Wavelets Based on Second Order Linear Time-Invariant Systems, Theory and Applications

Tariq Abuhamdia

Dissertation submitted to the Faculty of the
Virginia Polytechnic Institute and State University
in partial fulfillment of the requirements for the degree of

Doctor of Philosophy
in
Mechanical Engineering

Saied Taheri, Chair
John Burns
Corina Sandu
Dan Stilwell
Alfred Wicks
Craig Woolsey

March 17, 2017
Blacksburg, Virginia

Keywords: Wavelets Analysis, Second Order Linear Time Invariant Wavelets, SOULTI, Time-Frequency, Laplace Wavelets, System Identification, Modal parameters Identification

Wavelets Based on Second Order Linear Time-Invariant Systems, Theory and Applications

Tariq Abuhamdia

(ABSTRACT)

This study introduces new families of wavelets. The first is directly derived from the response of Second Order Underdamped Linear-Time-Invariant (SOULTI) systems, while the second is a generalization of the first to the complex domain and is similar to the Laplace transform kernel function. The first takes the acronym of SOULTI wavelet, while the second is named the Laplace wavelet. The most important criteria for a function or signal to be a wavelet is the ability to recover the original signal back from its continuous wavelet transform. It is shown that it is possible to recover back the original signal once the SOULTI or the Laplace wavelet transform is applied to decompose the signal. It is found that both wavelet transforms satisfy linear differential equations called the reconstructing differential equations, which are closely related to the differential equations that produce the wavelets. The new wavelets can have well defined Time-Frequency resolutions, and they have useful properties; a direct relation between the scale and the frequency, unique transform formulas that can be easily obtained for most elementary signals such as unit step, sinusoids, polynomials, and decaying harmonic signals, and linear relations between the wavelet transform of signals and the wavelet transform of their derivatives and integrals. The defined wavelets are applied to system analysis applications. The new wavelets showed accurate instantaneous frequency identification and modal decomposition of LTI Multi-Degree of Freedom (MDOF) systems and it showed better results than the Short-time Fourier Transform (STFT) and the other harmonic wavelets used in time-frequency analysis. The modal decomposition is applied for modal parameters identification, and the properties of the Laplace and the SOULTI wavelet transforms allows analytical and accurate identification methods.

Wavelets Based on Second Order Linear Time-Invariant Systems, Theory and Applications

Tariq Abuhamdia

(GENERAL AUDIENCE ABSTRACT)

This study introduces new families of wavelets (small wave-like functions) derived from the response of Second Order Underdamped (oscillating) Linear-Time-Invariant systems. The first is named the SOULTI wavelets, while the second is named Laplace Wavelets. These functions can be used in a wavelet transform which transfers signals from the time domain to the time-frequency domain. It is shown that it is possible to recover back the original signal once the transform is applied. The new wavelets can have well defined Time-Frequency resolutions. The time-frequency resolution is the multiplication of the time resolution and the frequency resolution. A resolution is the smallest time range or frequency range that carries a feature of the signal. The new wavelets have useful properties; a direct relation between the scale and the frequency, unique transform formulas that can be easily obtained for most elementary signals such as unit step, sinusoids, polynomials, and decaying oscillating signals, and linear relations between the wavelet transform of signals and the wavelet transform of their derivatives and integrals. The defined wavelets are applied to system analysis applications. The new wavelets showed accurate instantaneous frequency identification, and decomposing signals into the basic oscillation frequencies, called the modes of vibration. In addition, the new wavelets are applied to infer the parameters of dynamic systems, and they show better results than the Short-time Fourier Transform (STFT) and the other wavelets used in time-frequency analysis.

To Maysarah, my Father; Zahira, my Mother; Nedaa, my Wife, and my daughters Salma, Ayah, and Andalus, and to my friend Basel.

Acknowledgments

This work became a reality because of the bounties, guidance, blessings, family, great academic institution, fantastic and extraordinary supervisor, sincere committee, and supporting friends that Almighty God gave to me or led me to. I would like to thank Virginia Tech for giving me the opportunity, my supervisor, Professor Saied Taheri, for his patience and invaluable advice, my supervising committee, especially Professors John Burns and Craig Woolsey, all my family members who supported me in the past years, and my friends; Hassan Fayyed, Ibrahim Awad, Huthaifa Ashqar, Mohammed El-Jammal, Mostafa Ali, Haitham El-Marakby, Mohmmed Zain, Issa Amro and the others, who are all significant, for their help. In addition, I would like to thank Ms. Sydney Jones for her help in editing this manuscript. I may not forgot those who taught me and helped me in my academic life before starting the doctoral studies. I am grateful to Eng. Jalal Essalaymeh, and Professors Othman Zalloum, Danial Storti, Joseph Garbini, and Mark Damborg for what I learned from them, and Professors Karim Tahboub, Ishaq Seder, and Jacob Rosen for their encouragement and support.

Contents

List of Figures **ix**

List of Tables **xiii**

1 Introduction **1**

1.1 Literature Survey 2

1.1.1 Underdamped second-order LTI systems impulse response as a pseudo wavelet 14

1.2 Contribution 15

2 Wavelets **17**

2.1 General properties 17

2.2 Multiresolution analysis and orthogonal wavelets 21

2.3 Harmonic wavelets 22

2.4 Pseudo wavelets 24

2.5 Ridges and skeletons 25

3 SOULTI Wavelets **26**

3.1 SOULTI wavelet transform 26

3.1.1 Region of convergence 28

3.2 SOULTI wavelet inverse transform 29

3.2.1 SOULTI wavelet reconstruction identity 30

3.2.2 Particular solution of 2nd order autonomous ODEs 31

3.2.3 Particular solution of the reconstructing DE 33
3.3 SOULTI transform of elementary signals and its properties 34
3.3.1 SOULTI transform of derivatives 37
3.3.2 SOULTI transform of integrals 38
3.4 The time-frequency resolution and properties 39

4 Generalized Complex SOULTI Wavelets (Laplace Wavelets) 46
4.1 The Laplace Wavelet Transform 46
4.1.1 The Laplace transform and the Laplace wavelet transform 47
4.2 Inverse Laplace wavelet transform 49
4.2.1 Inverse Laplace wavelet transform 51
4.2.2 particular solution by Laplace wavelet transform 52
4.3 LWT of elementary signals and its basic properties 53
4.3.1 Laplace wavelet transform of derivatives 53
4.3.2 Laplace wavelet transform of integrals 54
4.3.3 Region of convergence 55
4.3.4 Time-frequency resolution 55

5 Harmonic Analysis 59
5.1 Numerical computation of the continuous SOULTI and Laplace wavelet transforms for discrete time-series 60
5.2 Resolving instantaneous frequency in frequency time-varying signals 61
5.2.1 SOULTI wavelet example 62
5.2.2 Laplace wavelet example 68
5.3 Analysis of a three degree-of-freedom mechanical system 69
5.3.1 Experiment and measurement system description 69
5.3.2 Time-frequency analysis by the Laplace wavelets 70
5.3.3 Modes decomposition 71

6 Modal Parameters Identification 89

6.1 Modal Decomposition 90
6.2 Modal Parameters Identification 96
6.2.1 Frequency estimation 96
6.2.2 Damping ratio estimation 97
6.3 Application Example 99
6.3.1 Simulated LTI 3-DOF system 99

7 Concluding Remarks **112**

Bibliography **114**

List of Figures

2.1 Decomposition of a signal into four-level MRA based on Mallat Algorithm [43]. © 2011 IEEE. 22

2.2 Four-Level DWPT decomposition tree [43]. © 2011 IEEE. 23

3.1 (a) Mass-spring-damper system (b) R-L-C electrical circuit 27

3.2 A SOULTI wavelet function with different properties defined. $\zeta = 0.3$, $a = 1$, and $p = 1$. 28

3.3 A SOULTI frequency domain function showing the mean frequency $\omega_{CG\zeta}$, the standard deviation-based frequency window $\Delta\Omega_{SD}$, and the (half-power)-based frequency window $\Delta\Omega_{BW}$. $\zeta = 0.5$, $a = 1$, and $p = 1$ 30

3.4 SOULTI Wavelet transform surface of the decaying exponential function at $\zeta = 0.7$ and $\beta = 2$. 35

3.5 SOULTI wavelet transform of $f(t) = \cos(\omega t)$, at $\zeta = 0.7$. 37

3.6 Wavelet amplitude in frequency domain for different values of scaling at $\zeta = 0.2$ 42

3.7 $|\Psi(a\omega)|$ for different values of ζ showing the quality factor and the half-power bandwidth. 44

4.1 The Laplace wavelet 47

4.2 The Laplace domain and the time-scale domain. 49

4.3 Laplace wavelet at different scales in the frequency domain. $\zeta = 0.01$. 56

4.4 Laplace wavelet in the frequency domain with quality factor, half-power points, and half-power bandwidth marked. $\zeta = 0.5$. 57

5.1 Top: single harmonic with white noise of SNR = 15dB. Bottom: single harmonic with white noise of $SNR = 7.5$dB. 62

5.2 Contour mapping of the SOULTI wavelet Transform of a harmonic signal of frequency=2rad/s. (a) $SNR = 15$dB (b) $SNR = 7.5$dB. 63

5.3 Sum of two harmonics with white noise. $\omega_1 = 2$rad/s, $\omega_2 = 8$rad/s, and the $SNR = 15$dB. 64

5.4 SOULTI wavelet transform for the two harmonics signal in Figure 5.3. (a) Time-scale contour mapping. (b) Time-frequency contour mapping. 65

5.5 Two constant harmonics with a time varying frequency component signal. . . 66

5.6 Frequency spectrum of the signal described by 5.10. (Dashed line) FFT. (Solid line) Welsh spectrum averaging 67

5.7 SOULTI wavelet transform for the chirp signal described by Equation (5.10) and shown in Figure 5.5. (a) Scalogram (Time-scale) contour mapping (b) Spectrogram (Time-frequency) contour mapping. 68

5.8 Scalograms of the signal described by Equation (5.10) using different wavelets. (a) by Morlet wavelet (b) by Complex Shannon wavelet ($f_b = 1$, $f_c = 1$) (c) by Mexican hat wavelet (d) by Frequency B-Spline wavelet (order=2, $f_b = 1$, $f_c = 1$). f_b: bandwidth frequency. f_c: wavelet center frequency 74

5.9 Spectrograms of the linear chirp signal in Equation (5.10) at different Window widths (samples). (a) $W = 8$ (b) $W = 16$ (c) $W = 32$ (d) $W = 64$ (e) $W = 128$ (f) $W = 256$. 75

5.10 Reverse wavelet transform of the signal in Figure 5.3. (a)Scalogram, time-scale contour. (b) Spectrogram, time-frequency contour mapping. 76

5.11 Reverse wavelet transform of the signal in Figure 5.5. (a) Scalogram, time-scale contour mapping. (b) Spectrogram, Time-frequency contour mapping. . 76

5.12 Average of FWT and RWT of the linear chirp in Figure 5.5. (a) Scalogram, time-scale contour mapping. (b) Spectrogram, time-frequency contour mapping. 77

5.13 Quadratic chirp and two constant harmonics and white noise at SNR=15dB. 77

5.14 Laplace Wavelet Transform of $S(t)$ in Equation (5.11). (a) Time-scale contour (scalogram) (b) Time-frequency contour (spectrogram). 78

5.15 (a) schematic of 3 DOF Mass-spring system with friction (b) The testing bench used in experiments. 78

5.16 The response acceleration (left column), velocity (center column), and displacement (right column) for mass M_1 (top row), M_2 (middle row), and M_3 (bottom row). 79

5.17 Spectrogram contour of the LWT, with $\zeta = 0.01$, of acceleration (left column), velocity (center column), and displacement (right column), and of M_1 (top row), M_2 (middle row), and M_3 (bottom row). The contour is plotted at 15 contour lines. 80

5.18 Spectrum on semi-log scale of the acceleration (left column), velocity (middle column), and displacement (right column) for M_1 (top row), M_2 (middle row), and M_3 (bottom row). 81

5.19 Spectrogram contour of the Morse wavelet transform of acceleration (left column), velocity (center column), and displacement (right column), for M_1 (top row), M_2 (middle row), and M_3 (bottom row). The contour is plotted with 15 contour lines. 82

5.20 Spectrogram contour of the Morlet wavelet transform of acceleration (left column), velocity (center column), and displacement (right column), for M_1 (top row), M_2 (middle row), and M_3 (bottom row). The contour is plotted at 15 contour lines. 83

5.21 Spectrograms contours of the STFT of acceleration (left column), velocity (center column), and displacement (right column), for M_1 (top row), M_2 (middle row), and M_3 (bottom row). The contour is plotted at 15 contour lines. . 84

5.22 LWT Mode decomposition of $x_1(t)$. Skeleton lines at the modal ridges from mass M_1 displacement spectrograms shown in Figures 5.17 and 5.19 to 5.21. 85

5.23 Skeleton lines at the modal ridges from the velocity spectrograms of mass M_1 shown in Figures 5.17 and 5.19 to 5.21. (a) 1.6 Hz skeleton; (b) 11.6 Hz skeleton; (c) 31 Hz skeleton. 86

5.24 Skeleton lines at the modal ridges of mass M_2 velocity spectrograms shown in Figures 5.17 and 5.19 to 5.21. (a) 1.6 Hz skeleton; (b) 11.6 Hz skeleton; (c) 31 Hz skeleton, notice the enlarged section. 87

5.25 Skeleton lines at the modal ridges of mass M_3 velocity spectrograms shown in Figures 5.17 and 5.19 to 5.21. (a) 1.6 Hz skeleton; (b) 11.6 Hz skeleton; (c) 31 Hz skeleton. 88

6.1 Block diagram representing the Laplace and SOULTI wavelets transform as the output of linear time-invariant system. 92

6.2 $|\Phi_{L\zeta}(as_1)|$ and $|\Phi_{L\zeta}(as_2)|$ versus scale for $\omega_{dk} = 1$, $\zeta = 0.2$, and $\xi = 0.4$. . . 95

6.3 Laplace Wavelet Spectrogram for the response of the simulated 3 DOF system. (a) $\dot{x}_1(t)$ spectrogram. (b) $\dot{x}_2(t)$ spectrogram. (c) $\dot{x}_3(t)$ spectrogram. 100

6.4 Spectrums of the simulated example response. Top $\dot{x}_1(t)$, Center $\dot{x}_2(t)$, and Bottom $\dot{x}_3(t)$. 102

6.5 LWT of $\dot{x}_1(t)$ at the modal frequencies. Top, first mode; center, second mode; bottom, third mode. 103

6.6 LWT of $\dot{x}_2(t)$ at the modal frequencies. Top, first mode; center, second mode; bottom, third mode. 104

6.7 LWT of $\dot{x}_3(t)$ at the modal frequencies. Top, first mode; center, second mode; bottom, third mode. 105

6.8 Spectrums of the LWT of $\dot{x}_1(t)$ at the modal frequencies. Top, first mode; center, second mode; bottom, third mode. 106

6.9 Spectrums of the LWT of $\dot{x}_2(t)$ at the modal frequencies. Top, first mode; center, second mode; bottom, third mode. 107

6.10 Spectrums of the LWT of $\dot{x}_3(t)$ at the modal frequencies. Top, first mode; center, second mode; bottom, third mode. 108

6.11 Hilbert envelops of the modes. Top row, first mode; center row, second mode; bottom row, third mode. Left column, $\dot{x}_1(t)$, center column, $\dot{x}_2(t)$, right column $\dot{x}_3(t)$ 109

6.12 Natural logarithm of the decaying envelops in Figure 6.11. Top row, first mode; center row, second mode; bottom row, third mode. Left column, $\dot{x}_1(t)$, center column, $\dot{x}_2(t)$, right column $\dot{x}_3(t)$ 109

6.13 Hilbert envelops of the modes. Top row, first mode; center row, second mode; bottom row, third mode. Left column, $x_1(t)$, center column, $x_2(t)$, right column $x_3(t)$ 110

6.14 Natural logarithm of the decaying envelops in Figure 6.11. Top row, first mode; center row, second mode; bottom row, third mode. Left column, $x_1(t)$, center column, $x_2(t)$, right column $x_3(t)$ 111

List of Tables

3.1 SOULTI wavelet transform for basic signals. 36

3.2 Time-Frequency resolution based on standard deviation definition at $p = 1$. . 40

4.1 Laplace wavelet transform for basic signals. 54

6.1 Physical parameters for 3-DOF Linear mass-spring-damper system 100

6.2 Dynamic parameters for the 3-DOF Linear mass-spring-damper system . . . 100

6.3 Estimated frequencies by LWT and FFT. 101

6.4 Estimated slopes of the envelopes natural logarithm and estimated damping ratios from the velocity response. 101

6.5 Estimated slopes of envelopes exponentials and estimated damping ratios from the displacement response. 102

Chapter 1

Introduction

The content of this chapter is extracted from a study by the author of this dissertation that is published in the Journal of Vibration and Control [1].

Wavelets provide a powerful tool to analyze signals and extract information from them. They are capable of extracting frequency, time, and non-harmonic information. These potentials lured many scholars to use them in the analysis of dynamic systems. Scholars have used wavelets for system identification, system modeling, system response solution, and even control design.

Mathematically, The wavelet transform is an inner product between a function and a set of basis functions who are all derived from a single function called the mother wavelet. So it measures how much parallelism exists between the analyzed function and the set of basis functions. Therefore, if we seek extracting some features from a signal, then the analyzing wavelet family should have that feature. This is similar to the way we measure the periodicity of a signal by making inner product with the harmonic functions for their periodicity.

This idea implies also, that if we want to make time-frequency analysis of a dynamic system by analyzing its response, a better understanding can be developed if the analyzing wavelet is close in characteristics to systems responses and behaviors.

This observation led to investigating the characteristics of the underdamped second-order response of LTI systems to find if it can serve as a mother wavelet. The underdamped second-order impulse response of LTI systems is oscillatory and decaying exponentially, and it dies out to effective zero within well defined period. Furthermore, its frequency domain representation is a second-order filter that can effectively extract certain frequency bands from signals.

This dissertation lays out the theory that establishes the response of Second-Order Underdamped Linear Time-Invariant systems as a wavelet, which will be called for brevity the SOULTI wavelet. The remainder of this chapter presents a comprehensive literature survey

on the applications of wavelets to dynamic systems analysis and control. A special attention is given to previous employment of the underdamped second-order LTI systems response as pseudo wavelets in Section 1.1.1. Chapter 2 gives a background on wavelets theory in general. Chapter 3 defines the SOULTI wavelet, its transform and its inverse transform. Chapter 4 generalizes the SOULTI wavelet from a real-time wavelet to the complex domain to produce the Laplace wavelet. Chapter 5 discusses using the SOULTI and Laplace wavelets for harmonic analysis. Computing the transforms for time series in accordance with the Shannon theory is explained, then it is applied to instantaneous frequency detection and modal system identification. This paves the road for modal parameter identification of linear systems that is treated in detail in Chapter 6.

1.1 Literature Survey

Many scholars are searching for analysis tools that are more suitable for Time-Varying (TV) and nonlinear systems. Tools that better adapt to the modal parameters change with time and the non-harmonic behavior or response of these systems. Wavelets are a good candidate tool given their numerous wave shapes and the time-scale or time-frequency localization property. However, wavelets also have been used for the analysis of Linear Time-Varying (LTI) systems, where some scholars have been trying to find a unified approach between the time-domain and the frequency-domain. The following literature survey is adapted from an extensive study. For more detail, the reader is referred to [1].

The idea of using wavelets in physical systems engineering appeared with the first applications of wavelets. The capability of decomposing a signal into scale-time components, and the direct relation between scale and frequency in many wavelet families made wavelets intuitively attractive to analyze nonlinear and TV systems.

Wavelets are among the different time-frequency analysis tools that can be applied to system analysis. Wigner-Ville Distribution (WVD) is one of the oldest methods that shows the distribution of the signal power over time and frequency [23]. The Short Time Fourier Transform (STFT) gives direct decomposition of the signal into components along frequencies at successive time intervals. It uses translated window functions to extract intervals of the signal and perform harmonic analysis. However, the analysis depends on the window width and the translation method [46]. Gabor Transform is a special case of the STFT that uses the Gaussian distribution as the window function [29].

The wavelets analysis differs from the time-frequency analysis by decomposing the signal over a time-scale domain [94]. However, the scale can be linked to frequency as will be shown later. Two types of wavelet transforms exist: continuous wavelet transform and discrete wavelet transform. The Discrete Wavelet Transform (DWT) distributes the components along scales that increase geometrically by a multiple power of two [27]. Researchers have applied both continuous and discrete wavelet transforms to all types of systems.

wavelets found room for successful application in vibrations analysis by solving and characterizing the response and obtaining the spectrum and in system identification.

Many researchers used wavelets as bases functions for discrete numerical solutions of vibrational boundary value problems (BVPs) because of their local nature and scaling and translation parameters. The Galerkin-Wavelet approach for solving generic BVPs is well established. Xu and Shann [138] presented a thorough treatment of the two-point BVP. Díaz [30] presented a Galerkin-Wavelet method for solving continuous parameter vibrational and heat transfer boundary value problems.Youhe et al. [145] used the same approach for solving the Euler-Bernoulli beam equation, and They approximated the deflection by the Daubechies scaling basis. In their study, they also applied the same procedure for the deflection equation of plates.

Mei et al. [89] presented a wavelet stochastic FEM for beam structures. They addressed the problem of variations in geometry and material along the beam length, so they modeled the bending stiffness by a constant added to a stochastic process. Tratskas and Spanos [130] applied the harmonic wavelet transform to obtain the evolutionary spectrum and the response of LTI MDOF systems to stochastic input. They used the linear properties of both the convolution integral and the wavelet transform and derived the wavelet transform of the particular solution of the system in discrete form. Tratskas and Spanos applied their method to solve the response of the 2-DOF system and generated an evolutionary spectrum of it. They compared this spectrum with a one generated by the Monte Carlo simulation method and showed that the two are almost identical. In a similar way, Basu and Gupta [9, 10] applied the L-P wavelets to obtain the response statistics of systems subject to nonstationary seismic inputs for Multi [9] and single [10] DOF systems. They applied the same scheme for structural systems with Coulomb damping at the foundation [11].

Nonlinear TV systems do not have stationary frequencies of oscillation; their frequencies as well as their amplitude change with time. Standard Fourier analysis does not capture this behavior. As explained in Section 2.1, wavelets overcome the time-frequency resolution drawbacks of STFT and provide better window width adaptability to different frequency subbands. Consequently, one of the intuitive usages of wavelets is obtaining a TV spectrum, also referred to "evolutionary spectrum."

The geophysics discipline initiated the concept of modern wavelets. Geophysicists analyzed seismic data to obtain the time-frequency spectrum. Chakraborty and Okaya [15] used the matching pursuits algorithm by Mallat and Zhang [88] to achieve good time-frequency resolution at mid to high frequencies. Later, other researchers obtained time-frequency spectrum for mechanical systems [10, 129].

Pham and Wong [105] used the DWPT for power system harmonic analysis. Their algorithm showed improvements in identifying all the harmonics contained in the analyzed signals including integer, non-integer and sub-harmonics. The algorithm consists of two stages. First the signal is decomposed into equal sub-bands by the DWPT; then the CWT, using the Morlet wavelet, is applied to each sub-band to identify its frequency content. Lamarque

and Malasoma [68] used wavelets for the analysis of nonlinear oscillatory systems to identify chaotic behaviors . They defined a quasi-Lyapunov Exponent or greatest Lyapunov-like exponent

Neild et al. [96] performed a comparative study between Short-Time Discrete Fourier Transform (STDFT), moving window Auto-Regressive algorithm (AR), Windowed-Wigner-Ville distribution(WWV), and harmonic wavelets for structural vibration analysis. The study compared each method's capability in estimating the fundamental frequency over time. It also showed that the harmonic wavelets yielded similar outcomes to WWV's results, and were best in estimations at the beginnings and ends of signals.

One of the goals of vibrations analysis in Ambient Vibration Test (AVT) is distinguishing harmonics from structural components. Le and Argoul [74] pursued this goal and proposed four steps for distinguishing structural modes from harmonic components: compute the skeletons and the associated ridges (see next section for explanation of ridges), obtain the analytic signals and take the real part of them, normalize the results by subtracting from them the expected value and divide the results by their standard deviation, and draw the histogram of the results in the previous step and calculate their Kurtosis. If the Kurtosis value is close to 3 and the histogram is similar to a bell shape, then the component is for structural mode. However, if the kurtosis value is close to 1.5 and the histogram has two symmetrical peaks at the boundary, then the component is a harmonic component.

Many recent studies demonstrate the advantages of using wavelets in systems and modal parameters identification. Therefore, we offer a review of the recent advances in this realm. Wavelets are an attractive tool for systems identification because they are capable of extracting transient features and localizing both frequency and time. Significant number of the recent studies on using wavelets for dynamic systems and control used wavelets for systems identification with notable high quality results. Hence, wavelets-based systems identification can be considered a well established application of wavelets.

The terms System Identification and Modal Parameters Identification signify very close ideas, but there is slight difference between the two with respect to the applied applications. Modal parameters identification is mostly applied to structures including civil structures. It refers to measuring signals produced by structures or mechanical systems and identifying their parameters: damping, frequency, mode shapes, and modal participation factor [58]. This is why wavelets have been a very active research topic in civil engineering in recent years.

The term "system identification" has been used mainly for the process of measuring signals produced by a system and building a model to represent that system for control design [58]. This section covers both modal parameters identification and system identification. It is worth mentioning here that system identification for control purposes and some vibrations applications can be parametric [84] or non-parametric [85]. In non-parametric system identification, the transfer function or the FRF is identified.

The application of the wavelet transform for system identification requires an analyzing-

wavelet with good frequency localization. Therefore, the Morlet wavelet, harmonic wavelets, L-P wavelets, and Cauchy wavelets all have many applications in systems and modal parameters identification. It is relevant to mention that before any use of wavelets in systems identification, Jezequel and Argoul [56] proposed an integral transform for non-parametric LTI systems identification that allows the detection of the poles and zeros of the transfer function. The transform is similar to the wavelet transform and is performed in the frequency domain. Argoul [4] called the kernel function in the transform as the *Cauchy Wavelet*, or the *Complex Fractional Wavelet*, and re-interpreted the integral transform as a continuous wavelet transform.

Yin et al. [143] used the complex fractional function, or the Cauchy wavelet, in the standard definition of the wavelet transform with frequency as the independent variable.

The first attempt to use wavelets for system identification goes back to Tsatsanis and Giannakis [131]. They applied discrete wavelet transform to TV-AR and Auto-Regression Moving Average with Exogenous Input (ARMAX) models. Huang et al. [52], used the time series ARX model with multiple variables in a wavelet-based procedure for modal parameters identification of LTI models. They used the orthogonal wavelets symlets 1, 4, and 10. Huang and Su [51] followed a similar path to that in [52] but used the harmonic wavelets. Su et al. [126] presented a method that combines the TV-ARX method of Huang et al. [53] for SDOF systems with the CWT to estimate the instantaneous modal parameters of a structure. Chang and Shi [16] applied multiresolution analysis to identify the TV-hysteresis parameters of structures. Instead of using ARX models, which requires data pre-filtering with some knowledge of the system FRF or at least the FR, Váňa and Preisig [132] used wavelets with a weighting matrix that makes the filtration process simpler by tweaking the matrix's diagonal entries only.

Schoenwald [113] adapted the Pearson-Lee modulation method [104] for system identification and proposed replacing the modulating function with a wavelet basis.

Coca and Billings [24] used the Spline wavelets to identify linear and nonlinear systems. Their technique depends on describing the system input and output in terms of the spline wavelet, then the problem changes to solving an algebraic equation. Paiva and Galvao applied digital wavelets (subband filters) to digital models (in Z-domain) of dynamic systems [93]. Klepka and Uhl [64] put a technique derived from recursive least square, inside which, they used adaptive wavelet filter to separate modes. Then, they estimated the parameters of each mode separately. Sone et al. [119] proposed a similar system identification method for MDOF systems that applies the Mexican hat wavelet transform to the equation of motion. The method requires the acceleration data only because they developed a relation that links the wavelet transform of the integral of a signal to the wavelet transform of the signal.

Finding the response's decaying envelop gives valuable information about the system's characteristics and parameters. Dishan [32] developed an algorithm for finding the Hilbert transform based on wavelets. Later, Sheen and Hung [115] improved the method for constructing a wavelet-based envelop function from vibration signals. Staszewski and Cooper [123] used

the Morlet wavelet to identify the damping in an aircraft during flight testing. Though flutter is a time-varying and nonlinear phenomenon, they treated the system as a LTI MDOF. The natural frequencies and the modes were recognized directly on the Wavelet transform time-scale map. The method is based on the observation that the modulus of the wavelet transform gives the estimate of the envelope function. Then, the logarithm of the modulus gives a line equation, in which the line slope represents the damping ratio of the mode. Ruzzene et al. [112] and Staszewski [121] improved this method and developed complete analysis procedures for system identification. They used the Morlet wavelet for identifying the natural frequencies and the damping ratios of MDOF Mass-Spring-Damper systems.

Hilbert Transform is good for producing the envelop function from an oscillatory response if the response corresponds to a single mode or to SDOF system. For MDOF systems, the Hilbert transform method is not efficient. However, wavelets can extend Hilbert transform method to MDOF systems. With direct relation between frequency and scale in the Morlet wavelet, the wavelet transform extracts each mode response by itself from the total response, thus it decouples the response of the system.

An alternative approach described by Staszewski [121] is using the approximation reconstruction formula on the extracted mode wavelet transformation. This retrieves back the single mode impulse response. In their study, Ruzzene et al. [112] showed superiority of this method to the Hilbert Transform Method especially for MODF systems.

The ridge and skeleton method is an important method for extracting frequencies and modes form signals. Ridges and skeletons are basic features of any wavelet transform, and they are described in Section 2.5. The ridge and the skeleton of each wavelet can be found separately for each mode, then the envelop function of the impulse response for each mode can be obtained from the analytic function. Then, the damping ratio is calculated. It is obvious that this method depends on finding the ridge of the transform.

There are different algorithms to extract the ridge. The simplest one detects the maximum of the amplitude of the transform along the scale axis. This algorithm gives exact results for linear ridges. The other algorithm uses the phase function of the transform [128]. The first algorithm depends on the conditions given by

$$\frac{\partial \theta(a,b)}{\partial a} = 0, \tag{1.1}$$

$$\frac{d\theta(a,b)}{db}_{t_s(a,b)=b_0} = \frac{\theta'_\psi(0)}{a}. \tag{1.2}$$

Staszewski [122] extended the ridge-skeleton method to identify nonlinear systems' models. The procedure consists sequentially of computing the wavelet transform of the output signal, performing mode decoupling, identifying the ridge $a = r(b)$, finding the instantaneous frequency at each translation b from Equation (2.32), computing the instantaneous envelope from the approximation formula, obtaining the backbone function from the instantaneous

envelop and frequency, and fitting the envelop with the other backbone curves of nonlinear systems.

Not only the Morlet wavelet is used with the Ridge-Skeleton Method, Newland [99] showed Rige-Skeleton extraction scheme with harmonic wavelets. Argoul and Erlicher [5] used the Cauchy wavelet with the Ridge-Skeleton method and applied it in the frequency domain. In another study, Erlicher and Argoul [35] applied the Cauchy wavelet Ridge-Skeleton method to identify non-proportional damping in linear systems. Le and Argoul [73] applied the method and did a comparison between Morlet, Cauchy, and the harmonic wavelets and addressed the end effect problem. According to them, Morlet and Cauchy wavelets gave close results, but the Harmonic wavelets' results were unsatisfactory. Also, Rouby et al. [111] made a comparison ,based on the Ridge-Skeleton method, between the Chebyshev polynomials and the Cauchy wavelets in parameter identification of linear mechanical systems in the time domain. Slavic et al. [118] applied this approach to the lateral vibration of a uniform beam with free-free boundary conditions . They investigated the edge effect on system identification and defined an instantaneous Signal to Noise Ratio (SNR) and Mean Square Error (nMSE) for measuring the quality of identification. Lardies and Gouttebroze [71] applied the Ridge-Skeleton method to identify the parameters of a broadcasting tower, and Lardies [70] applied it to identify the parameters of an acoustic enclosure. In both studies, they used the optimized Morlet wavelet based on the signal entropy, and referred to it by the Modified Morlet Wavelet. Lardies and Ta [72] followed a similar approach to identify the damping in a nonlinear oscillator. First, they solved the nonlinear system by Krylov-Bogolinbov method of averaging. Then, they applied the wavelet cross-section method and the Ridge-Skeleton method to find the parameters that characterize the nonlinear damping.

Kijewski and Kareem [62] studied this method also and investigated some processing concerns such as the time-frequency resolution, the frequency bandwidth, the end effect melioration, and the selection of the wavelet central frequency. They proposed padding for the end effect, and determined the frequency bandwidth based on Gabor's mean square, where only 68% of the frequency window is accounted for. Yan et al. [142] followed a similar approach to the Ridge-Skeleton method. However, they also applied the boot strap statistical technique for uncertainty reduction. Yan and Miyamoto [141] also did a comparative study between the wavelet transform Ridge-Skeleton method and the Hilbert-Huang Transform (HHT) method. The HHT method consists of performing the Empirical Mode Decomposition (EMD) followed by the Hilbert Transform [54]. They tested the two methods by impact test and ambient vibration test of a bridge, and the wavelet transform Ridge-Skeleton method was better and more effective than the HHT method for the identification of systems with very closely spaced modes [141].

Wavelets are also used to model dynamic systems. The mathematical model can be a state space model, a system of second order ODEs, an impulse response convolution, or a Frequency or a Laplace domain transfer function. The wavelet transform is applied to these models in a similar way to the Fourier or Laplace transform application to LTI systems. However, there are essential differences between the two: there is time-translation parameter

in wavelets, there are many wavelet mother functions, and the wavelet transform integral is complex and difficult to evaluate. Nevertheless, wavelets show superior results to standard frequency domain transforms especially in the case of TV and nonlinear systems.

Robertson et al. [109] put a simple method for extracting the impulse response characteristics of LTI systems. They applied the Discrete wavelet transform with orthogonal wavelets to input-output convolution relation in the time interval $0 \leq t \leq t_n$. Since the wavelets used are orthogonal, the inverse wavelet transform requires less number of computations. Similarly, Kitada [63] offered a method to identify the piecewise linear damping and the tangential stiffness using the Daubechies D4 orthogonal wavelet. Lamarque et al. [69] described a wavelet logarithmic decrement formula, and Hans et al. [45] applied it for damping identification of a four-story civil structure.

Ghanem and Romeo [40] followed an approach similar to the Galerkin-FEM approach, where the wavelet transform is applied to the mathematical model of a Linear Time-Varying (LTV) system. The importance of their work lies in defining a relation between the wavelet transform of a function and the wavelet transform of its derivative. Ghanem and Romeo [41] applied the same method to nonlinear system identification. The nonlinear model contained constant and linear Coulomb friction terms, cross-coupling polynomial, and cubic stiffness. Pacheco and Steffen Jr [101] developed a parallel method that uses orthogonal functions for identifying the nonlinear systems which has Coulomb friction and cubic stiffness. Xu et al. [139] proposed an approach for TV systems identification, where the wavelet transform of the integral of a variable is developed. The approach assumes a known inertia matrix and slowly varying stiffness and damping and uses the free decay response. In another study, Xu et al. [140] presented a method that can use either free or forced vibration responses to identify the parameters of a LTV system described by time-varying state space model.

Chakraborty et al. [14] used the modified L-P wavelets, given in Equation (2.28), for modal parameters and mode shapes identification of the LTI-MDOF systems. Basu et al. [12] proposed a method to perform online identification of the stiffness in LTV systems. They used the proportion between the energy and the integral of the square of the wavelet transform.

Sometimes the system can not be excited by a single input, or its free vibration response is not available because the system has many disturbances and continuous sources of uncontrolled inputs. For example, consider a bridge under traffic loading, wind excitation, and seismic base inputs. Some studies have found in wavelets a way to identify systems with unknown ambient vibrations. Le and Paultre [75] applied the Cauchy wavelet transform for the matrix of response correlation function to identify the natural frequencies and the mode shapes during ambient vibration testing.

Gandelli et al. [39] presented an application of the Haar wavelet transform for the parameter identification of electrical circuits. They applied the method to RL load circuit with square wave input. The method consists of transforming the discrete time-domain state space model of the circuit to the Haar-domain.

Some of the mentioned methods extend their application to chemical and nuclear systems. Tangirala et al. [127] surveyed some wavelets applications for the modeling of process control and chemical systems.

Pseudo wavelets are introduced in section 2.4, and system identification is one of their applications. Wilson [135] used a sequence of zeros and ones to generate a pseudo mother wavelet. She generated the sequence by applying the condition of Persistent Excitation (PE) on the binary sequence. The resulting pseudo wavelet has good filtration property that resembles low-pass filter with a sharper cut-off frequency.

Staszewski and Giacomin [124] suggested a wavelet-based FRF, counter to the harmonic-based FRF, and applied it to the data of nonstationary vibrations of a vehicle. In another attempt to define a similar FRF, Dziedziech et al. [33] used both wavelets and Wigner-Ville distribution as time-frequency transformations. Dziedziech et al. [33] proposed adding Gaussian noise to both the input and the output signals so that an ensemble of noisy signals was obtained, $\{u_i(t)\}, \{y_i(t)\}$. Then, they calculated the TF for the noisy signals, and took the averages of the input ensemble and the output ensemble for the TF-FRF definition as shown in Equation (1.3).

$$H(t,\omega) = \frac{E\left[TF\left[y(t)\right]\right]}{E\left[TF\left[u(t)\right]\right]}, \tag{1.3}$$

where E denotes the expectation operator. Though the preceding definitions seem to offer reasonable wavelet-based FRFs, Staszewski and Wallace [120] pointed out that it is inconclusive as the entire concept has not been supported by any reasonable interpretation and the output to input wavelet based ratio is sensitive to noise and singularities. Instead, they offered a different definition and interpretation of a wavelet-based FRF using the generalized convolution operator. Tratskas and Spanos [130] also defined a wavelet transfer function for MDOF mechanical systems. Their definition depends on the harmonic wavelets defined by Equations (2.23) and (2.24).

In a parallel way to the methods of cross-correlation in time domain and cross-coherence in the frequency domain for model validation, Kyprianou and Staszewski [67] attempted to define a cross-wavelet transform between the input U and the output Y of a system as the inner product of the output Y and a transformed version of the input U.

$$\overline{W_{a,b}\{Y\}}\, W_{a,b}\{U\} = \overline{\langle \psi_{a,b}, Y\rangle}\ \langle \psi_{a,b}, U\rangle = \left\langle Y, \psi_{a,b}\ \psi^*_{a,b} U\right\rangle. \tag{1.4}$$

Here, $\psi_{a,b}\ \psi^*_{a,b}$ is the transformation operator. Tratskas and Spanos [130] used Equation (1.4) to define the Cross-Spectrum (CS) between LTI MDOF system's output and its corresponding stochastic input. They defined the cross-spectrum as the expected value of the magnitude of the cross wavelet transform defined in Equation (1.4).

Jiang and Mahadevan [57] proposed different wavelet-based CS and coherence definitions. If the experimental observation of a dynamic system is $x_E(t_n)$ and the prediction output is $x_P(t_n)$, they defined the wavelet-based CS by

$$S_{x_E x_P}(a,b) = W\{x_E\} W\{x_P\} \tag{1.5}$$

and the wavelet-based coherence by

$$C_{EP}^2(a,b) = \frac{|\bar{S}_{x_E x_P}(a,b)|}{\left(\bar{S}_{x_E}(a,b)\right)^2}, \tag{1.6}$$

where $\bar{S}_{x_E x_P}(a,b)$ is the smoothed time-frequency cross spectrum, and $\bar{S}_{x_E}(a,b)$ is the smoothed wavelet power spectrum defined by

$$S_{x_E}(a,b) = |W\{x_E\}|^2. \tag{1.7}$$

Wilson [136] proposed a wavelet correlation for transfer function estimation of the fifth order low pass filter as shown in Equation (1.8).

$$\hat{H}_W(\omega) = \frac{\int\int\int \frac{1}{\sqrt{a}} y(t) u(\frac{t-b}{a}) e^{-j\omega b} dt\ db\ da}{\int\int\int \frac{1}{\sqrt{a}} u(t) u(\frac{t-b}{a}) e^{-j\omega b} dt\ db\ da}, \tag{1.8}$$

where $y(t)$ is the system's output, and $u(t)$ is the system's input, which is the mother wavelet. The wavelet used in Wilson's study is the pseudo-random binary sequence, which is classified as a pseudo wavelet in Section 2.4.

Kougioumtzoglou and Spanos [65] introduced Harmonic wavelet based input-output relationship or wavelet response function. Based on the assumption of small frequency band. Wavelets are used for vibration analysis to characterize and detect systems' properties. This information helps qualifying and predicting the systems' response and comparing different systems' behavior. Argoul and Le [6] applied the Cauchy wavelet defined in Equation (1.9) with the Ridge-Skeleton method to obtain four instantaneous indicators characterizing systems' nonlinearities. The indicators are: pseudo-frequency, positive modal shape, energy dissipation of a mode, and the deviation from linear viscous damping.

$$\psi_n(t) = \left(\frac{i}{t+i}\right)^{n+1}. \tag{1.9}$$

Meliopoulos and Lee [91] used Daubecheis Wavelets to find the transient response and the disturbances of LTV systems. They solved the transient response of an electrical network. Hsiao and Wang [50] and Liu and Zhang [82] proposed an interesting employment of the Haar wavelet for the analysis and solution of LTV systems described by the state space model. They approximated the input vector, the state vector, and the initial state vector by $(m-1)$th resolution levels, so they expanded them by the mth Haar wavelet bases vector. Chen and Hsiao [19] exploited Haar integral operational matrix given by Equation (1.10) to solve the response of lumped and distributed parameters systems. They demonstrated the validity of the method for distributed parameters systems on a continuous transmission line model. The method is identical to the method proposed by Chen and Hsiao [19].

$$\int_{t_0}^{t} \psi(\tau) d\tau = \mathbf{P}\psi_m(t). \tag{1.10}$$

Mahadevan and Hoo [86] applied the Galerkin approach with wavelets as basis functions to obtain reduced model for control design. They used Daubecheis and B-spline scaling and wavelet functions in addition to their anti-derivatives.

As an application of wavelets to electrical systems analysis, Gandelli and Leva [38] used the Haar wavelet to construct LTI state space model for power electronics systems. They applied the method to three-phase inverter Park equivalent circuit model. Barmada et al. [7] applied wavelet expansion to the scattering matrix, which is usually used for modeling transmission lines and communication circuits and to analyze integrated circuits. Their results showed $40-50\%$ reduction in computational cost and competitive results to the standard FFT-IFFT techniques.

Most of the methodologies discussed in this survey are related in one way or another to control systems. However, we discuss in the following the efforts that have direct involvement of wavelets into control design or synthesis.

As computational costs are becoming cheaper and more affordable, implementation of wavelets in real-time is becoming a realistic approach. Yet, some researchers attempted to implement the wavelets filters by analogue circuits. For example, Li and He [77] implemented CWT through Multiple-Loop Feedback (MLF) Switched Current (SI) filters. These efforts make the use of wavelets into applications that require quick control reactions possible.

Chou [22] presented one of the earliest attempts to exploit the advantages of wavelets in control systems. He proposed a solution for the problem of communication bottleneck of systems with large number of sensors and actuators, i.e. inputs and outputs, such as in the control case of distributed parameter systems. Chou proposed using the wavelet transform in a similar fashion to the similarity transform to transform the states, the outputs, and the inputs from the time domain to the wavelet domain to reduce the computational and the communication burden.

Many of the mentioned wavelet-based parameters identification methods can be also applied to control systems. Li et al. [76] used the Mexican hat wavelet with an iteration algorithm that compares the Digital Wavelet Transform (DDWT) coefficients of the output with the model DDWT coefficients in iterative mode until the minimum error coefficients are obtained. Loussifi et al. [84] applied the wavelet Ridge-Skeleton method using the optimized Morlet wavelet for parameters identification of elastic drive system. The optimal Morlet wavelet is chosen to minimize the signal entropy according to Lin and Qu [81] approach. The identification procedure is similar to the procedure of Lardies and Gouttebroze [71].

Cole et al. [26] introduced a wavelet analyzer in the control loop of adaptive control of rotor vibration. Their approach consists of synthesizing a control action $u(t)$ using a wavelet expansion. During each cycle, the controller analyzes the vibrations output signal and extracts its wavelet coefficients, and according to its largest coefficients from the previous cycle, the controller tweaks the wavelet coefficients that synthesize the control action. The controller will then cancel the effects of periodic but possibly irregular disturbance inputs.

Though wavelets showed improvements on different control methods and applications, some applications require further development of wavelets implementation to render practical use in systems as the following study shows. For example, Aitken and Clarke [3] investigated the value the time-frequency analysis that wavelets could provide for an Oberver Kalman Filter Identification/Eigner Realization Algorithm(OKID/ERA). They converted the discrete time signals and variables to the wavelet domain and substituted the results into the OKID/ERA algorithm. However, when they compared the results with the standard Kalman filter, the wavelets-based results were not competitive.

Parvez and Gao [102, 103] proposed a wavelet controller similar to the classical PID controller, where the error signal $e(t)$ is decomposed through an MRA into high, intermediate and low scale-components.

After the signal is decomposed, each component is scaled by a scaling coefficient. This constitute the control law. Then, the signal is reconstructed back to form the controller output and is input to the controlled process. Though the control law is novel and shows potential for rejecting noise as claimed in [102, 103] but selecting the values of the gains K is not presented based on rigorous mathematical analysis; i.e the effect of these gains on stability is not clear.

Islas-Gomez et al. [55] compared the performance of eight mother wavelets in auto- tuning a PID controller for a DC motor. The wavelets tested are Morlet, RASP1, RASP2, RASP3, POLYWOG1, POLYWOG3, POLYWOG4, and Shanon. Tuning the PID gains is achieved through a wavenet that performs system identification then updates the gains based on the identified parameters and the wavenet learning rate. The comparison shows that Morlet, RASP1,RASP2, RASP3 are superior to the other wavelets.

Optimal control offers strong theoretical approach to high performance control. However, as far as the practical application is concerned, it suffers from the computational challenge in solving the Riccati equation. Wavelets offer feasible reduction on computations in solving the Riccati equation, and they can be used as bases for the approximation methods of computing the feedback control. The Haar wavelet is the most employed wavelet for solving the Riccati and the Riccati-like equations due to its operational matrices and simple closed form representation.

Chen and Hsiao [18] compared the computation time of the integral operational matrix formed by different orthogonal functions and found that the Haar wavelet operational matrix is the fastest. Such result could explain why the Haar wavelet is the most employed wavelets for feedback control computation.

Hsiao and Wang [50] extended their analysis of systems to solving the optimal control problem of LTI systems. Based on their solution of the LTI system, they used the backward integration to solve the adjoint equation of the optimal control problem. Liu and Zhang [83] presented another solution where they expanded the, input, state, and initial state vectors by the Haar wavelets as besis and substituting the expansion into the state space equation

and then forming a new Riccati equation, which can be solved algebraically.

Ding and Gu [31] used the properties of the Haar wavelet to design boundary predictive control for distributed parameter systems. Shojaeizadeh and Babolian [117] used the Rationalized Haar wavelets with the to solve the optimal control problem of singular TV systems. They followed a close line of solution to Hsiao and Wang [50]. Biswas et al. [13] compared the Haar wavelet solution with an analytically obtained solution and showed error in the order of 10^{-5} for 8-level Haar MRA and 10^{-9} for 64-level Haar MRA.

As an example on electrical applications, Gandelli and Leva [37] used the Haar wavelet to analyze the chopper voltage control circuit of a DC motor. Then, they implemented the electronic components of the controller by an equivalent Haar expansion.

Haar wavelets are not the only wavelets family that has been applied to quadratic optimal control problems; Poterasu [106] defined a cubic spline wavelet and used it as interpolation to solve the quadratic control problem of a nonlinear multibody system, and Ebrahimi et al. [34] solved the optimal control problem of singular systems but using the Legendre wavelets.

Wavelets were also used to form wavenets or Wavelet Neural Networks (WNN), which are neural networks whose neuron functions are the wavelet bases, while the network weights used are the coefficients of the wavelet basis. Zhang and Benveniste [147] were the first to propose Wavelet networks. They proposed them as an "alternative to feedforward neural networks for approximating arbitrary nonlinear functions".

Wavenets found considerable use in control synthesis and controllers design. The fact that wavenets can approximate any relation is the key property for such use. Chen and Cheng [17] used wavenets to approximate a nonlinear Multi-Input-Multi-Output (MIMO) system and designed adaptive control laws and parameter update algorithms to achieve H_∞ tracking performance. Chen and Lin [20] applied the same use of wavenets for uncertain multivariable nonlinear systems but with Sliding Mode Control (SMC). Chen et al. [21] applied wavelet network adaptive SMC to a Skid-To-Turn (STT) nonlinear anti-ship missile system. Lin et al. [80] also designed a WNN control system based on adaptive SMC. Their controller consists of a WNN to learn the ideal equivalent control law to the SMC in addition to a robust controller to meet the sliding mode conditions. Both the WNN adaptive learning algorithm and the bound estimation algorithm of the robust controllers were derived based on the Lyapunove stability criterion. Also, Karimi et al. [61] designed an adaptive wavelet controller that achieves H_∞ performance, and Ho et al. [47] introduced the Fuzzy Wavelet Networks (FWN) as a variation of wavelet networks that can also be used to approximate arbitrary nonlinear functions. Zekri et al. [146] designed a FWN representation for nonlinear controllers, while Wu et al. [137] used similar strategy to control a 3DOF mobile robot manipulator.

The presented survey shows the diverse methods and applications of wavelets in systems design and control. The major wavelets used are Morlet, Daubechies, Cauchy, Haar, and the Harmonic wavelets. There are other functions used as pseudo wavelets as well. Pseudo

wavelets are functions that do not satisfy all the wavelets conditions but possess desirable characteristics, so we can use them for feature extraction through dot product with signals. Morlet, Cauchy, and the Harmonic wavelets have direct relation between scale and frequency, which enables using these wavelets for direct time-frequency analysis of systems and signals. The methods used can be categorized according to different ways: the wavelet type, the analyzed systems, the dynamic model, whether applied to input, output or both, and whether applied to the differential or the integral of the signals.

1.1.1 Underdamped second-order LTI systems impulse response as a pseudo wavelet

Freudinger et al. [36] used the exponentially decaying complex harmonic function and called it the Laplace Wavelet, which is defined in Equation (2.31). They defined and used a dictionary of wavelets with the varying parameters ω, ζ, and τ. They correlated the output signal with every wavelet in the dictionary through the inner product $< \psi_\gamma(t), y(t) >$, then they computed the correlation coefficient κ_γ for each parameters' vector $\gamma = \{\omega, \zeta, \tau\}$. Afterwards, they defined $\kappa(\tau)$ as the maximum value of κ_γ at each τ and let $\bar{\omega}$ and $\bar{\zeta}$ be the parameters at that peak value. The obtained parameters characterize the modal properties of the system. Hou and Hera [48] proposed pseudo wavelet in the frequency domain. The proposed pseudo wavelet is the FRF

$$\Psi(\omega, \omega_0, \zeta_0) = \begin{cases} \eta \frac{\omega_0^2}{\sqrt{(\omega^2 - \omega_0^2)^2 + (2\zeta_0\omega_0\omega)^2}} & \omega \geq 0 \\ 0 & \omega < 0 \end{cases}, \tag{1.11}$$

where η is a normalizing factor. They defined the pseudo wavelet transform in the frequency domain by

$$W_\omega(\omega_0, \zeta_0) = \int_0^\infty F(\omega)\Psi(\omega, \omega_0, \zeta_0)d\omega. \tag{1.12}$$

If $F(\omega)$ is the FRF of a SDOF system, then the integration in Equation (1.12) is maximum when the damping ratio of the system is equal to ζ_0 and the natural frequency is equal to ω_0 [48]. The parameters can be identified at the peaks of $\zeta - \omega$ domain. This method shows good results with SDOF systems, but with MDOF systems they proposed a truncated pseudo wavelet transform [49] to overcome the interference between modes. They truncated the wavelet by locating a local maximum, appropriately selecting amplitude-to-peak ratio, and determining a frequency range in the neighborhood of the peak of the function in Equation (1.11).

It was a notable coincidence, when Robinson [110] used the term wavelet decades before Morlet et al. [94] to describe the response of LTI systems. Surprisingly, he defined the wavelet as a one sided L^2 stable time function $w(t)$, and defined the following two properties

$$w(t) = 0, \quad t < 0 \tag{1.13}$$

$$\int_0^\infty |w(t)|^2 dt < \infty. \tag{1.14}$$

Robinson referred to the response of 2nd order LTI systems by "wavelet", so he defined the Laplace pseudo wavelet shown in Equation (2.31), and called it a wavelet before the modern concepts of wavelet and pseudo wavelet were developed.

1.2 Contribution

The contributions this study added so far can be summarized by four major points; proving that the impulse response of second-order LTI systems can function as a none-compactly supported wavelet with major wavelets capabilities, defining the major properties and finding analytical formulas for the continuous wavelet transform of the elementary signals using the new wavelet, producing improved spectrograms using the new wavelet, addressing the edge effect that reduces spectrograms qualities at both ends and proposing the Reverse Wavelet Transform (RWT) as a solution to this problem.

The impulse response of second-order LTI systems is a natural signal that linear systems produce in nature. Being available as a wavelet for a wavelet transform with scale and time shift is desired because Engineers desire to perform time-frequency analysis of systems using a kernel that carries systems' properties. The SOULTI wavelet meets this criterion more than the other available wavelets which does not represent any natural process.

The SOULTI wavelets are extended to the complex-domain and the Laplace complex wavelet is produced. The major properties of derivation, differentiation, and time-frequency resolution are found for the Laplace wavelet. The Laplace wavelet transform can be evaluated for the elementary signals efficiently and can be derived from the Laplace transform.

One of the major difficulties in dealing with wavelets and wavelet transform is the difficulty of evaluating the transform even for simple signals, and sometimes there is no close form solution for the transform. Having an analytical formula for the transform enables the systems dynamics engineers to predict and then identify the behavior of system from their time-frequency response. Furthermore, the existence of a transform formula ease the process of finding the ridges and skeleton of a signal in the time-frequency domain. The ridges and their corresponding skeletons carry important information about signals and systems since they show where the concentration of energy takes place in terms of time and frequency.

Spectrograms are mappings that offer a way for tracking how the spectrum is evolving with time. The standard way of producing spectrograms is through using STFT. These spectrograms suffer from two problems. First, we have to guess on the suitable analysis window before we start, and sometimes we have to iterate using different window sizes to arrive at a satisfactory spectrogram. Second, the results are truncated from both ends along the time axes. The length of truncation depends on the analysis window size. So the result is missing information about the beginning and end of signals. The SOULTI wavelet overcomes

both problems. The wavelet transform inherently excels over STFT because the analysis window width changes by changing the scale/frequency. Also, the wavelet transform does not truncate any part of the answer and offers full range analysis. However, it suffers from the edge effect at the end, but this study is proposing a solution that mitigate significantly the edge effect.

The edge effect is described in detail in the following sections. It affects the quality of the transform at both ends of the time range. So the beginning and the end of the signal have both distorted transforms. As a solution to this problem the RWT is proposed. The RWT performs the wavelet transform but starting from the end of the signal and proceeding reversely to the beginning. This shows edge effect at the beginning of the signal. Therefore the average of the Forward Wavelet Transform (FWT) and the RWT mitigates the edge effect at both ends and gives smoothed or filtered results.

The LWT and the SWT are proved to represent the particular solution of linear first order and second order differential equations respectively. This result is essential for using the LWt and the SWT in modal parameters identification, and it is used for laying the foundation for accurate system identification methodology.

Chapter 2

Wavelets

2.1 General properties

Wavelets can be classified into orthogonal, biorthogonal, and pseudo wavelets. Pseudo wavelets are wavelets that do not have inverse wavelet transform. However, there are wavelets that do not have exact inverse wavelet transform but have approximate inverse. Within this category falls famous wavelets such as the Morlet and the Mexican hat wavelets. Therefore, we are categorizing these with wavelets, and including the weaker functions with the pseudo wavelet category.

Wavelets, in the modern sense, appeared first in the works of Morlet et al. [94] on seismic signals, where they adapted the STFT with Gabor Window (the Gabor Transform) by adding a scaling parameter to change the signal time scale. Daubechies [28] introduced the orthogonal wavelets, though, decades before Daubechies, Haar [44], through his work on orthogonal function systems, discovered the first orthogonal family of wavelets, the Haar wavelets.

The STFT and the WVD have limitations over Wavelets that must be explored. The STFT is defined as

$$\hat{f}(\tau, \omega) = \int_{-\infty}^{\infty} g(t)^*_{\tau,\omega} \cdot f(t)\ dt, \tag{2.1}$$

where "*" denotes the conjugate and $g(t)_{\tau,\omega}$ is defined by

$$g(t)_{\tau,\omega} = g(t - \tau) \cdot e^{-j \cdot \omega}, \tag{2.2}$$

where $g(t)$ is the window function, and τ is the translation variable.

The window function has a constant width, which is a shortcoming of the STFT. This fixed width makes the analysis of signals containing frequencies much smaller or larger than the reciprocal of the window width inaccurate. If the time period is much larger than the window

width, then the corresponding frequency will not appear in the spectrum, and if the time period is very short, the corresponding frequency will have poor time localization. Moreover, transient variations that last very short durations are not translated into the spectrum.

The WVD of a signal $x(t)$ is the Fourier transform of its instantaneous auto-correlation at time t and is defined by [23]

$$WVD(t,\omega) = \frac{1}{2\pi}\int_{-\infty}^{\infty} x\left(t+\frac{\tau}{2}\right) x^*\left(t-\frac{\tau}{2}\right) e^{-j\omega\tau} d\tau. \tag{2.3}$$

The WVD has strong limitations. The first limitation is the crossterm interference, which prevents using the WVD in any real application [108]. The second limitation comes from the integral limits of Equation (2.3), which extends infinitely before and after the time concerned. Consequently, the distribution is suitable for post-collection data processing but not for online processing.

Wavelets overcome the limitations of the WVD and the shortcomings of the fixed window width in the STFT. Wavelets have a scaling variable a, also called the dilation variable, which changes the width of the analysis window and changes the frequency bandwidth of the wavelet instead of only changing the frequency as in the case of the STFT. So if a function $\psi(t)$ is the fundamental analyzing function, or the mother wavelet, then

$$\psi_{\tau,a}(t) = \psi(\frac{t-\tau}{a}) \tag{2.4}$$

is the general form of the analyzing wavelet family $\{\psi_{\tau,a}(t)\}_{a,\tau\in\mathbb{R}}$. Substituting $\psi_{\tau,a}(t)$ instead of $g_{\tau,\omega}$, into Equation (2.1) yields the transform

$$W\{f(t)\} = \tilde{f}_{\tau,a} = \int_{-\infty}^{\infty} \psi_{\tau,a}(t)\cdot f(t)\ dt, \tag{2.5}$$

which is the wavelet transform. The analyzing wavelet has to satisfy certain conditions in order for the wavelet transform to have a meaning and be reversible; i.e., being able to obtain $f(t)$ from $\tilde{f}_{a,\tau}(t)$. These conditions can be found in [28, 42, 134], and we briefly summarize them. First, the transform must be finite, so

$$\lim_{t\to\pm\infty} \psi(t) = 0. \tag{2.6}$$

To guarantee the invertability of the transform in Equation (2.5) the following must hold

$$0 < \int_0^{\infty} \frac{|\Psi(\omega)|^2}{\omega}\ d\omega = C < \infty, \tag{2.7}$$

which is called the admissibility condition, where $\Psi(\omega)$ is the Fourier Transform of $\psi(t)$, and C is a finite constant. The admissibility condition says that the integration in Equation (2.7)

must be constant and bounded. Note that the condition in Equation (2.6) can be inferred from the admissibility condition. In addition, the wavelet family $\{\psi_{a,\tau}(t)\}_{a,\tau\in\mathbb{R}}$ has to span $L^2(\mathbb{R})$ and provide a compact support over it.

However, some applications require analyzing a signal to only extract certain features from it without caring about retrieving the original signal back. In such cases, less strict conditions apply to the mother wavelet. The reconstruction formula, or the inverse wavelet transform is given by

$$f(t) = \int_0^\infty \int_{-\infty}^\infty |a|^{-1} \upsilon_{\tau,a}(t)\ \tilde{f}(\tau, a)\ d\tau\ da \tag{2.8}$$

where $\upsilon_{a,\tau}(t)$ is the reconstruction wavelet corresponding to $\psi_{\tau,a}(t)$. For numerical applications, there is a simplified approximation of Equation (2.8) [128] that requires estimating only single integration or summation as shown in Equation (2.9)

$$f(t) \approx \frac{1}{C} \int_0^\infty \frac{\tilde{f}(\tau, a)}{a}\ da, \tag{2.9}$$

where C is the admissibility condition constant defined in Equation (2.7).

The wavelet transform had been generalized to the Fractional Wavelet Transform (FRWT) by Mendlovic et al. [92] as a parallel generalization to the Fractional Fourier Transform (FRFT) [114]. Mendlovic et al. [92] defined the FRWT as

$$W^\alpha\{f(t)\} = \tilde{f}_{\alpha,a,\tau} = \int_{-\infty}^\infty \int_{-\infty}^\infty \kappa_\alpha(\omega, t) \cdot f(t) \cdot \psi_{a,\tau}(\omega)\ dt\ d\omega, \tag{2.10}$$

where κ_α is the transform kernel, which can take different definitions [92, 107, 114, 116]. One possible definition is the same definition as the FRFT kernel, which is given by

$$\kappa_\alpha(\omega, t) = \begin{cases} \sqrt{\frac{1-j\cot(\alpha)}{2\pi}} e^{j\frac{\omega^2+t^2}{2}\cot(\alpha) - j\omega t \csc(\alpha)} & \alpha \neq k\pi \\ \delta(t-\omega) & \alpha = 2k\pi \\ \delta(t+\omega) & \alpha = (2k-1)\pi \end{cases}. \tag{2.11}$$

Depending on the kernel and how α is defined the FRWT can take different meanings. Note that the FRWT takes the fraction parameter α in addition to scale, a, and time shift, τ. When using Equation (2.11) for the kernel, the FWRT transform becomes the conventional wavelet transform if $\alpha = \pi/2$.

Wavelets can localize signal characteristics in the time-frequency domain. However, there is a lower bound on the localization uncertainty that any wavelet function or analyzing window function can achieve [59, 134]. This lower bound is determined by the uncertainty principle, also called the Heisenberg principle. The principle states that the resolution in both frequency and time domain cannot become arbitrarily small. Mathematically, the

localization window in the time-frequency domain defined by $\triangle t \cdot \triangle \omega$ is bounded by the inequality

$$\triangle t \cdot \triangle \omega \geq \frac{1}{4\pi} \tag{2.12}$$

where the inequality becomes equality for the Gaussian signal.

The most used wavelet in systems analysis, especially for system identification purposes, is the Morlet wavelet named after Jean Morlet [94]. Though the Morlet wavelet is the first wavelet of the modern wavelets, it is actually a pseudo wavelet. However, it can be approximated as a wavelet with inverse wavelet transform. The Morlet wavelet came from the Gabor transform; Morelet himself called the Morlet wavelet the Gabor wavelet [94], which is the Gaussian window applied to the complex harmonic function,

$$g(t) = e^{j\omega_o|t|}e^{-t^2/2}, \tag{2.13}$$

where ω_o is the basic or the fundamental frequency. With the Morlet wavelet, direct link between frequency and scale can be established [125], where the value of the scale a_ω, at which the wavelet is focused on frequency ω, is given by

$$a_\omega = \frac{\omega_o}{\omega}. \tag{2.14}$$

Lin and Qu [81] presented a parameter optimization method for the Morlet wavelet in feature extraction applications such as fault diagnosis. The method depends on minimizing the wavelet entropy. The idea of minimizing the signal entropy was first proposed by Coifman and Wickerhauser [25] for best bases selection. However, Lin and Qu [81] employed the entropy minimization for parameter optimization. If $\{c_i\}_{i=1,\ldots,M}$ are the wavelet coefficients, then the normalized coefficients are given by

$$d_j = \frac{c_j}{\sum_{i=1}^{M} c_i}, \tag{2.15}$$

and the wavelet entropy is defined by [81]

$$En = -\sum_{i=1}^{M} d_i \; log \; d_i. \tag{2.16}$$

An additional parameter ς is introduced inEquation (2.13), as shown in Equation

$$g_\varsigma(t) = e^{j\omega_o|t|}e^{-\varsigma^2 t^2/2}. \tag{2.17}$$

Then the entropy is calculated for a range of the parameter ς, while the value that minimizes Equation (2.16) is the optimal parameter, and the corresponding wavelet is the optimal wavelet.

2.2 Multiresolution analysis and orthogonal wavelets

Multiresolution Analysis (MRA) was first introduced by Mallat [87]. However, the first family of orthogonal functions that formed an MRA were discovered by Haar [44]. In MRA, a function $f(t) \in L^2(\mathbb{R})$ is decomposed into subspaces divided between scales and details. The scale subspaces $\{V_j\}_{j\in\mathbb{Z}}$ satisfy the following: $\cap_{j\in\mathbb{Z}}\{V_j\} = \{0\}$; the spaces V_j are generated by a function $\phi(t)$ called the scaling function such that $\phi(t-k)$ spans V_0 and $\phi(2^j t-k)$ spans V_j, $k \in \mathbb{Z}$; V_j are nested, i,e, $V_{-1} \subset V_0 \subset V_1$...; if $f(t) \in V_0$ then $f(2t) \in V_1$ and $f(2^j t) \in V_j$. The details W_j represent the difference between the subspaces V_j and V_{j+1}, so $W_j \perp V_j$ and satisfies

$$V_{j+1} = V_j \oplus W_j. \tag{2.18}$$

The functions that span W_0 are the translations of a mother wavelet $\psi(t)$ derived from $\phi(t)$ and the multiresolution properties [27, 87] ; hence, $span(W_0) = \{\psi(t-k)\}_{k\in\mathbb{Z}}$ and in general,

$$span(W_j) = \{\psi(2^j t - k)\}_{k\in\mathbb{Z}}. \tag{2.19}$$

Usually, orthogonal wavelets are not expressed by a closed form relation; instead, they are expressed by a dilation equation. The dilation equation of a scaling function is given by

$$\phi(t) = \sum_{k=0}^{N-1} c_k \phi(2t - k), \tag{2.20}$$

where c_k are the equation coefficients and N distinguishes a wavelet family from another. It is not possible to find the c_ks from Equation (2.20), but from the iteration algorithm described by

$$\phi_j(t) = \sum_{k=0}^{N-1} c_k \phi_{j-1}(2t - k), \tag{2.21}$$

where the iteration continues until $\phi_j(t) = \phi_{j-1}(t)$. In addition to Equation (2.21), there are three types of conditions that produce N equations to solve for the N coefficients as Daubechies describes in [27]. The conditions are the conservation of area condition, the accuracy conditions, and the orthogonality conditions. We refer the reader to [27, 28] for the detailed description of these conditions. After finding the coefficients, the wavelet function or the detail function is given by the iteration equation

$$\psi_j(t) = \sum_{k=0}^{N-1} c_k \phi_{j-1}(2x - N - k + 1). \tag{2.22}$$

Orthogonal wavelets are suitable for DWT, and because the wavelet transform is similar to the convolution integral, the DWT becomes similar to the convolution sum. This observation leads to implementing the DWT using digital filter banks [133]. The algorithm decomposes the signal through stages; each stage represents a resolution level. In each level, two filters

decompose the signal; one is high pass filter and the other is low pass filter. The high pass filter output is not decomposed further and is put directly into the transform result. The low pass filter output is decomposed further by high pass and low pass filters. The process continues until the lowest level of resolution is reached, which depends on the number of samples in the signal. If the number of samples N is a power of 2 then the number of stages or multiresolution levels is $\log_2(N)$. If N is not a power of 2 then the signal is either padded by zeros or truncated to become a power of 2. The algorithm can be described by Figure 2.1.

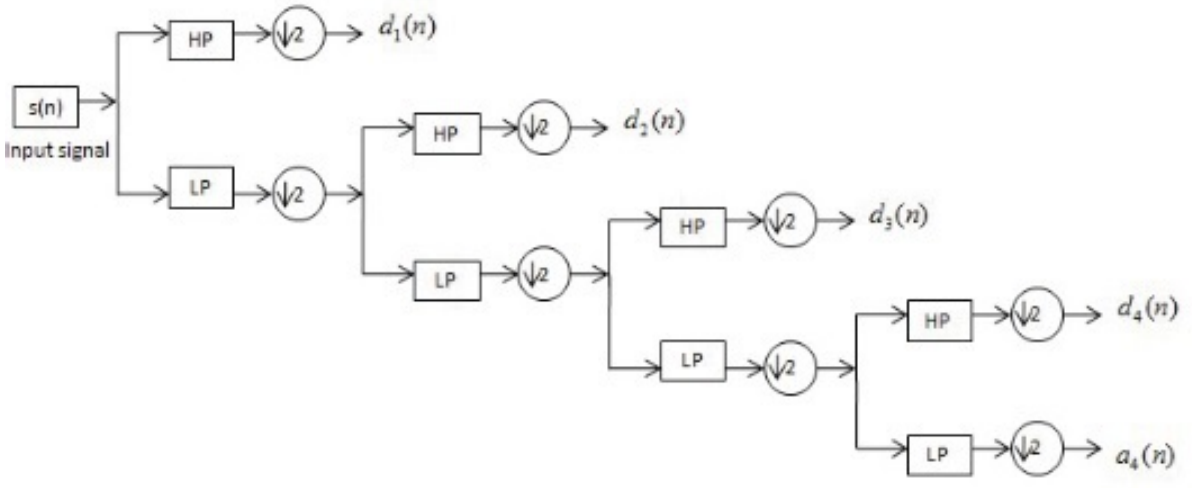

Figure 2.1: Decomposition of a signal into four-level MRA based on Mallat Algorithm [43]. © 2011 IEEE.

The DWT decomposes the signal into octave-bands, which compromises the frequency resolution at higher frequency levels. To overcome this negativity, two decomposition methods were proposed. The first is the matching pursuits algorithm [88], and the second is the Discrete Wavelet Packet Transform (DWPT), which decomposes the signal into equal frequency sub-bands [25]. The DWPT algorithm decomposes the output of the high pass filter in the next stage by another pair of high pass and low pass filters similar to the output of the low pass filter. Figure 2.2 illustrates the DWPT algorithm.

2.3 Harmonic wavelets

Harmonic wavelets are an important class of orthogonal wavelets. Newland [100] noticed that as the number of coefficients in the dilation Equation (2.22) increases, the Fourier transform of the wavelet approaches a box shape. Then, he let the number of coefficients increase infinitely and proposed a wavelet whose Fourier transform is given by the box function

$$\Psi(\omega) = \begin{cases} \frac{1}{2\pi} & 2\pi \leq \omega < 4\pi \\ 0 & elsewhere \end{cases} . \tag{2.23}$$

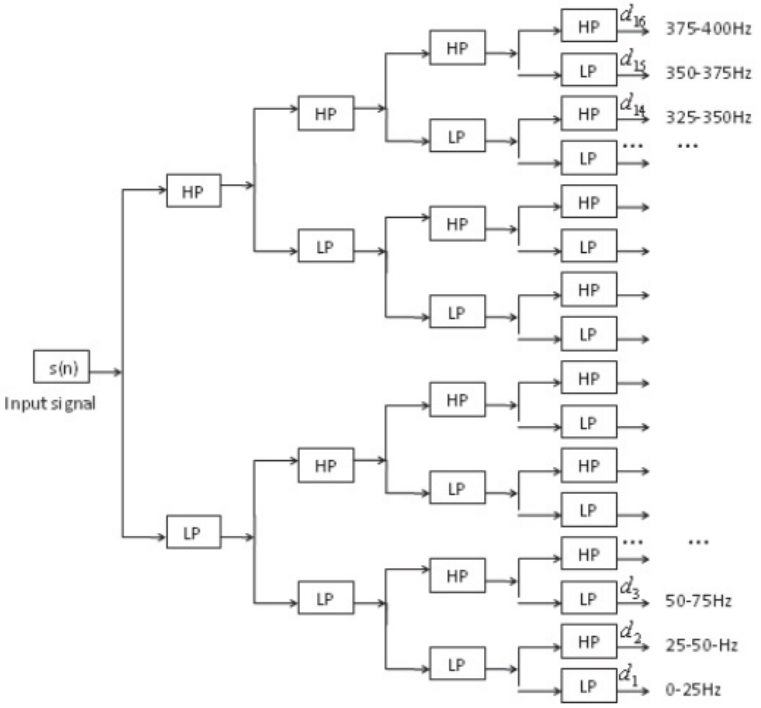

Figure 2.2: Four-Level DWPT decomposition tree [43]. © 2011 IEEE.

The inverse Fourier transform of Equation (2.23) reads

$$\psi(t) = \frac{e^{i4\pi t} - e^{i2\pi t}}{i2\pi t}, \tag{2.24}$$

which gives the harmonic mother wavelet whose bandwidth is $2\pi \leq \omega < 4\pi$ in time domain, and its scaling function is given by

$$\phi(t) = \frac{e^{i2\pi t} - 1}{i2\pi t}, \tag{2.25}$$

which is obtained from the inverse Fourier transform of

$$\Phi(\omega) = \begin{cases} \frac{e^{-i\omega k}}{2\pi} & 0 \leq \omega < 2\pi \\ 0 & elsewhere \end{cases}. \tag{2.26}$$

Newland [97, 98] proposed the harmonic wavelets for vibrations analysis because the most important property these wavelets possess beside orthogonality is the ability to control precisely the frequency bandwidth they cover.

The Littlewood-Paley (L-P) wavelets [8] are bases functions equivalent and closely related to the Harmonic wavelets family. The L-P wavelet is defined by

$$\psi = \frac{1}{2\pi} \frac{\sin(4\pi t) - \sin(2\pi t)}{t}. \tag{2.27}$$

The modified L-P wavelet [10] is obtained by introducing a tuning parameter $\sigma > 1$ for modifying the frequency band as follows

$$\psi_{L-P} = \frac{1}{\pi\sqrt{\sigma - 1}} \frac{\sin(4\pi t) - \sin(2\pi t)}{t}. \tag{2.28}$$

Recently, the Morse wavelets, which resemble probability distributions in the frequency domain, were introduced as super analytical wavelets with two controlling parameters that control the shape and behavior of the wavelet in the time and frequency domains [79]. The continuous Morse wavelet transform is defined in the frequency domain as

$$\Psi(\omega) = U(\omega) b_{\beta,\gamma} \omega^{\beta} e^{-\omega^{\gamma}} \tag{2.29}$$

where b is a normalizing constant, $U(\omega)$ the step function, γ the symmetry parameter, and β the decay parameter. The Morse wavelet attains its peak value in the frequency domain at a frequency equal to

$$\omega_{\beta,\gamma} = \left(\frac{\beta}{\gamma}\right)^{\frac{1}{\gamma}} \tag{2.30}$$

2.4 Pseudo wavelets

Pseudo wavelets are functions that do not satisfy all the requirements of wavelets but are useful for signal analysis [48]. Associated with them is a Pseudo-Wavelet Transform (PWT). However, in many cases, the Inverse Pseudo-Wavelet Transform (IPWT) is not available since the pseudo mother wavelet does not satisfy the admissibility condition defined in Equation (2.7). Wavelets are either redundant sets of generalized frames that are linearly dependent or orthogonal or bi-orthogonal bases for the $L^2(\mathbb{R})$ space [59]. The term *dictionary* is sometimes used for a set of pseudo wavelets [36] as they are similar in concept to the Time-Frequency dictionaries introduced by Mallat and Zhang [88].

Pseudo wavelets have been used for systems and signals analysis because they give more freedom in choosing the analyzing function. Almost any function that is closely related to a system's behavior or a signal's feature can be employed as a pseudo wavelet, so it detects that system's behavior or extracts that signal's feature. For example, the impulse response function of a 2nd order LTI system is employed as a pseudo wavelet and is called the *Laplace Pseudo Wavelet* or *Laplace Wavelet* [36, 148],

$$\psi(f, \zeta, \tau, t) = \psi_{\gamma}(t) = \begin{cases} A e^{\frac{-\zeta}{\sqrt{1-\zeta^2}} 2\pi f(t-\tau)} e^{-j2\pi f(t-\tau)} & t \in [\tau, \tau + T_e] \\ 0 & else \end{cases}. \tag{2.31}$$

The vector $\gamma = [f, \zeta, \tau]$ represents the changing parameters, and T_e is the effective duration of the wavelet that guarantees a compact support and a finite non-zero length of the wavelet. Pseudo wavelets are used in vibrations analysis and system identification as explained in more details in the following sections.

2.5 Ridges and skeletons

Ridges and Skeletons are part of wavelets' time-scale maps. The ridge of the wavelet transform is the set of points in the time-scale domain where the wavelet integral has stationary points [128]; $(a, b) \in \Omega$ such that $t_s(a, b) = b$, where t_s is a stationary point. On ridges, the scale a satisfies the relation [128]

$$a = a_r(b) = \frac{\theta'_\psi(0)}{\theta'_x(b)}, \tag{2.32}$$

where θ_ψ is the wavelet phase, and θ_f is the analyzed signal phase. The values of the wavelet transform restricted to its ridges are called the skeleton of the wavelet transform [128]. The importance of ridges and skeletons comes from the observation that the energy of signals is concentrated on the skeleton of their wavelet transform. The skeleton is approximated by the relation [128]

$$W\{x(t)\}\Big|_{(r(b),t)} \approx C(t)Z(t), \tag{2.33}$$

where $C(t)$ is a correction factor, and $Z(t)$ is the analytic signal of $x(t)$ given by

$$Z(t) = x(t) + j\tilde{x}(t), \tag{2.34}$$

where $\tilde{x}(t)$ is the Hilbert transform of $x(t)$.

Chapter 3

SOULTI Wavelets

The content of this chapter is extracted from a study by the author of this dissertation that is published in the Journal of Vibration and Control [2].

The response of underdapmed second-order LTI systems has been used before as pseudo wavelet to analyze signals for system identification as presented in Section 1.1.1. However, can be considered full wavelets since after their inner product with the signal, it is possible to retrieve the original signal back as will be shown in the following sections.

3.1 SOULTI wavelet transform

Second order LTI systems are very common in most dynamic fields of science. The mechanical mass-spring-damper system, shown in Figure 1.a, and the RLC-electrical circuit, shown in Figure 1.b, are typical examples of such systems. The response of the second order underdamped LTI system in Figure 3.1, for the impulse input $\omega_n^2\ \delta(t)$ is given by

$$h(t) = \left(\frac{\omega_n}{\sqrt{1-\zeta^2}} \right) e^{-\zeta\omega_n t} \sin(\omega_n \sqrt{1-\zeta^2} t) u(t) \tag{3.1}$$

where $\zeta < 1$ is the damping ratio, ω_n is the natural frequency and $u(t)$ is the Heaviside step function. The impulse input is scaled by ω_n^2 to simplify the derivation of the frequency properties in Sections 3.3 and 3.4, hence

$$\int_{-\infty}^{\infty} \delta(t) dt = \omega_n^2 \tag{3.2}$$

The damped frequency ω_d is defined by

$$\omega_d = \omega_n \sqrt{1-\zeta^2} \tag{3.3}$$

so Equation (3.3) can be rewritten in terms of ω_d as

$$h(t) = \left(\frac{\omega_d}{1-\zeta^2}\right) e^{-\zeta \frac{\omega_d}{\sqrt{1-\zeta^2}} t} \sin(\omega_d t) u(t) \tag{3.4}$$

Let the reciprocal of the damped frequency, defined in Equation (5), be the scaling parameter as

$$a = \frac{1}{\omega_d} \tag{3.5}$$

Substitute Equation (3.5) into Equation (3.4) to get

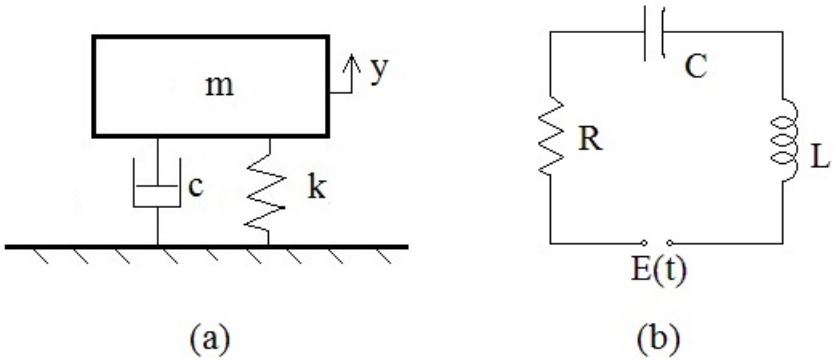

Figure 3.1: (a) Mass-spring-damper system (b) R-L-C electrical circuit

$$h(t) = \left(\frac{a^{-1}}{1-\zeta^2}\right) e^{-\zeta \frac{\frac{t}{a}}{\sqrt{1-\zeta^2}}} \sin(\frac{t}{a}) u(t) \tag{3.6}$$

which is the impulse response in terms of the scaling parameter a where $a \in (0, \infty)$. Now, the SOULTI wavelet can be defined as

$$\psi_\zeta^{\tau,a} = \psi_\zeta \left(\frac{t-\tau}{a}\right) = \left(\frac{a^{-p}}{1-\zeta^2}\right) e^{\frac{-\zeta}{\sqrt{1-\zeta^2}}\left(\frac{t-\tau}{a}\right)} \sin(\frac{t-\tau}{a}) u(t-\tau) \tag{3.7}$$

which represents the real part of the Laplace wavelet defined by Freudinger et al. [36]. If f(t) is right handed signal or function, i.e. $f(t) = 0 \forall t < 0$, the SOULTI wavelet transform of $f(t)$ is now defined by the generic continuous wavelet transform definition,

$$\tilde{f}_\zeta(\tau, a) = \int_{-\infty}^{\infty} f(t) \psi_\zeta(\frac{t-\tau}{a}) dt, \quad , \tau \in (-\infty, \infty) \tag{3.8}$$

Equation (3.7) defines more than one family of wavelets, such that each family is linked to a value of ζ, where $0 < \zeta < 1$. The parameter p is used to give the wavelet a preservation property. For example, when the wavelet is scaled, its energy content is also scaled, so to

preserve the energy under scaling use $p = 1/2$. However, to preserve the l^1 integration of the wavelet, namely

$$\int_{-\infty}^{\infty} \psi_\zeta(\frac{t}{a})dt = \int_{-\infty}^{\infty} \psi_\zeta(t)dt \tag{3.9}$$

use p=1. Figure 3.2 graphs the SOULTI wavelet versus time showing its time properties. The SOULTI wavelet presented here retains the LTI second order response characteristics

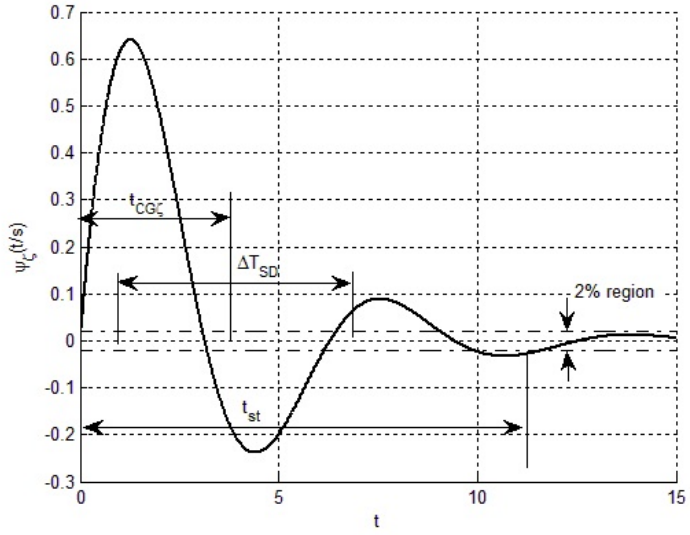

Figure 3.2: A SOULTI wavelet function with different properties defined. $\zeta = 0.3$, $a = 1$, and $p = 1$.

completely. It offers the potential to measure the similarity between any signal and the response of second order LTI systems for characterization and identification purposes. In addition, it gives direct and simple relationship between scale and frequency as shown in Equation (3.5), where the frequency is the reciprocal of the scale.

3.1.1 Region of convergence

The region of convergence of the SOULTI transform defines the region $\Gamma \subset S \times T$, where $a \in S = (0, \infty), \tau \in T = (-\infty, \infty)$, in which the transform in Equation (3.8) converges to a finite value. Before exploring such region, notice that $f(t)$ has to be exponentially bounded in order for the transform in Equation (3.8) to converge.

Definition 3.1. Suppose that $\rho < \infty$, then let $J \subset (\rho, \infty) \subset R$ and $f(t) : J \to R$. If there exists $\alpha, k \in R$ such that $|f(t)| \leq |k.e^{\alpha t}| \forall t \in J$, then $f(t)$ is exponentially bounded ■

If $f(t)$ is exponentially bounded, then the SOULTI transform is convergent for the scale region

$$0 < a < \frac{\zeta}{\alpha\sqrt{1-\zeta^2}} \tag{3.10}$$

The convergence depends also on the time shift of the transform. For example, a function $f(t)$ with $\lim_{t\to t_0} = \infty$, while $f(t) < L_u < \infty \ \forall \ t > t_0$ may not yield a convergent transform for $\tau < t_0$ while the transform is convergent for $\tau > t_0$. Therefore, the time region has to be explicitly indicated on the transform, especially if the transform is done on part of the defined domain of the function. Besides, the transform is equal for two functions that are identical everywhere except on a set of measure zero. In the next section, we will define the inverse continuous wavelet transform with respect to the SOULTI wavelet.

3.2 SOULTI wavelet inverse transform

Notice that Equation (3.8) represents an inner product in the time domain, which is equivalent to the inner product in the frequency domain according to the Plancherel's identity. Applying the identity to Equation (3.8) yields

$$\tilde{f}_\zeta(\tau, a) = \langle \psi_\zeta^{\tau,a}, f(t) \rangle = \langle \Psi_\zeta^{\tau,a}(\omega), F(\omega) \rangle \tag{3.11}$$

where $\Psi_\zeta^{\tau,a}(\omega)$ is the Fourier transform of $\psi_\zeta^{\tau,a}$, and using the Fourier transform shift and scale properties it can be expressed in terms of the mother wavelet Fourier transform $\Psi_\zeta(\omega)$ by

$$\psi_\zeta^{\tau,a} = a e^{-j\omega t} \Psi_\zeta(a\omega) \tag{3.12}$$

Using Parseval's identity, Equation (3.8) becomes

$$\tilde{f}_\zeta(\tau, a) = \frac{a}{2\pi} \int_{-\infty}^{\infty} e^{j\omega t} \overline{\Psi_\zeta(a\omega)} F(\omega) d\omega \tag{3.13}$$

where the conjugate of $\psi_\zeta^{\tau,a}$ is applied in the inner product. Note that the integral in the right side of Equation (3.13) represents the inverse Fourier transform of $\bar{\Psi_\zeta}(a\omega)F(\omega)$. Applying the Fourier transform to Equation (3.13) yields

$$\int_{-\infty}^{\infty} e^{-j\omega\tau} \tilde{f}_\zeta(\tau, a) d\tau = \frac{a}{2\pi} \overline{\Psi_\zeta(a\omega)} F(\omega) \tag{3.14}$$

In general, we cannot divide both sides by $a\overline{\Psi_\zeta(a\omega)}$ because it could vanish at some values of ω or a. However, in our case $a\overline{\Psi_\zeta(a\omega)}$ is given by

$$a\overline{\Psi_\zeta(a\omega)} = \frac{\frac{a^{1-p}}{1-\zeta^2}}{-\omega^2 a^2 + \frac{1}{1-\zeta^2} - j\frac{2\zeta\omega a}{\sqrt{1-\zeta^2}}} \tag{3.15}$$

which does not vanish for any value of ω or $a \in (0, \infty)$. Figure 3.3 shows the wavelet spectrum, which is equivalent to its conjugate spectrum. The curve never crosses the zero axis and decays asymptotically to zero. Consequently dividing by $a\overline{\Psi_\zeta(a\omega)}$ is a legitimate operation. Therefore, we can solve for $F(\omega)$ in Equation (3.14) to get

$$F(\omega) = \frac{2\pi}{a\overline{\Psi_\zeta(a\omega)}} \int_{-\infty}^{\infty} e^{-j\omega\tau} \tilde{f}_\zeta(\tau, a) d\tau \tag{3.16}$$

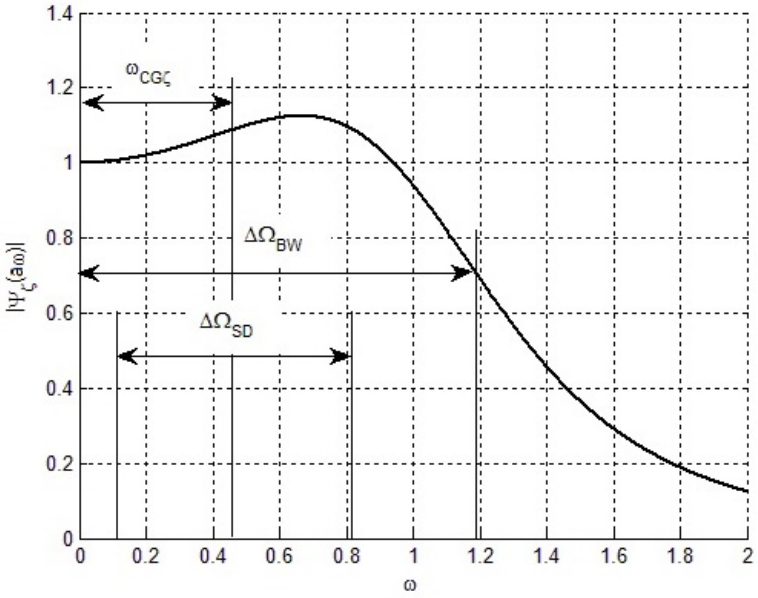

Figure 3.3: A SOULTI frequency domain function showing the mean frequency $\omega_{CG\zeta}$, the standard deviation-based frequency window $\Delta\Omega_{SD}$, and the (half-power)-based frequency window $\Delta\Omega_{BW}$. $\zeta = 0.5$, $a = 1$, and $p = 1$

To retrieve $f(t)$, take the inverse Fourier transform of Equation (18), so the inverse wavelet transform with respect to the SOULTI wavelet becomes

$$f(t) = \int_{-\infty}^{\infty} \int_{-\infty}^{\infty} \frac{e^{j\omega t}}{a\overline{\Psi_\zeta(a\omega)}} e^{-j\omega t} \tilde{f}_\zeta(\tau, a) d\tau d\omega \tag{3.17}$$

Equation (3.17) forms the inverse wavelet transform with respect to the SOULTI wavelet or the reconstruction formula of the original wavelet definition shown in Equation (3.8). If $f(t)$ is differentiable, we can use a simpler and probably more practical inverse formula to retrieve $f(t)$ back from its wavelet transform.

3.2.1 SOULTI wavelet reconstruction identity

Theorem 3.2. *Let J be as defined in Section 3.1.1, and let $f(t) : J \to R$ be differentiable and exponentially bounded, see Section 3.1.1, and the SOULTI wavelet transform of $f(t)$ is*

given by Equation (3.8)*, then the inverse wavelet transform is given by*

$$f(t) = a^{p-1}\left[(1-\zeta^2)a^2\frac{d^2}{dt^2}\left(\tilde{f}_\zeta(\tau,a)\right) - 2\sqrt{1-\zeta^2}\zeta a\frac{d}{dt}\left(\tilde{f}_\zeta(\tau,a)\right) + \tilde{f}_\zeta(\tau,a)\right] \tag{3.18}$$

Proof: Substituting $s\overline{\Psi_\zeta(a\omega)}$ from Equation (3.15) into Equation (3.17) gives

$$f(t) = \int_{-\infty}^{\infty}\frac{e^{j\omega t}\left(1-\zeta^2\right)}{a^{1-p}}\left(-\omega^2a^2 + \frac{1}{1-\zeta^2} - j\frac{2\zeta\omega a}{\sqrt{1-\zeta^2}}\right)\int_{-\infty}^{\infty}e^{-j\omega t}\tilde{f}_\zeta(\tau,a)d\tau d\omega \tag{3.19}$$

Using the operator notation for the Fourier transform, Equation (3.19) becomes

$$f(t) = a^{p-1}\mathcal{F}^{-1}1\left\{\left(-\omega^2a^2\left(1-\zeta^2\right) + 1 - j\sqrt{1-\zeta^2}2\zeta\omega a\right)\mathcal{F}\left\{\tilde{f}_\zeta(\tau,a)\right\}\right\} \tag{3.20}$$

Applying the linear operators properties [95] to Equation (3.20) gives

$$\begin{aligned} f(t) = {} & a^{p-1}\mathcal{F}^{-1}1\left\{-\omega^2a^2\left(1-\zeta^2\right)\mathcal{F}\left\{\tilde{f}_\zeta(\tau,a)\right\}\right\} + a^{p-1}\mathcal{F}^{-1}1\left\{\mathcal{F}\left\{\tilde{f}_\zeta(\tau,s)\right\}\right\} \\ & - a^{p-1}\mathcal{F}^{-1}1\left\{j\sqrt{1-\zeta^2}2\zeta\omega a\mathcal{F}\left\{\tilde{f}_\zeta(\tau,a)\right\}\right\} \end{aligned} \tag{3.21}$$

and after applying the Fourier transform differentiation property to Equation (3.21) we arrive at Equation (3.18) ■

This provides a simple and direct method in time domain to calculate the inverse wavelet transform with respect to the SOULTI wavelet. However, in order for the formula in Equation (3.18) to apply, $\tilde{f}_\zeta(\tau,a)$ has to be at least twice differentiable with respect to time. When considering the transform that defines $\tilde{f}_\zeta(\tau,a)$ in Equation (3.8), we find that $\tilde{f}_\zeta(\tau,a)$ is twice differentiable with respect to time if $f(t)$ is differentiable. So if $f(t)$ is exponentially bounded and $f(t) \in C^1$, then its SOULTI wavelet transform is unique and $f(t)$ can be retrieved using Equation (3.18).

Equation (3.18) also provides information about the uniqueness of the SOULTI wavelet transform. The inverse wavelet transform given by Equation (3.18) is a linear 2nd order differential equation, which we will call the *Reconstructing Differential Equation*. The original function $f(t)$ is the input function, and its wavelet transform is the solution or the response, which is unique if $f(t) \in l^1$. However, the other conditions must be satisfied in order for Equation (3.18) to server as inverse formula for the SOULTI wavelet transform.

3.2.2 Particular solution of 2nd order autonomous ODEs

Theorem 3.3. *Let J be defined as in Section 3.1.1, and let $f(t) : J \to \mathbb{R}$ be integrable and exponentially bounded, and let s_1 and s_2 be the roots of the accompanying characteristic*

equation of the autonomous non-homogeneous differential equation

$$f(t) = l\ \frac{d^2y(t)}{dt^2} + h\ \frac{dy(t)}{dt} + g\ y(t) \tag{3.22}$$

if $s_1 \neq s_2$*, then the particular solution of Equation* (3.22) *is given by the wavelet transform defined by*

$$y_p(t) = \int_t^{t_1} \psi(r-t) f(r) dr + K(t, t_1) \tag{3.23}$$

where $t \in J$*,* $K(t, t_1)$ *is a function that depends on the parameters of the differential equation and* t_1*, and* $\psi(t)$ *is defined by*

$$\psi(t) = \frac{e^{-s_2 t} - e^{-s_1 t}}{l(s_2 - s_1)} \tag{3.24}$$

Proof: The solution of the homogeneous version of Equation (3.22) is given by

$$y_h(t) = c_1 y_1(t) + c_2 y_2(t) = c_1 e^{s_1 t} + c_2 e^{s_2 t} \tag{3.25}$$

where s_1 and s_2 are given by

$$s_{1,2} = \frac{-h}{2l} \pm \frac{\sqrt{h^2 - 4lg}}{2l} \tag{3.26}$$

while the particular solution $y_p(t)$ is given by

$$y_p(t) = y_2(t) \int \frac{y_1(t) f(t)}{l\ W(y_1(t), y_2(t))} dt - y_1(t) \int \frac{y_2(t) f(t)}{l\ W(y_1(t), y_2(t))} dt \tag{3.27}$$

where $W(y_1(t), y_2(t))$ is the Wronskian of $y_1(t)$ and $y_2(t)$ and is given by

$$W(y_1(t), y_2(t)) = \begin{vmatrix} y_1(t) & y_2(t) \\ y_1'(t) & y_2'(t) \end{vmatrix} = (s_2 - s_1) e^{(s_1 + s_2)t} \tag{3.28}$$

substituting $y_1(t)$, $y_2(t)$, and $W(y_1(t), y_2(t))$ into Equation (3.27) and simplifying yields

$$y_p(t) = e^{s_2 t} \int \frac{e^{-s_2 t} f(t)}{l\ (s_2 - s_1)} dt - e^{s_1 t} \int \frac{e^{-s_1 t} f(t)}{l\ (s_2 - s_1)} dt \tag{3.29}$$

the indefinite integrals in Equation (3.29) can be rewritten in the form of definite integrals, so Equation (3.29) becomes

$$y_p(t) = e^{s_1 t} \int_t^{t_1} \frac{e^{-s_1 r} f(r)}{l\ (s_2 - s_1)} dr - e^{s_1 t} k_1(t_1) + e^{s_2 t} k_2(t_1) - e^{s_2 t} \int_t^{t_1} \frac{e^{-s_2 r} f(r)}{l\ (s_2 - s_1)} dr \tag{3.30}$$

where $k_1(t)$ and $k_2(t)$ are given by

$$\begin{aligned} k_1(t) &= \textstyle\int \frac{e^{-s_1 t} f(t)}{l\ (s_2 - s_1)} dt \\ k_2(t) &= \textstyle\int \frac{e^{-s_2 t} f(t)}{l\ (s_2 - s_1)} dt \end{aligned} \tag{3.31}$$

Collecting the terms and defining $K(t, t_1)$ as

$$K(t, t_1) = e^{s_1 t} k_1(t_1) - e^{s_2 t} k_2(t_1) \tag{3.32}$$

gives $y_p(t)$ as

$$y_p(t) = \int_t^{t_1} \frac{e^{-s_1(r-t)} - e^{-s_2(r-t)}}{l(s_2 - s_1)} \, f(r) \, dr + K(t, t_1) \tag{3.33}$$

which completes the proof ■

It is important to note that even if $s_1 = s_2$, in other words the system has a repeated roots, the particular solution can still be expressed as a wavelet transform. This can be easily proved using the particular solution of a system of 1st order differential equations. In the following we show that the SOULTI wavelet transform is the particular solution of Equation (3.18).

3.2.3 Particular solution of the reconstructing DE

Corollary 3.4. *Let $J \subset (a, \infty) \subset \mathbb{R}$, and let $f(t) : J \to \mathbb{R}$ be integrable and exponentially bounded, then there exists a and $0 < \zeta < 1$ such that the particular solution of Equation* (3.18) *is given by the SOULTI wavelet transform*

$$y_p(t) = \tilde{f}_\zeta(t, a) = \int_t^\infty \left(\frac{a^{-p}}{1 - \zeta^2} \right) e^{\frac{-\zeta}{\sqrt{1-\zeta^2}} \left(\frac{r-t}{a} \right)} \sin\left(\frac{r-t}{a} \right) \, f(r) \, dr \tag{3.34}$$

Proof: by comparing Equation (3.18) to Equation (3.22) we find that the parameters of the autonomous homogeneous differential equation in Equation (3.18) are given as follows

$$l = a^{p+1}(1 - \zeta^2) \tag{3.35}$$

$$h = -2a^p \zeta \sqrt{1 - \zeta^2} \tag{3.36}$$

$$g = a^{p-1} \tag{3.37}$$

We can use the result of Proposition 3.3 and substitute Equation (3.35) into Equation (3.33) and letting $t_1 \to \infty$ to have

$$y_p(t) = \int_t^\infty \frac{e^{\left(\frac{-\zeta}{a\sqrt{1-\zeta^2}} + i \right)(r-t)} - e^{\left(\frac{-\zeta}{a\sqrt{1-\zeta^2}} - i \right)(r-t)}}{-i2a^p(1 - \zeta^2)} \, f(r) \, dr - K(t, \infty) \tag{3.38}$$

Using Euler formula, Equation (3.38) reads

$$y_p(t) = \int_t^\infty \left(\frac{a^{-p}}{1 - \zeta^2} \right) e^{\frac{-\zeta}{\sqrt{1-\zeta^2}} \left(\frac{r-t}{a} \right)} \sin\left(\frac{r-t}{a} \right) \, f(r) \, dr - K(t, \infty) \tag{3.39}$$

Now, we have to show that $K(t,t_1)$ vanishes as $t_1 \to \infty$. Since $f(t)$ is of exponential order, then there exists m, a, $0 < \zeta < 1$, and $\alpha > 0$ all $\in \mathbb{R}$, such that $|f(t)| \leq |me^{\alpha t}| \leq |me^{\frac{\zeta}{a\sqrt{1-\zeta^2}}t}| \; \forall \; t \in J$. Therefore, $k_1(t)$ and $k_2(t)$ are bounded by the inequalities

$$|k_1(t)| \leq \left| \int \frac{m\, e^{(\frac{-\zeta}{a\sqrt{1-\zeta^2}}+i)t} e^{\alpha t}}{l\,(s_2-s_1)} dt \right| \quad \forall t \in J \tag{3.40}$$

$$|k_2(t)| \leq \left| \int \frac{m\, e^{(\frac{-\zeta}{a\sqrt{1-\zeta^2}}-i)t} e^{\alpha t}}{l\,(s_2-s_1)} dt \right| \quad \forall t \in J \tag{3.41}$$

after evaluating the integrals, they become

$$|k_1(t)| \leq \left| \frac{m\, e^{\left(\frac{-\zeta}{a\sqrt{1-\zeta^2}}+\alpha+i\right)t}}{l\,(s_2-s_1)((\frac{-\zeta}{a\sqrt{1-\zeta^2}}+\alpha+i))} \right| \quad \forall t \in J \tag{3.42}$$

$$|k_2(t)| \leq \left| \frac{m\, e^{\left(\frac{-\zeta}{a\sqrt{1-\zeta^2}}+\alpha-i\right)t}}{l\,(s_2-s_1)((\frac{-\zeta}{a\sqrt{1-\zeta^2}}+\alpha-i))} \right| \quad \forall t \in J \tag{3.43}$$

but as $t \to \infty$ both quantities on the left of inequalities 3.42 and 3.43 vanish. Therefore,

$$\lim_{t\to\infty} k_1(t) = \lim_{t\to\infty} k_2(t) = 0 \tag{3.44}$$

hence $K(t,\infty) = 0$ in Equation (3.39), and we obtain Equation (3.34) ■

3.3 SOULTI transform of elementary signals and its properties

Let us examine the validity of Equation (3.18) with an example.

Example 3.5. Let $f(t) = e^{(} - \beta t)$, then its SOULTI wavelet transform is given by

$$\tilde{f}_\zeta(\tau,a) = \int_{-\tau}^{\infty} e^{-\beta t} \frac{a^{-p}}{1-\zeta^2} e^{\frac{-\zeta}{\sqrt{1-\zeta^2}}(\frac{t-\tau}{a})} \sin(\frac{t-\tau}{a}) dt \tag{3.45}$$

which can be evaluated using the integration by parts technique to give

$$\tilde{f}_\zeta(\tau,a) = e^{-\beta\tau} \frac{a^{1-p}}{(1-\zeta^2)\beta a^2 + 2\sqrt{1-\zeta^2}\zeta\beta a + 1} \tag{3.46}$$

Which represents an analytical formula in terms of the scale a, the time shift τ, and the wavelet damping ratio ζ, in addition to the decay speed β.

Note that the transform of $e^{(} - \beta t)$ in Equation (3.46) consists of a multiplication of two functions, a function of time and a function of scale. Note also, that the transform is very similar to the Laplace Transform of a delayed and scaled function. Figure 3.4 shows the wavelet transform of the exponential function as described in Equation (3.46).

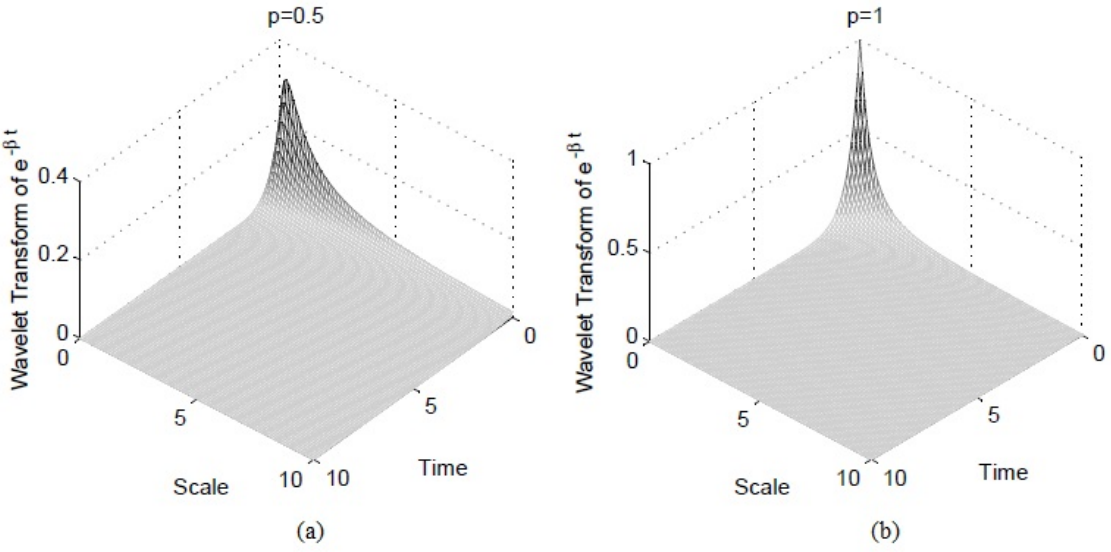

Figure 3.4: SOULTI Wavelet transform surface of the decaying exponential function at $\zeta = 0.7$ and $\beta = 2$.

Let us now evaluate the SOULTI inverse transform by using the formula in Equation (3.18). Differentiating Equation (3.46) with respect to time twice and substituting the result into the right hand side of Equation (3.46) and substituting τ for t yields

$$a^{p-1}\left[\left((1-\zeta^2)a^2\beta^2 e^{-\beta t} + e^{-\beta t} + 2\sqrt{1-\zeta^2}\zeta\beta a e^{-\beta t}\right)\left(\frac{a^{1-p}}{(1-\zeta^2)\beta a^2 + 2\sqrt{1-\zeta^2}\zeta\beta a + 1}\right)\right] = e^{-\beta t}\blacksquare \tag{3.47}$$

We can use the result in Equation (3.46) to find the SOULTI wavelet transform for the sinusoidal functions. Table 3.1 lists the SOULTI wavelet transform for some elementary signals. Figure 3.5 shows the wavelet transform scalogram of the $\cos(\omega t)$ function.

Table 3.1: SOULTI wavelet transform for basic signals.

#	$f(t)$	$\tilde{f}_\zeta(\tau, a)$
1	$u(t)$	a^{1-p}
2	$tu(t)$	$a^{1-p}\left(\frac{2\zeta a}{\sqrt{1-\zeta^2}} + \frac{1}{1-\zeta^2}\tau\right)$
3	$t^2u(t)$	$a^{1-p}\left(2(2\zeta^2-1)(1-\zeta^2)a^2 + 4\zeta\sqrt{1-\zeta^2}a\tau + (1-\zeta^2)\tau^2\right)$
4	$e^{-\beta t}$	$e^{-\beta\tau}\frac{a^{1-p}}{(1-\zeta^2)\beta a^2+2\sqrt{1-\zeta^2}\zeta\beta a+1}$
5	$\sin(\omega\tau)$	$\frac{a^{1-p}}{\sqrt{A^2+B^2}}\sin(\omega\tau+\phi)$ $\phi = \tan^{-1}\left(\frac{A}{B}\right)$ $A(a,\omega) = 1-(1-\zeta^2)a^2\omega^2$ $B(a,\omega) = 2\zeta\sqrt{1-\zeta^2}a\omega$
6	$\cos(\omega t)$	$\frac{a^(1-p)}{\sqrt{A^2+B^2}}\cos(\omega\tau+\phi)$ $\phi = \tan^{-1}\left(\frac{B}{A}\right)$ $A(a,\omega) = 1-(1-\zeta^2)a^2\omega^2$ $B(a,\omega) = 2\zeta\sqrt{1-\zeta^2}a\omega$
7	$e^{-\xi t}\cos(\omega t)$	$\frac{a^(1-p)}{\sqrt{A^2+B^2}}e^{-\xi\tau}\cos(\omega\tau+\phi)$ $\phi = \tan^{-1}\left(\frac{B}{A}\right)$ $A(a,\omega) = 1+(1-\zeta^2)(\xi^2-\omega^2)s^2 + 2\zeta\sqrt{1-\zeta^2}\xi a$ $B(a,\omega) = 2\left((1-\zeta^2)\xi\omega a^2 + \zeta^2\sqrt{1-\zeta^2}\omega a\right)$
8	$e^{-\xi t}\sin(\omega t)$	$\frac{a^(1-p)}{\sqrt{A^2+B^2}}e^{-\xi\tau}\sin(\omega\tau+\phi)$ $\phi = \tan^{-1}\left(\frac{B}{A}\right)$ $A(a,\omega) = 1+(1-\zeta^2)(\xi^2-\omega^2)a^2 + 2\zeta\sqrt{1-\zeta^2}\xi a$ $B(a,\omega) = 2\left((1-\zeta^2)\xi\omega a^2 + \zeta^2\sqrt{1-\zeta^2}\omega a\right)$

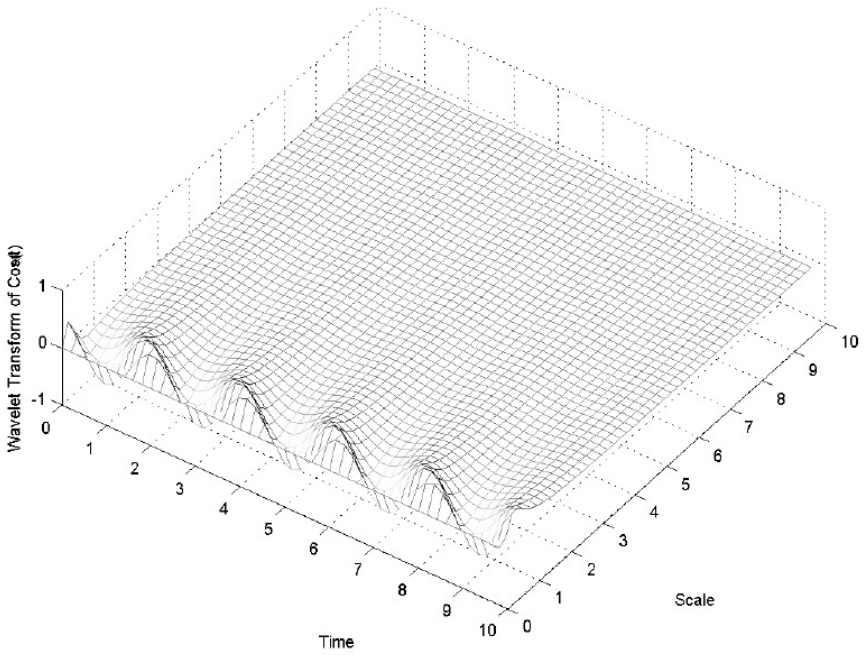

Figure 3.5: SOULTI wavelet transform of $f(t) = \cos(\omega t)$, at $\zeta = 0.7$.

3.3.1 SOULTI transform of derivatives

Lemma 3.6. *Let J be as defined in Section 3.1.1, and let $x(t) : J \to \mathbb{R}$ be differentiable and exponentially bounded, see Section 3.1.1, and the SOULTI wavelet transform of $x(t)$ be given by Equation* (3.8)*, then the SOULTI wavelet transform of $\dot{x}(t)$ is given by*

$$\begin{aligned} \tilde{\dot{x}}_\zeta(\tau, a) &= \frac{e^{\frac{-\zeta}{\sqrt{1-\zeta^2}}\theta}}{a\sqrt{1-\zeta^2}} \tilde{x}_\zeta(\tau + a\theta, a) \\ \theta &= \tan^{-1}\left(\frac{\sqrt{1-\zeta^2}}{\zeta}\right) \end{aligned} \tag{3.48}$$

Proof: substitute $\dot{x}(t)$ in Equation (3.8) to have

$$\tilde{\dot{x}}_\zeta(\tau, a) = \int_\tau^\infty \dot{x}(t)\psi_\zeta(\frac{t-\tau}{a})dt, \quad , \tau \in (-\infty, \infty) \tag{3.49}$$

which can be evaluated by the integration by parts technique to obtain

$$\begin{aligned} \tilde{\dot{x}}_\zeta(\tau, a) =& \frac{a^{-p}}{1-\zeta^2}\left(x(t)e^{\frac{-\zeta}{\sqrt{1-\zeta^2}}\left(\frac{t-\tau}{a}\right)}\sin\left(\frac{t-\tau}{a}\right)\Big|_\tau^\infty\right) \\ & - \frac{s^{-p}}{1-\zeta^2}\left(\int_\tau^\infty \frac{x(t)}{a\sqrt{1-\zeta^2}} e^{\frac{-\zeta}{\sqrt{1-\zeta^2}}\left(\frac{t-\tau}{a}\right)}\sin\left(\theta - \frac{t-\tau}{a}\right)dt\right) \end{aligned} \tag{3.50}$$

where θ is given by

$$\theta = \tan^{-1}\left(\frac{\sqrt{1-\zeta^2}}{\zeta}\right) \tag{3.51}$$

Since $x(t)$ is exponentially bounded, then the first term in Equation (3.50) vanishes, so Equation (3.50) becomes

$$\tilde{\dot{x}}_\zeta(\tau,a) = \frac{e^{\frac{-\zeta}{\sqrt{1-\zeta^2}}\theta}}{a\sqrt{1-\zeta^2}}\left(\frac{a^{-p}}{1-\zeta^2}\int_\tau^\infty x(t)e^{\frac{-\zeta}{\sqrt{1-\zeta^2}}\left(\frac{t-(\tau+a\theta)}{a}\right)}\sin\left(\frac{t-(\tau+a\theta)}{a}\right)dt\right) \tag{3.52}$$

but the part inside the parenthesis is equal to $\tilde{x}_\zeta(\tau+a\theta,a)$, hence Equation (3.52) is equivalent to Equation (3.48) ■

3.3.2 SOULTI transform of integrals

Lemma 3.7. *Let J be as defined in Section 3.1.1, and let $x(t) : J \to \mathbb{R}$ be exponentially bounded as defined in Section 3.1.1, and the SOULTI wavelet transform of $x(t)$ be given by Equation* (3.8)*, then the SOULTI wavelet transform of $\chi(t)$, defined by*

$$\chi(t) = X(t) - X(\eta) = \int_\eta^t x(r)dr \tag{3.53}$$

is given by

$$\begin{aligned}&\tilde{\chi}_\zeta(\tau,a) = a\sqrt{1-\zeta^2}e^{\frac{\zeta}{\sqrt{1-\zeta^2}}\theta}\tilde{x}_\zeta(\tau-a\theta,a) - a^{1-p}X(a)\\ &\theta = \tan^{-1}\left(\frac{\sqrt{1-\zeta^2}}{\zeta}\right)\end{aligned} \tag{3.54}$$

Proof: since $x(t) = \frac{dX(t)}{dt}$, substitute $x(t)$ in place of $\dot{x(t)}$, and $X(t)$ in place of $x(t)$ in Equation (3.52), and the result can be written as

$$\int_\tau^\infty x(t)\psi_\zeta(\frac{t-\tau}{a})dt = \frac{e^{\frac{-\zeta}{\sqrt{1-\zeta^2}}\theta}}{a\sqrt{1-\zeta^2}}\left(\int_\tau^\infty X(t)\psi_\zeta\left(\frac{t-(\tau+a\theta)}{a}\right)dt\right) \tag{3.55}$$

make the substitutions $\chi(t) + X(a) = X(t)$, and $\sigma = \tau + a\theta$ into Equation (3.55), then Equation (3.54) follows.

3.4 The time-frequency resolution and properties

The time-frequency resolution is an important property of the wavelet transform. The resolution is defined by

$$\mu = \Delta T.\Delta\Omega \tag{3.56}$$

where ΔT is the time resolution or the time window, and, $\Delta\Omega$ is the frequency resolution or frequency window. The time window represents the time interval that a frequency can be identified within, while $\Delta\Omega$ represents the range of frequencies within a time interval. There are different ways to define the time and frequency resolutions. One possible way is to use the standard deviation definition, in which the resolutions are defined by

$$\Delta T_{SD}^2 = \frac{\int_{-\infty}^{\infty}(t - t_{CG\zeta})^2|\psi_\zeta(t)|^2dt}{\int_{-\infty}^{\infty}|\psi_\zeta(t)|^2dt} \tag{3.57}$$

$$\Delta\Omega_{SD}^2 = \frac{\int_{-\infty}^{\infty}(\omega - \omega_{CG\zeta})^2|\Psi_\zeta(\omega)|^2d\omega}{\int_{-\infty}^{\infty}|\Psi_\zeta(\omega)|^2d\omega} \tag{3.58}$$

where $t_{CG\zeta}$ and $\omega_{CG\zeta}$ represent the center of mass of the signal in time and frequency respectively, and they are given by

$$t_{CG\zeta} = \frac{\int_0^{\infty} t|\psi_\zeta(t)|^2dt}{\int_0^{\infty}|\psi_\zeta(t)|^2dt} \tag{3.59}$$

$$\Delta\Omega_{SD}^2 = \frac{\int_0^{\infty}\omega|\Psi_\zeta(\omega)|^2d\omega}{\int_0^{\infty}|\Psi_\zeta(\omega)|^2d\omega} \tag{3.60}$$

Table 3.2 lists the results of calculating μ for some values of $0 < \zeta < 1$ at $p = 1$. The values of μ does not depend on the scale value and they satisfy the Heisenberg principle (Kaiser, 2010), where $\mu > \pi/4$. However $\omega_{CG\zeta}$ is proportional to the scale s, while $t_{CG\zeta}$ is inversely proportional to a. However, the standard deviation does not offer meaningful time and frequency windows of resolution. The SOULTI wavelet is not symmetrical neither in time nor in frequency. Moreover, it has no compact support in time. So we would question the significance of the standard deviation window about the signal center in time, and the significance of the frequencies included in the standard deviation window and weather that is really what is accentuated in the time-scale or time-frequency analysis.

We can attain an alternative definition for the SOULTI wavelet resolution based on systems dynamics and control theory. The system response is considered settled when it enters the 2 margin of the final value and never leaves it again. Therefore, we can use the 2% settling time value to define the time window as $\Delta T_{2\%} = 2\%t_{st}$.

In the frequency domain, the frequency corresponding to attenuating the input power by a half is considered the frequency bandwidth of the system or the cut-off frequency, so we can use the bandwidth to define the frequency window.

Table 3.2: Time-Frequency resolution based on standard deviation definition at $p = 1$.

ζ	$t_{CG\zeta}$	$\omega_{CG\zeta}$	ΔT_{SD}	$\Delta\Omega_{SD}$	μ
0.05	20.075	0.48531	39.85	0.24577	9.794
0.1	10.149	0.47298	19.704	0.33949	6.689
0.15	6.8878	0.46292	12.896	0.40724	5.252
0.2	5.2909	0.45506	9.4305	0.46191	4.356
0.25	4.3571	0.44939	7.3101	0.5088	3.719
0.3	3.7522	0.44595	5.8715	0.55084	3.234
0.35	3.3322	0.44484	4.8325	0.58997	2.851
0.4	3.0245	0.44625	4.0534	0.62763	2.544
0.45	2.7882	0.45046	3.4579	0.66502	3
0.5	2.5981	0.4579	3	0.7033	2.11
0.55	2.4372	0.46922	2.6493	0.74366	1.970
0.6	2.2933	0.48537	2.3828	0.78752	1.877
0.65	2.157	0.50783	2.1798	0.83668	1.824
0.7	2.02	0.53899	2.0203	0.89372	1.806
0.75	1.8741	0.58291	1.8838	0.96259	1.813
0.8	1.71	0.64715	1.7483	1.05	1.836
0.85	1.5153	0.74778	1.5888	1.1692	1.858
0.9	1.2689	0.927	1.3714	1.3512	1.853
0.95	0.92196	1.3553	1.0296	1.7057	1.756

The 2% settling time, t_{st} is guaranteed to occur when the enveloping function enters within 2% of the final value. Therefor, for a scaled wavelet, it is given by

$$t_{st} = -\frac{s\sqrt{1-\zeta^2}}{\zeta}\log(0.02) \simeq \frac{4s\sqrt{1-\zeta^2}}{\zeta} \tag{3.61}$$

On the other hand, the wavelet bandwidth is the frequency at which the frequency spectrum of a scaled wavelet satisfies

$$|a\Psi(a\omega)|^2 = \frac{\frac{a^{2-2p}}{1-\zeta^2}}{\left(-a^2\omega^2 + \frac{1}{1-\zeta^2}\right)^2 + \left(\frac{2\zeta\omega a}{\sqrt{1-\zeta^2}}\right)^2} = \frac{1}{2} \tag{3.62}$$

Solving for ω gives the bandwidth by

$$\omega\Big|_{|a\Psi(a\omega)|^2=\frac{1}{2}} = \Delta\Omega_{BW} = \frac{1}{a\sqrt{1-\zeta^2}}\sqrt{1-2\zeta^2+\sqrt{2a^{2-2p}-4\zeta^2+4\zeta^4}} \tag{3.63}$$

Substitute Equation (3.61) and Equation (3.63) into Equation (3.56) gives the resolution as

$$\mu = 4\frac{\sqrt{1-2\zeta^2+\sqrt{2a^{2-2p}-4\zeta^2+4\zeta^4}}}{\zeta} \tag{3.64}$$

Equation (3.64) gives us a way to determine an appropriate value for p based on the time-frequency resolution shape. In order for μ to be independent of a, we must have $p = 1$, which yields

$$\mu(\zeta) = 4\frac{\sqrt{1-2\zeta^2+\sqrt{2-4\zeta^2+4\zeta^4}}}{\zeta} \tag{3.65}$$

which indicates that the $2\%t_{st} - \Delta\Omega_{BW}$ resolution definition depends only on ζ thus on the wavelet family ψ_ζ, so we may write $\mu(\zeta)$ as $\mu(\psi_\zeta)$. Now, let us investigate the values of mu in ζ range, $0 < \zeta < 1$. When $\zeta \to 0$, we have

$$\lim_{\zeta\to 0}\mu(\zeta) = \infty \tag{3.66}$$

while when $\zeta \to 1$ we get

$$\lim_{\zeta\to 1}\mu(\zeta) = 2.65 \tag{3.67}$$

Since $\frac{d\mu}{d\zeta} < 0 \forall \zeta \in (0,1)$, then

$$\frac{\pi}{4} < 2.65 < \mu(\zeta) < \infty \tag{3.68}$$

which means that the $2\%t_{st} - \Delta\Omega_{BW}$ definition satisfies the Heisenberg principle when $p = 1$. Another advantage of having $p = 1$, is preserving the wavelet frequency function peak

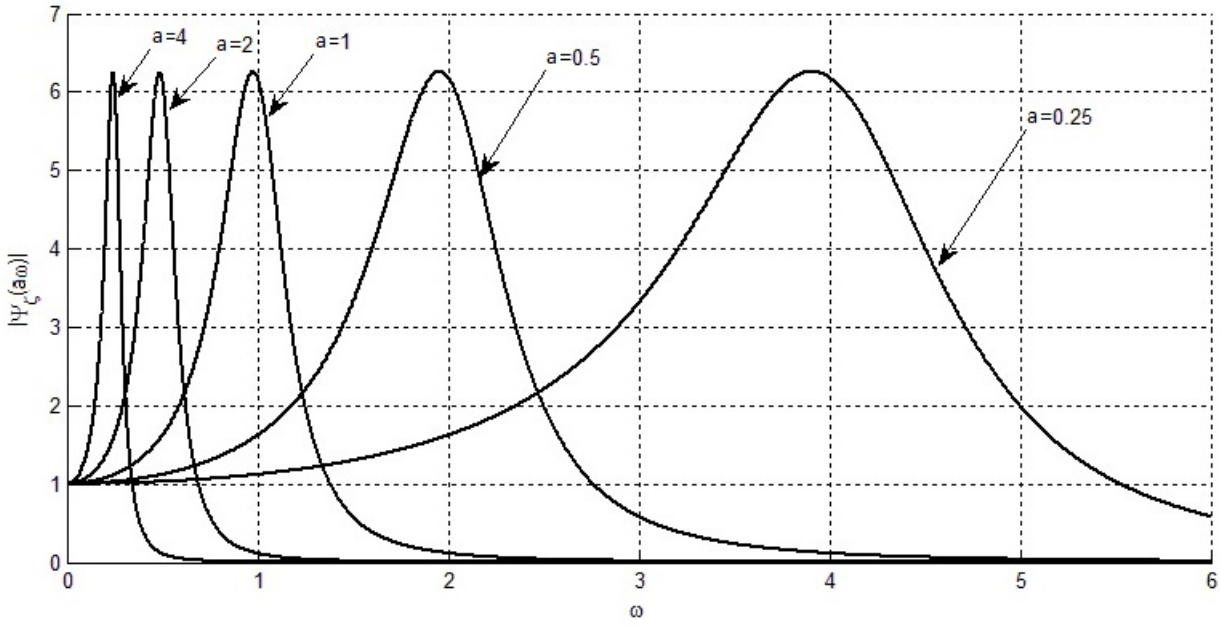

Figure 3.6: Wavelet amplitude in frequency domain for different values of scaling at $\zeta = 0.2$

constant. This is sometimes useful since it guarantees that all the frequency bands are amplified at the same level, see Figure 3.6. This works as a normalizing factor though it does not preserve the wavelet energy. Figure 3.2 shows the standard deviation-based and the $2\%t_{st}$-based time windows, while Figure 3.3 illustrates the standard deviation-based and the half-power bandwidth-based frequency windows for the SOULTI wavelet.

The $2\%t_{st} - \Delta\Omega_{BW}$ gives a better meaning for the time-frequency resolution of the SOULTI wavelet, but when ζ is small, $\zeta < 0.4$, the definition suffers from two problems. First, the variation in the frequency response magnitude varies significantly within the bandwidth, which requires better focus on the resonance range. Secondly, as a decreases, the bandwidth of $\psi(\frac{t}{a})$ contains all the bandwidths corresponding to larger a values, i.e. $\Delta\Omega_{BW}(\zeta, a_2) \subset \Delta\Omega_{BW}(\zeta, a_1)$ when $a_1 < a_2$.

For $\zeta < 0.4$, another definition of the time-frequency, resolution that better reflects the data on the time-scale or the time-frequency analysis domain is based on the quality factor half-power bandwidth. The quality factor is the peak value of the frequency response of the second order system. For small ζ, the quality factor for LTI second order system can be approximated by [90]

$$Q = \frac{1}{2\zeta} \tag{3.69}$$

The half power points, q_1 and q_2 are the points when $|\Psi(a\omega)| = \frac{Q}{\sqrt{2}}$, see Figure 3.7. The bandwidth of the frequency response is

$$\Delta\Omega_Q = \omega_2 - \omega_1 \tag{3.70}$$

where ω_1, ω_2 is the corresponding frequency to q_1, q_2 respectively, as shown in Figure 3.7. To find ω_1 and ω_2 we have to solve the wavelet power in Equation (3.71) for ω where $p = 1$.

$$|\Psi(a\omega)|^2 = \frac{1}{(-a^2\omega^2(1-\zeta^2))^2 + \left(2\zeta\omega\sqrt{1-\zeta^2}a\right)^2} = \frac{1}{8\zeta^2} \tag{3.71}$$

From Equation (3.71) we find

$$\omega_1^2 = \frac{1-2\zeta}{a^2(1-\zeta^2)} \tag{3.72}$$

$$\omega_2^2 = \frac{1+2\zeta}{a^2(1-\zeta^2)} \tag{3.73}$$

Using the approximation ($\omega_1 + \omega_2 \simeq \frac{2}{a\sqrt{1-\zeta^2}}$), which is valid for small values of ζ, it is easy to show that

$$\Delta\Omega_Q = \omega_2 - \omega_1 = \frac{2\zeta}{a\sqrt{1-\zeta^2}} \tag{3.74}$$

Substituting Equations (3.61) and (3.74) into Equation (3.56), the new time-frequency resolution definition becomes

$$\mu = \Delta T \Delta\Omega \simeq \frac{4a\sqrt{1-\zeta^2}}{\zeta}\frac{2\zeta}{a\sqrt{1-\zeta^2}} = 8 \tag{3.75}$$

Equation (3.75) shows a very interesting result where the time-frequency resolution is constant and does not depend on ζ. Note that this approximation is valid for values of $\zeta < 0.4$, for larger values the quality factor is smaller, hence the time-frequency resolution defined by Equations (3.64) and (3.65) would be more meaningful and suitable to adopt. Of course one may require a wider bandwidth than the half-power quality factor bandwidth, which will make the time-frequency resolution coarser. For example, if instead of the $\frac{Q}{\sqrt{2}}$ bandwidth limit we use Q/x, where $x < Q$, then the bandwidth and the time-frequency resolution become

$$\Delta\Omega_Q = \simeq \frac{2\sqrt{x^2-1}\zeta}{a\sqrt{1-\zeta^2}} \tag{3.76}$$

$$\mu = 8\sqrt{x^2-1} \tag{3.77}$$

The frequency at Q represents the frequency at which the wavelet filter is centered at. Moreover, it is easy to predict where the wavelet frequency is centered because the scale is directly linked to frequency as stated by Equation (3.5). The peak occurs at [90]

$$\omega_Q = \omega_n\sqrt{1-2\zeta^2} \tag{3.78}$$

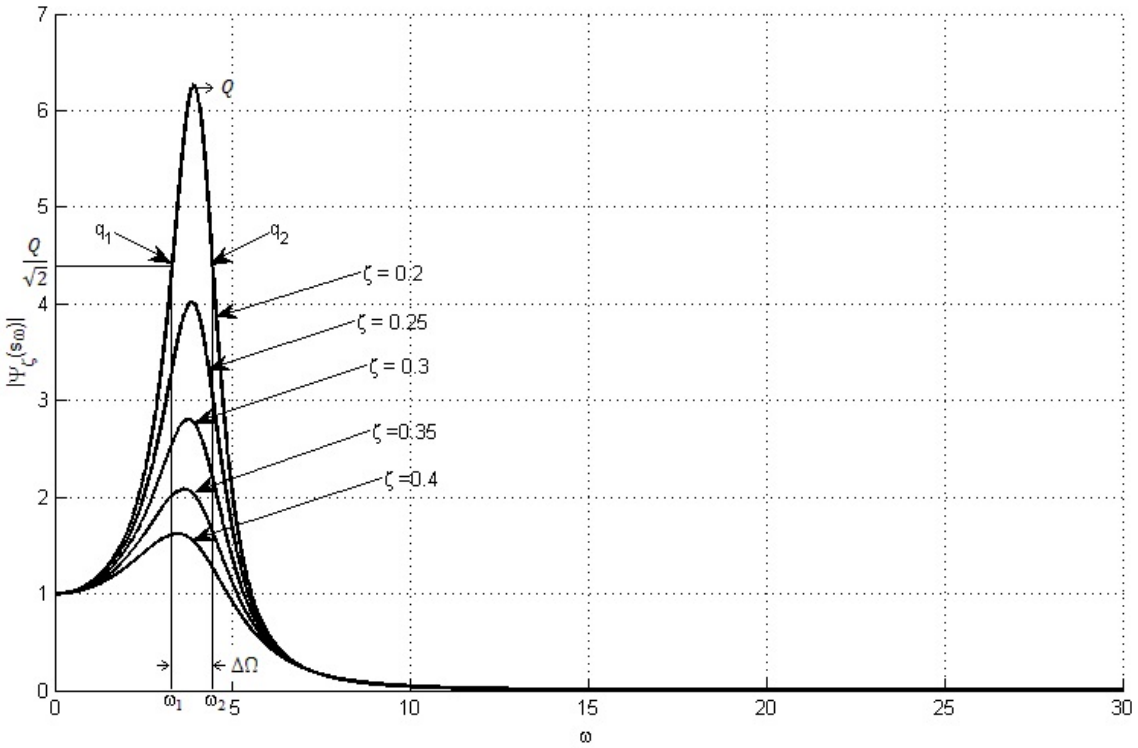

Figure 3.7: $|\Psi(a\omega)|$ for different values of ζ showing the quality factor and the half-power bandwidth.

For small ζ we have,

$$\omega_Q = \omega_n\sqrt{1-2\zeta^2} \simeq \omega_n\sqrt{1-\zeta^2} = \omega_d \tag{3.79}$$

which with Equation (3.5) shows that we can easily approximate to good accuracy the wavelet peak frequency by the relation

$$\omega_Q \simeq \frac{1}{a} \tag{3.80}$$

Figure 3.6 shows clearly the accuracy of Equation (3.80) for the $\psi_0.2(\frac{t}{a})$ SOULTI family with different scaling values. For larger values of ζ, i.e. $\zeta >= 0.4$, the approximation in Equation (3.80) is not valid and we have to use the exact relation

$$\omega_Q = \frac{\sqrt{1-2\zeta^2}}{\sqrt{1-\zeta^2}}\frac{1}{a} \tag{3.81}$$

The SOULTI wavelet has $\Psi(0) = 1$ when $p = 1$. For other values of p, the wavelet magnitude depends on a^{1-p}. Moreover, we have

$$\int_0^\infty \frac{|\Psi(\omega)_\zeta|^2}{\omega} d\omega = \infty \tag{3.82}$$

which implies that the SOULTI wavelet does not satisfy the admissibility condition stated in Equation (2.7) but it has and inverse, hence the admissibility condition is not necessary.

Chapter 4

Generalized Complex SOULTI Wavelets (Laplace Wavelets)

Parts of the content of this chapter are extracted from a study, by the author of this dissertation, that is published in the Journal of Vibration and Control [2].

Having the definition, properties, and inverse of the SOULTI wavelet laid out, we can generalized the SOULTI wavelet to the complex domain and define a complex version of the wavelet. The resulting complex wavelet is similar to the Laplace transform kernel function, and the Laplace Wavelet Trasform (LWT) is similar to the wavelet transform and can be derived from it. The generalization to the complex domain adds many advantages as will be shown in this chapter. For example, the Laplace wavelet frequency filter is exactly centered at the reciprocal of the scale. Moreover, the edge effect is mitigated by the use of the Laplace wavelet.

In the following sections, the properties and theory of the Laplace wavelet is defined in a parallel sequence to the sequence followed in Chapter 3.

4.1 The Laplace Wavelet Transform

$$\psi_{L\zeta}^{s,\tau}(t) = \left(\frac{s^{-p}}{1-\zeta^2}\right) e^{\frac{-\zeta}{\sqrt{1-\zeta^2}}\left(\frac{t-\tau}{s}\right)} \left(\cos\left(\frac{t-\tau}{s}\right) + j\sin\left(\frac{t-\tau}{s}\right)\right) u(t-\tau) \tag{4.1}$$

which can be written in the form

$$\psi_{L\zeta}^{s,\tau}(t) = \left(\frac{s^{-p}}{1-\zeta^2}\right) e^{\left(\frac{-\zeta}{\sqrt{1-\zeta^2}}+j\right)\left(\frac{t-\tau}{s}\right)} u(t-\tau) \tag{4.2}$$

Then, the complex SOULTI transform is given by

$$\tilde{f}_{C\zeta}(\tau, s) = \left(\frac{s^{-p}}{1-\zeta^2}\right) \int_{\tau}^{\infty} f(t) e^{\left(\frac{-\zeta}{\sqrt{1-\zeta^2}}+j\right)\left(\frac{t-\tau}{s}\right)} dt \tag{4.3}$$

which is similar to the Laplace transform but with time delay and is restricted to the left half of the complex domain excluding the real and the imaginary axes. In addition, the integral is restricted to the interval $t \in [\tau, \infty)$. However, it is natural that the new wavelet and it's transform inherit many properties from the Laplace transform.

The new transform generates a phase output because it outputs real and imaginary parts. Moreover, the SOULTI wavelet represents the imaginary part of the transform. Figure 4.1 shows a plot of the Laplace wavelet.

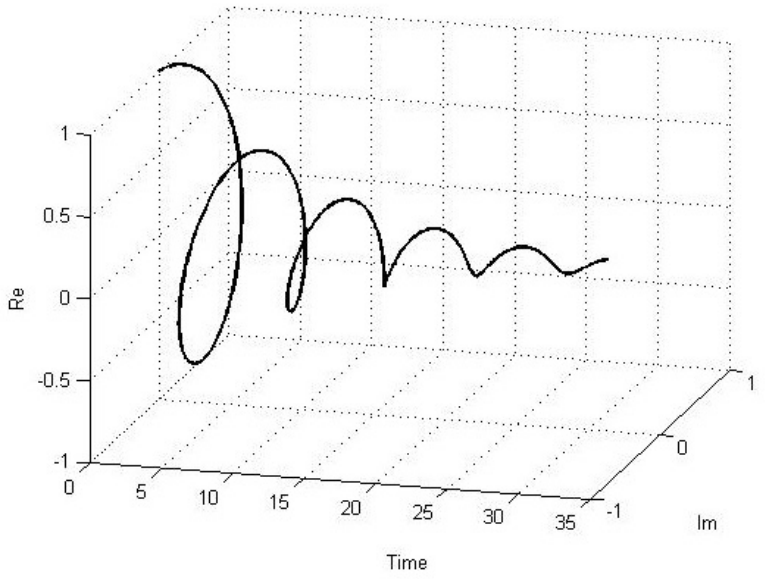

Figure 4.1: The Laplace wavelet

4.1.1 The Laplace transform and the Laplace wavelet transform

Suppose that $J \subset (a, \infty) \subset \mathbb{R}$, and let $f(t) : J \to \mathbb{R}$, where $f(t) \in L^1$ and is exponentially bounded, see Definition 3.1, then using the definition of the Laplace Wavelet in Equation (4.2), the LWT of $f(t)$ reads

$$\mathcal{W}_{L_\zeta}\{f(t)\} = \tilde{f}_{L_\zeta}(\tau, a) = \left(\frac{a^{-p}}{1-\zeta^2}\right) \int_{\tau}^{\infty} e^{\left(\frac{-\zeta}{\sqrt{1-\zeta^2}}+j\right)\left(\frac{t-\tau}{a}\right)} f(t) dt \tag{4.4}$$

Now, we can establish a relation between the Laplace transform and the LWT. The Laplace transform is defined as

$$\mathcal{L}\{f(t)\} = F(s) = \int_{-\infty}^{\infty} e^{-st} f(t) dt \tag{4.5}$$

which can be written for right sided signals, namely $f(t) = 0$ if $t < 0$, as

$$F(s) = \int_0^\infty e^{-st} f(t) dt \tag{4.6}$$

where $s \in \mathbb{C}$ is the Laplace complex variable. Now, consider the exponent part in Equation (4.4) and make the substitutions

$$\sigma = \frac{1}{a}\left(\frac{\zeta}{\sqrt{1-\zeta^2}} - j\right) \tag{4.7}$$

$$c = \left(\frac{1}{1-\zeta^2}\right) \tag{4.8}$$

then substitute Equations (4.7) and (4.8) back into Equation (4.4) to arrive at

$$\tilde{f}_{L_\zeta}(\tau, \sigma) = ca^{-p} \int_\tau^\infty e^{-\sigma(t-\tau)} f(t) dt \tag{4.9}$$

Because $u(t-\tau) = 0,\ t \leq \tau$, the integration lower limit changed to start from τ, and the Heaviside function is dropped from the integration. By comparing Equations (4.6) and (4.9), we find that the Laplace wavelet transform is similar to the Laplace transform with positive time-delay, namely $\mathcal{L}\{f(t+\tau)\}$, but the lower limit of the integration is different. However, the time-shifting property of the Laplace transform does not apply here, because the Laplace wavelet, which is the transform kernel, is right-sided. When the kernel is right-sided and a positive shift is applied to the transformed signal, part of the signal becomes multiplied by zero and does not count for the integration. In this case, the Laplace time-shifting property is only applicable when the shift is negative.

Alternatively, the Laplace wavelet transform in Equation (4.9), can be written as

$$\tilde{f}_{L_\zeta}(\tau, \sigma) = ca^{-p} e^{\sigma\tau} \int_\tau^\infty e^{-\sigma t} f(t) dt \tag{4.10}$$

which can be split into two parts as

$$\tilde{f}_{L_\zeta}(\tau, \sigma) = ca^{-p} e^{\sigma\tau} \left(\int_0^\infty e^{-\sigma t} f(t) dt - \int_0^\tau e^{-\sigma t} f(t) dt\right) \tag{4.11}$$

where the first term inside the parenthesis is the Laplace transform of $f(t)$, so Equation (4.11) can be written as

$$\mathcal{W}_{L_\zeta}\{f(t)\} = ca^{-p} e^{\sigma\tau} \left(\mathcal{L}\{f(t)\}\big|_{s=\sigma} - \int_0^\tau e^{-\sigma t} f(t) dt\right) \tag{4.12}$$

Equation (4.12) shows the relation between the Laplace transform and the LWT. It is important to notice that with the LWT not all the complex Laplace domain is covered. The transform is only restricted to the region in the complex domain determined by Equation (4.7).

Figure 4.2 shows the relationship between the Laplace domain and the Time-Scale domain of the LWT. The Time-Scale domain intersects perpendicularly the Laplace domain, where the time axis is perpendicular to the Laplace complex plane. Each ray that emerges from the origin in the left half plane represents a Laplace wavelet family. Each wavelet family is determined by the parameter ζ, which is restricted to the range $0 < \zeta < 1$. The parameter ζ controls the angle between the scale axis and the real axis of the Laplace domain, where the angle is given by

$$\phi(\zeta) = \tan^{-1}\left(\frac{\zeta}{\sqrt{1-\zeta^2}}\right) = \cos^{-1}(\zeta) \tag{4.13}$$

Also, note that the permissible range of σ on the Laplace domain includes the left half-plane except the real and imaginary axes.

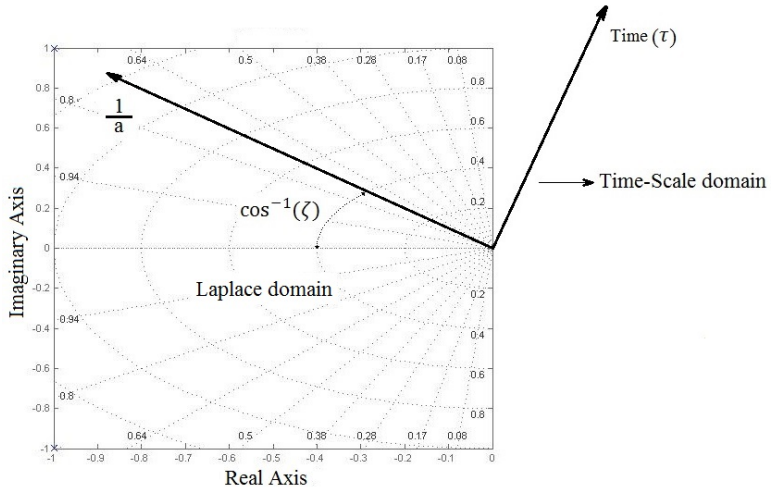

Figure 4.2: The Laplace domain and the time-scale domain.

The transform in Equation (4.4) can be evaluated either by direct substitution of the signal into the integral or by evaluating the real and imaginary parts separately and then combining the two together. Also, we can use the similarity between the Laplace transform and the Laplace wavelet transform to evaluate the LWT.

The Morse wavelet approaches the complex exponential as $\beta \to \infty$ for a fixed value of γ [79]. So the Laplace wavelet can be considered a special case of the Morse wavelets that falls on the Morse wavelet boundary.

4.2 Inverse Laplace wavelet transform

Evaluating the Inverse Laplace Wavelet Transform (ILWT) is similar to evaluating the inverse SOULTI wavelet transform, and deriving the inverse formula is parallel to deriving the inverse

formula of the SOULTI wavelet transform. Moreover, for simple signals, the real part of the Laplace wavelet transform can be used directly to evaluate the ILWT by applying the Inverse SOULTI wavelet transform to the imaginary part of the LWT.

The Fourier transform of the Laplace mother wavelet is given by

$$\mathcal{F}\left\{\psi_{L_\zeta}(t)\right\} = \mathcal{F}\left\{\frac{a^{-p}}{1-\zeta^2} e^{\left(\frac{-\zeta}{\sqrt{1-\zeta^2}}+j\right)t}\right\} = \frac{a^{-p}}{j(1-\zeta^2)(\omega-1)+\zeta\sqrt{1-\zeta^2}} \tag{4.14}$$

For a shifted and scaled version of the wavelet, the Fourier transform is given by

$$\mathcal{F}\left\{\psi_{L_\zeta}(\frac{t-\tau}{a})\right\} = ae^{-j\omega\tau}\Psi_{L_\zeta}(a\omega) = e^{-j\omega\tau}\frac{a^{1-p}}{j(1-\zeta^2)(a\omega-1)+\zeta\sqrt{1-\zeta^2}} \tag{4.15}$$

since $a > 0$, then $\Psi_{L_\zeta}(a\omega)$ never vanishes. Using the Plancherel's Identity [144], the Fourier transform of $f(t)$ becomes

$$\tilde{f}_{L_\zeta}(\tau, a) = \frac{a}{2\pi}\int_{-\infty}^{\infty} e^{j\omega\tau}\overline{\Psi_{L_\zeta}(a\omega)}F(\omega)d\omega \tag{4.16}$$

Equation (4.16) is equal to the inverse Fourier transform of $a\overline{\Psi_{L_\zeta}(a\omega)}F(\omega)$, where $\overline{\Psi_{L_\zeta}(a\omega)}$ is the complex conjugate of $\Psi_{L_\zeta}(a\omega)$. By applying the Fourier transform to both sides of Equation (4.16), we arrive at

$$\int_{-\infty}^{\infty} e^{-j\omega\tau}\tilde{f}_{L_\zeta}(\tau, a)d\tau = a\overline{\Psi_{L_\zeta}(a\omega)}F(\omega) \tag{4.17}$$

Dividing by $\overline{\Psi_{L_\zeta}(a\omega)}$ is a legitimate operation since it does not vanish for any value of ω or a. When Equation (4.17) is solved for $F(\omega)$, we obtain

$$F(\omega) = \frac{1}{a\overline{\Psi_{L_\zeta}(a\omega)}}\int_{-\infty}^{\infty} e^{-j\omega\tau}\tilde{f}_{L_\zeta}(\tau, a)d\tau \tag{4.18}$$

Applying the inverse Fourier transform to both sides of Equation (4.18) retrieves $f(t)$ back in the form

$$f(t) = \frac{1}{2\pi}\int_{-\infty}^{\infty}\int_{-\infty}^{\infty}\frac{1}{a\overline{\Psi_{L_\zeta}(a\omega)}}e^{-j\omega(\tau-t)}\tilde{f}_{L_\zeta}(\tau, a)d\tau d\omega \tag{4.19}$$

Equation (4.19) represents an integral formula for the ILWT. In the following, we show that other formulas are possible if $f(t)$ satisfies certain conditions. Now, some theorems and corollaries can be introduced in an analogous approach to the SOULTI wavelet theorems.

4.2.1 Inverse Laplace wavelet transform

Theorem 4.1. *Let $J \subset (\alpha, \infty) \subset \mathbb{R}$, and let $f(t) : J \to \mathbb{R}$ be integrable and exponentially bounded, and let the Laplace wavelet transform of $f(t)$ be given by Equation (4.4), then $f(t)$ can be retrieved back from its wavelet transform $\tilde{f}_{L_\zeta}(t,a)$, using the identity*

$$f(t) = a^{p-1}\left(-(1-\zeta^2)a\frac{d\left(\tilde{f}_{L_\zeta}(t,a)\right)}{dt} + \left(j(1-\zeta^2)+\zeta\sqrt{1-\zeta^2}\right)\tilde{f}_{L_\zeta}(t,a)\right) \tag{4.20}$$

Proof: Substituting $a\overline{\Psi_\zeta(a\omega)}$ from Equation (4.15) into Equation (4.19) gives

$$f(t) = \int_{-\infty}^{\infty}\frac{e^{j\omega t}}{2\pi a^{1-p}}\left(j\left(1-\zeta^2\right)(1-\omega)+\zeta\sqrt{1-\zeta^2}\right)\int_{-\infty}^{\infty}e^{-j\omega t}\tilde{f}_{L_\zeta}(t,a)dtd\omega \tag{4.21}$$

Using the operator notation for the Fourier transform, Equation (4.21) becomes

$$f(t) = a^{p-1}\mathcal{F}^{-1}\left\{\left(-j\left(1-\zeta^2\right)\omega + j\left(1-\zeta^2\right)+\zeta\sqrt{1-\zeta^2}\right)\mathcal{F}\left\{\tilde{f}_{L_\zeta}(t,a)\right\}\right\} \tag{4.22}$$

Applying the linear operators properties [95] to Equation (4.22) gives

$$\begin{aligned} f(t) = {} & a^{p-1}\mathcal{F}^{-1}\left\{-j\left(1-\zeta^2\right)\omega\mathcal{F}\left\{\tilde{f}_{L_\zeta}(t,a)\right\}\right\} \\ & + a^{p-1}\mathcal{F}^{-1}\left\{\left(j\left(1-\zeta^2\right)+\zeta\sqrt{1-\zeta^2}\right)\mathcal{F}\left\{\tilde{f}_{L_\zeta}(t,a)\right\}\right\} \end{aligned} \tag{4.23}$$

and after applying the Fourier transform differentiation property to Equation (4.23) we arrive at Equation (4.20) ■

This result parallels a similar result for the SOULTI wavelet as proved in Section 3.2. However, the requirement on $\tilde{f}_{L_\zeta}(\tau,a)$ is to be differentiable, which is satisfied if $f(t)$ is integrable and exponentially bounded.

Theorem 4.1 proves that $\tilde{f}_\zeta$ is a solution of Equation (4.20). However, by observing Table 4.1 we find that the solution given by the wavelet transform is the particular solution. By plugging each of the basic functions in Table 4.1 in Equation (4.20) and solving for the particular solution using the method of undetermined coefficients, one can prove that the LWT gives the particular solution for that specific function.

In the following, we provide a proof showing that the LWT gives the particular solution of first order linear autonomous differential equations with positive characteristic equation root. In other words, the particular solution given by the variation of parameters method is a wavelet transform.

4.2.2 particular solution by Laplace wavelet transform

Theorem 4.2. *Let $J \subset (a, \infty) \subset \mathbb{R}$, and let $f(t) : J \to \mathbb{R}$ be integrable, and let $t_1 \in J$, then the particular solution of the non-homogeneous linear differential equation*

$$f(t) = \kappa \frac{dy(t)}{dt} + \gamma y(t) \tag{4.24}$$

is given by

$$y_p(t) = -\frac{1}{\kappa} \int_t^{t_1} e^{\frac{\gamma}{\kappa}(r-t)} f(r) dr + e^{-\frac{\gamma}{\kappa}t} H(t_1) \tag{4.25}$$

where

$$H(t) = \int e^{\frac{\gamma}{\kappa}t} f(t) dt \tag{4.26}$$

Moreover, if $f(t)$ is exponentially bounded, such that $|f(t)| \leq |k.e^{\alpha t}| < |k.e^{|\frac{\gamma}{\kappa}|t}| \; \forall t \in J$, and if $\frac{\gamma}{\kappa} < 0$, then as $t_1 \to \infty$, $H(t_1) \to 0$ and the particular solution of Equation (4.24) is given by

$$y_p(t) = -\frac{1}{\kappa} \int_t^{\infty} e^{\frac{\gamma}{\kappa}(r-t)} f(r) dr \tag{4.27}$$

Proof: Using the variation of parameters method, the particular solution of Equation (4.24) is given by indefinite integral

$$y_p(t) = \frac{e^{\frac{\gamma}{\kappa}t}}{\kappa} \int e^{\frac{\gamma}{\kappa}t} f(t) dt \tag{4.28}$$

By the fundamental theorem of calculus, the indefinite integral in Equation (4.28) can be written in terms of a definite integral and the function H shown in Equation (4.26) as

$$\int e^{\frac{\gamma}{\kappa}t} f(t) dt = \int_{t_1}^{t} e^{\frac{\gamma}{\kappa}t} f(t) dr + H(t_1) \tag{4.29}$$

Substituting Equation (4.29) in Equation (4.28) and switching the integral limits yield

$$y_p(t) = \frac{e^{\frac{\gamma}{\kappa}t}}{\kappa} \left(- \int_t^{t_1} e^{\frac{\gamma}{\kappa}t} f(t) dr + H(t_1) \right) \tag{4.30}$$

which is equivalent to Equation (4.25).

Now, suppose that $|f(t)| \leq |k.e^{\alpha t}| < |k.e^{|\frac{\gamma}{\kappa}|t}| \; \forall t \in J$ and $\frac{\gamma}{\kappa} < 0$, then

$$|H(t)| \leq \left| \int k e^{\frac{\gamma}{\kappa}t} e^{\alpha t} dt \right| = \left| \frac{k e^{(\frac{\gamma}{\kappa}+\alpha)t}}{\frac{\gamma}{\kappa}+\alpha} \right| \quad \forall t \in J \tag{4.31}$$

since $\frac{\gamma}{\kappa} < 0$ and $|\frac{\gamma}{\kappa}| > \alpha$, then as $t \to \infty$

$$\left| \frac{k e^{(\frac{\gamma}{\kappa}+\alpha)t}}{\frac{\gamma}{\kappa}+\alpha} \right| \to 0$$

so $H(\infty) = 0$ and Equation (4.27) follows. ■

To show that the LWT is the particular solution of the differential equation in Equation (4.20) substitute

$$\kappa = -(1-\zeta^2)a^p$$
$$\gamma = a^{p-1}\left(j(1-\zeta^2) + \zeta\sqrt{1-\zeta^2}\right)$$

in Equation (4.27) to get

$$y_p(t) = \tilde{f}_{L_\zeta}(t,a) = \left(\frac{a^{-p}}{1-\zeta^2}\right)\int_t^\infty e^{\left(\frac{-\zeta}{\sqrt{1-\zeta^2}}+j\right)\left(\frac{r-t}{a}\right)} f(r)dr \tag{4.32}$$

The result obtained in Theorem 4.2, can be extended to second and higher order LTI systems, by following the same technique.

When the this result is generalized to systems of 1st order differential equations, instead of a scalar wavelet function, we have a tensor of wavelets or wavelet tensor.

4.3 LWT of elementary signals and its basic properties

The Laplace wavelet transform can be evaluated for many basic signals. It inherits many properties from the Laplace transform and the SOULTI wavelet transform.

To simplify the relations obtained from evaluating the LWT, we will denote the constant value $\zeta/\sqrt{1-\zeta^2} - j$ by σ_0, so σ is now given by

$$\sigma = \frac{\sigma_0}{a} \tag{4.33}$$

and the LWT definition becomes

$$\tilde{f}_{L_\zeta}(\tau,\sigma) = ca^{-p}\int_\tau^\infty e^{-\frac{\sigma_0}{a}(t-\tau)} f(t)dt \tag{4.34}$$

Using Equation (4.34), the LWT for many basic signals is evaluated and shown in Table 4.1. Now, we provide two important lemmas that link the LWT of the derivative/integral of the signal to the LWT of the signal itself.

4.3.1 Laplace wavelet transform of derivatives

Lemma 4.3. *Let $J \subset (a,\infty) \subset \mathbb{R}$, and let $x(t) : J \to \mathbb{R}$ be differentiable and exponentially bounded as defined in Theorem 4.1, and let the LWT of $x(t)$ be given by Equation* (4.9)*, then the LWT wavelet transform of $\dot{x}(t)$ is given by*

$$\mathcal{W}_{L_\zeta}\{\dot{x}(t)\}(\tau,a) = \frac{\sigma_0}{a}\mathcal{W}_{L_\zeta}\{x(t)\} - a^{-p}cx(\tau) \tag{4.35}$$

Table 4.1: Laplace wavelet transform for basic signals.

#	$f(t)$	$\tilde{f}_{L_\zeta}(\tau, a)$
1	$u(t)$	$c\frac{a^{1-p}}{\sigma_0}$
2	$tu(t)$	$\frac{a^2}{\sigma_0^2} + \frac{a\tau}{\sigma_0}$
3	$t^2u(t)$	$a^{-p}c\left(\frac{a\tau^2}{\sigma_0} + \frac{2a^2\tau}{\sigma_0^2} + \frac{2a^3}{\sigma_0^3}\right)$
4	$e^{-\beta t}$	$c\frac{a^{1-p}e^{-\beta\tau}}{\sigma_0+\beta a}$
5	$\sin(\omega t)$	$ca^{-p}\frac{\omega a^2\cos(\omega\tau)+a\sigma_0\sin(\omega\tau)}{a^2\omega^2+\sigma_0^2}$
6	$\cos(\omega t)$	$ca^{-p}\frac{\sigma_0 a\cos(\omega\tau)-a^2\omega\sin(\omega\tau)}{a^2\omega^2+\sigma_0^2}$
7	$e^{-\xi t}\cos(\omega t)$	$ca^{-p}e^{-\xi\tau}\frac{(\sigma_0 a+\xi a^2)\cos(\omega\tau)-a^2\omega\sin(\omega\tau)}{a^2\omega^2+(\sigma_0+a\xi)^2}$
8	$e^{-\xi t}\sin(\omega t)$	$ca^{-p}e^{-\xi\tau}\frac{a^2\omega\cos(\omega\tau)+(\sigma_0 a+\xi a^2)\sin(\omega\tau)}{a^2\omega^2+(\sigma_0+a\xi)^2}$

Proof: Direct evaluation of the LWT of $\dot{x}(t)$ by the integration by parts gives

$$\mathcal{W}_{L_\zeta}\{\dot{x}(t)\}(\tau,a) = c\, a^{-p}\left[x(t)e^{-\sigma(t-\tau)}\Big|_\tau^\infty + \sigma\int_\tau^\infty x(t)e^{-\sigma(t-\tau)}dt\right] \tag{4.36}$$

The second term on the right side of Equation (4.36) is the LWT of $\frac{\sigma\, x(t))}{(ca^{-p})}$. After evaluating the first term, Equation (4.36) can be written as

$$\mathcal{W}_{L_\zeta}\{\dot{x}(t)\}(\tau,a) = c\, a^{-p}\left[-x(\tau) + \frac{\sigma}{c\, a^{-p}}\mathcal{W}_{L_\zeta}\{x(t)\}\right] \tag{4.37}$$

which is equivalent to Equation (4.35) ■

4.3.2 Laplace wavelet transform of integrals

Lemma 4.4. *Let $J \subset (a,\infty) \subset \mathbb{R}$, and let $x(t) : J \to \mathbb{R}$ be exponentially bounded as defined in Theorem 4.1, and the LWT of $x(t)$ be given by Equation (4.9), then the LWT of $\chi(t)$, defined by*

$$\chi(t) = X(t) - X(a) = \int_a^t x(r)dr \tag{4.38}$$

is given by

$$\mathcal{W}_{L_\zeta}\{\dot{\chi}(t)\}(\tau,a) = \frac{c\, a\, \chi(\tau)}{\sigma_0} + \frac{a}{\sigma_0}\mathcal{W}_{L_\zeta}\{x(t)\} \tag{4.39}$$

Proof: Similar to Lemma 4.3, direct evaluation by integration by parts of the transformation integral leads to

$$\mathcal{W}_{L_\zeta}\{\chi(t)\}(\tau,a) = c\, a^{-p}\left[\frac{\chi(\tau)\, e^{-\sigma(t-\tau)}}{-\sigma}\Big|_\tau^\infty + \frac{1}{\sigma}\int_\tau^\infty x(t)\, e^{-\sigma(t-\tau)}dt\right] \tag{4.40}$$

The second term on the right side of Equation (4.40) is the LWT of $\frac{x(t)}{c\,\sigma\,a^{-p}}$. After evaluating the first term on the right side, Equation (4.40) becomes

$$\mathcal{W}_{L_\zeta}\{\chi(t)\}(\tau,a) = c\,a^{-p}\left[\frac{\chi(\tau)}{\sigma} + \frac{a^{1+p}}{c\,\sigma_0}\mathcal{W}_{L_\zeta}\{x(t)\}\right] \tag{4.41}$$

which is identical to the formula in Equation (4.39) ■

4.3.3 Region of convergence

The region of convergence of the LWT integral depends on the exponential boundedness of the signal, see Proposition 3.1. If $f(t)$ is exponentially bounded, then the Laplace wavelet transform is convergent in the scale region defined by

$$0 < a < \frac{\zeta}{\alpha\sqrt{1-\zeta^2}} \tag{4.42}$$

4.3.4 Time-frequency resolution

The Laplace wavelets possess some advantages over the SOULTI wavelets. The time-frequency resolution is an important quantity that tells the accuracy within which time and frequency information can be localized on the time-frequency domain or the time-scale domain, when scale and frequency can be related.

There are different ways to define the time-frequency resolution of a signal as described in Chapter 3. However, the standard deviation based approach does not apply because of the zero-pole cancellation that leaves the Laplace wavelet a first order filter with first order transfer function in the frequency domain. Computing the center of mass for the magnitude function of a first order function does not converge, thus the standard deviation approach is not valid. Moreover, it has less significant meaning regarding frequency filtering and isolation.

Therefore, the systems theory based definitions are considered. In particular, we are presenting the quality factor based definition. The quality factor is the ratio of the peak response to the zero frequency response [90]. Let us start by finding the wavelet frequency at the maximum magnitude. The square of the magnitude of the Laplace wavelet in the frequency domain is given by

$$\left|a\Psi_{L_\zeta}(a\omega)\right|^2 = \frac{a^{2-2p}}{(1-\zeta^2)^4(a\omega-1)^2 + \zeta^2(1-\zeta^2)^2} \tag{4.43}$$

differentiating Equation (4.43) with respect to ω and equating it to zero yields

$$\frac{d\left|a\Psi_{L_\zeta}(a\omega)\right|^2}{dt} = \frac{-a^{2-2p}(2a(1-\zeta^2)^4(a\omega-1))}{\left((1-\zeta^2)^4(a\omega-1)^2 + \zeta^2(1-\zeta^2)^2\right)^2} = 0 \tag{4.44}$$

which when solved for ω gives the frequency at the peak value by

$$\omega_p = \frac{1}{a} \tag{4.45}$$

This is a very important result since it shows that the frequency of the wavelet filter at the peak amplitude is the reciprocal of the scale. The relation is exact and the derivation did not involve any approximation. Figure 4.3 shows the Laplace wavelet function in the frequency domain at different scales, $a = 1, \frac{1}{2}, \ldots, \frac{1}{10}$. The figure clearly shows the exact centering of the peak value at exactly the frequency $1/a$.

Now, we can find the peak value of the filter. Substituting ω_p from Equation (4.45) back into Equation (4.43) gives the peak magnitude as

$$Q = \frac{a^{1-p}}{\zeta\sqrt{1-\zeta^2}} \tag{4.46}$$

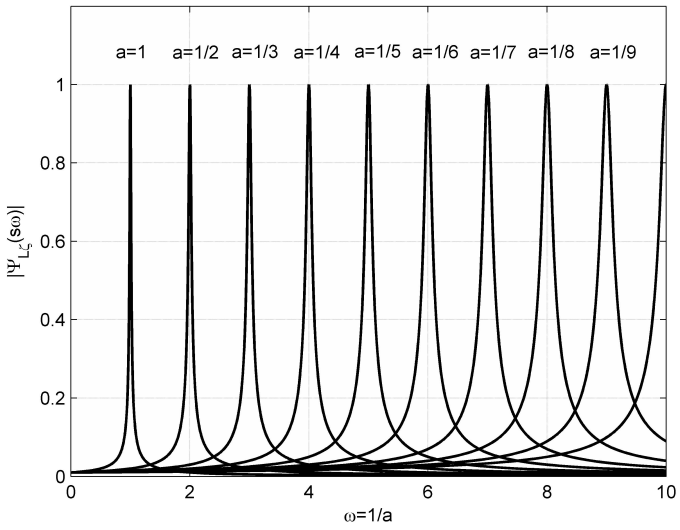

Figure 4.3: Laplace wavelet at different scales in the frequency domain. $\zeta = 0.01$.

The effective frequency window, which is the half-power bandwidth, is the difference between the frequencies at half peak power, namely $\left|a\Psi_{L_\zeta}(a\omega)\right| = Q/\sqrt{2}$. Solving for the frequencies at $Q/\sqrt{2}$ and taking their difference give the frequency bandwidth as

$$\Delta\Omega_Q = \frac{2\zeta}{\sqrt{1-\zeta^2}}\omega_p \tag{4.47}$$

It is important to note that the $\Delta\Omega_Q$ bandwidth window of the Laplace wavelet is symmetric about the peak frequency, that is

$$\omega\big|_{\frac{Q}{\sqrt{2}}} = \omega_p \pm \frac{\zeta}{\sqrt{1-\zeta^2}}\omega_p \tag{4.48}$$

Figure 4.4 shows the Laplace wavelet with the half-power bandwidth, as explained in the previous analysis.

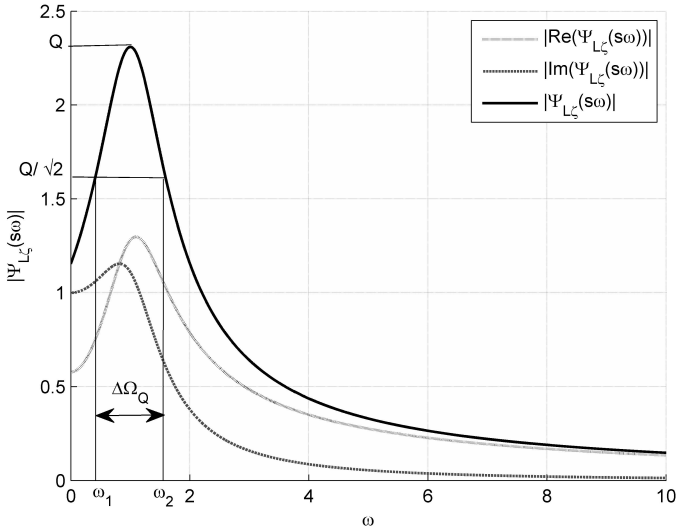

Figure 4.4: Laplace wavelet in the frequency domain with quality factor, half-power points, and half-power bandwidth marked. $\zeta = 0.5$.

The effective time window depends on the exponential decay part of the Laplace wavelet function. Therefore, the time window based on the 2% settling time will be given by

$$\Delta T_{2\%} \simeq \frac{4a\sqrt{1-\zeta^2}}{\zeta} \tag{4.49}$$

The time-frequency resolution, which is the product of the frequency resolution and the time resolution, becomes

$$\mu = \Delta\Omega_Q.\Delta T_{2\%} = \frac{2\zeta}{\sqrt{1-\zeta^2}}\omega_p.\frac{4a\sqrt{1-\zeta^2}}{\zeta} = 8 \tag{4.50}$$

which is equal to the result obtained for the SOULTI wavelet 3.4. However, the derivation of the frequency bandwidth in the SOULTI case involved some approximation, while the formula is exact in the case of the Laplace wavelet. It is important to note that a 2% settling time is too conservative limit for the time window, which can be shortened to 5% or 10% settling times.

The Laplace wavelet can be normalized by its frequency response peak value, Q, to make the peak value equal to unity at all values of ζ, thus the normalized Laplace wavelet becomes

$$\bar{\psi}_{L_\zeta}(\tau, a) = \left(\frac{\zeta}{a\sqrt{1-\zeta^2}}\right) e^{\left(\frac{-\zeta}{\sqrt{1-\zeta^2}}+j\right)\left(\frac{t-\tau}{a}\right)} u(t-\tau) \tag{4.51}$$

In all the applications presented in the following chapters, the normalized version of the Laplace wavelet is employed and the over-bar notation is dropped. The previous analysis shows improvement over the properties of the the real SOULTI wavelet. Figure 4.4 shows the Laplace wavelet with both the real and the imaginary components in the frequency domain. The imaginary component represents the SOULTI wavelet, and it is clear that the Laplace peak value is centered between the real and imaginary components peaks. As a result, the Laplace wavelet is expected to give better frequency identification and detect more precisely the change in frequencies.

Chapter 5

Harmonic Analysis

The content of this chapter is extracted from a study by the author of this dissertation that is published in the Journal of Vibration and Control [2].

The SOULTI and the Laplace wavelets can be useful in the analysis of dynamic systems especially the harmonic analysis. The Localized harmonic analysis is a desired analysis for many vibrations and acoustics applications. Generating spectrograms for time series demonstrate how the localized frequency spectra of the time series evolve with time.

Before using the SWT or the LWT, the important question that a researcher has to answer is what range of scales does yield useful information from the analysis? If the range is determined, how many scales are needed, or what is the minimum scale increment possible? Once these questions are answered correctly, the analysis can be performed with confidence about the results. Arbitrary analysis without careful scale range and increment choice yields erroneous analysis or meaningless one.

Therefore, a presentation is first offered for a correct analysis scales selection, which forms a pre-analysis for the wavelet analysis. Then, some applications that cover the instantaneous frequency detection and the modal separation of LTI systems are presented in the subsequent sections. The development relies on the properties and characteristics of the wavelets presented in the previous chapters. The major part of the modal separation analysis is presented with the Laplace wavelets. However, the same steps can be applied using the SOULTI wavelets. Moreover, the described pre-analysis can be applied to other families of harmonic wavelets, not just the SOULTI and the Laplace wavelets.

5.1 Numerical computation of the continuous SOULTI and Laplace wavelet transforms for discrete time-series

In Real applications, we have discrete representation of signals as discrete time series. Therefore, we have to adapt the continuous formulas of the continuous wavelet transforms to process discrete data, yet produce output that resembles the continuous wavelet transform to the closest degree possible. Usually the time-scale analysis is performed, then it is converted to the time-frequency domain. The first step before the analysis starts is to determine the upper and lower limits of the wavelets scales range. Selecting the range of scales and the appropriate number of them should rely on the Shannon theory and the Nyquist Criteria if the harmonic analysis is the goal. This is only possible if a one-to-one relation between the frequency content of the wavelets and the scales exists. This condition is well served in both the SOULTI and the Laplace wavelets. The relationship between the positive frequency domain and the positive scale domain is bijective, as demonstrated by Equations (3.80) and (4.45).

The analysis can be started from the sampling frequency of the time-series, f_s. The maximum frequency that can be extracted from the signal is defined by the Nyquist criterion as $f_s/2$. Therefore, using Equations (3.80) and (4.45), the lower limit of the scale range is given by

$$a_{min} = \frac{1}{\pi f_s} \tag{5.1}$$

However, the smallest possible frequency in any time series depends on the length of this time series. Where the smallest frequency is given by

$$f_{min} = \frac{f_s}{N_s} \tag{5.2}$$

where N_s is the number of samples in the series. Consequently, the maximum possible scale is defined as

$$a_{max} = \frac{N_s}{2\pi f_s} \tag{5.3}$$

In continuous time series, the scale can take any positive real value, i.e. $a \in \mathbb{R}$, so the number of possible scales is uncountable. This implies that the analysis with a fraction of a wavelet length is possible, or the number of wavelets can be non-integer. However, with discrete time series the transform integral is approximated as a summation, hence an uncountable number of scales is not feasible.

Assuming that the maximum possible scale for a signal is given by Equation (5.3), then the next possible smaller scale is

$$a_{N_s-1} = \frac{N_s - 1}{2\pi f_s} \tag{5.4}$$

So the set of scales can be defined by

$$a[i] = \frac{i}{2\pi f_s},\ i = 2, 3, \ldots, N_s \tag{5.5}$$

Similarly and using Equations (3.80) and (4.45), the time-frequency analysis can be performed directly. The set of frequencies are defined as

$$\omega[i] = \frac{2\pi f_s}{i},\ i = 2, 3, \ldots, N_s \tag{5.6}$$

The following definition defines the continuous SWT of discrete time-series based on simple trapezoidal integration.

Suppose that the time series $f(t[k])$ is defined for the time samples $\{t[k]\}$ where $k = 1, 2, \ldots, N_s$. Then, based on Equations (5.5) and (5.6), the continuous wavelet transform of f_k with respect to the wavelet $\psi(t)$ can computed using the trapezoidal rule by

$$\bar{f}_\zeta(\tau[n], a[i]) = \sum_{k=n}^{N_s-1} \frac{\psi^{\tau[n],a[i]}(t[k+1]) f\left(t[k+1]\right) + \psi^{\tau[n],a[i]}(t[k]) f\left(t[k]\right)}{2} \Delta t_k \tag{5.7}$$

where $\Delta t_k = t[k+1] - t[k]$, and $n = 1, 2, \ldots, N_s - 1$. Computationally, Equation (5.7) is not the most efficient way to compute the continuous wavelet transform. Equation (5.7) can be rewritten in the general inner product form as $\bar{f}_\zeta(\tau[n], a[i]) = \langle \psi^{\tau[n],a[i]}(t[k]), f\left(t[k]\right) \rangle$, which is equivalent to the rectangular integration rule with normalized time, i.e. $\Delta t_k = 1$. The inner product is computed as

$$\bar{f}_\zeta(\tau[n], a[i]) = \sum_{k=n}^{N_s-1} \psi^{\tau[n],a[i]}(t[k]) f\left(t[k]\right) \tag{5.8}$$

The discrete convolution or the discrete X-correlation formulas are usually used. The difference between the discrete X-correlation, $Xcorr(n)$, and the rectangular integration rule is the limits of summation. The wavelet transform can be extracted from the X-correlation by taking the values between $Xcorr(N_s)$ and $Xcorr(2N_s)$. The convolution summation can also be used, but after reflecting the wavelet about the vertical axis. Therefore the wavelet transform can be found as

$$\bar{f}_\zeta(\tau[n], a[i]) = \psi^{\tau[n],a[i]}(-t[k]) * f\left(t[k]\right) \tag{5.9}$$

5.2 Resolving instantaneous frequency in frequency time-varying signals

A potential application of the SOULTI and Laplace wavelets is producing evolutionary spectrums (spectrograms). Wavelets overcome the fixed window width limitation of the STFT,

at the same time it performs better than the other wavelets because of the accurate and direct relation between scale and frequency. To validate the capability of the SOULTI wavelet in detecting the frequency spectrum evolution, or the scale evolution with respect to time, we present some examples of the SOULTI and Laplace wavelets analysis of noisy finite time signals at different Signal to Noise Ratio (SNR) levels.

It is important to emphasize that the continuous version of the wavelet transform is performed in these examples, where the transform integral is performed numerically. In all the examples, =0.1 is used because it gives the wavelet a large quality factor value as shown in Figure 3.6.

5.2.1 SOULTI wavelet example

First, two noisy signals with the same frequency are tested. The first has $SNR = 15$dB, and the second has $SNR = 7.5$dB. Figure 5.1 shows the two signals. Figure 5.2 shows the contour map of the two signal transforms. We notice that in both cases ridges of peaks

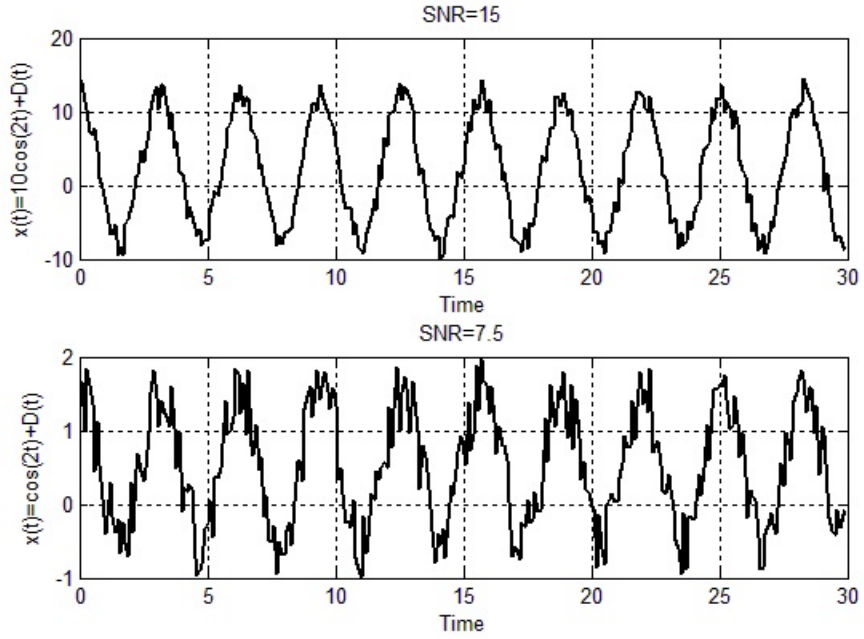

Figure 5.1: Top: single harmonic with white noise of $SNR = 15$dB. Bottom: single harmonic with white noise of $SNR = 7.5$dB.

are distinctly recognized at $s = \frac{1}{2}$, which corresponds to $\omega = 2$rad/s by the scale-frequency relation in Equation (3.5). The ridge of the wavelet transform is the set of points in the time-scale domain Θ, where the wavelet integral has stationary points $(t, s) \in \Theta$ such that

$t_s(t,s) = s$, where t_s is a stationary point, i.e. $\left.\frac{d\tilde{f}_\zeta(\tau,s)}{ds}\right|_{t_s} = 0$ [128]. Notice, also, that at the end of the signal, the transform is distorted and the peaks diminish due to the edge effect. Also, notice that since the SOULTI wavelet is causal, the edge effect appears at the end of the time scale of the signal only, and the noisy signal with $SNR = 7.5$dB has slightly worse edge effect.

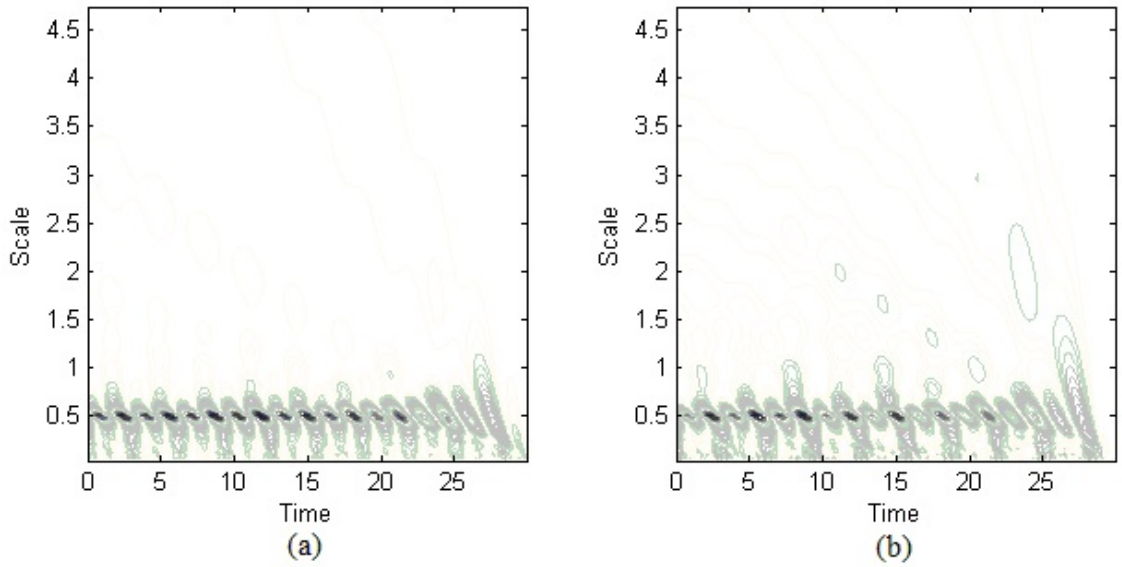

Figure 5.2: Contour mapping of the SOULTI wavelet Transform of a harmonic signal of frequency=2rad/s. (a) $SNR = 15$dB (b) $SNR = 7.5$dB.

In the second test, a signal carrying 2 different frequencies is analyzed. The signal has $SNR = 15$dB and is graphed in Figure 5.3. Figure 5.4 shows 2 mappings. The first maps the contours on the time-scale domain, and it shows clearly two ridges that stretch along two lines of constant scale, $s = 0.125$ and $s = 0.5$, parallel to the time axis. The second plots the contours on the time-frequency domain. The scale-frequency conversion is performed using Equation (3.5). The ridges stretch along the constant frequency values $\omega = 2$rad/s and $\omega = 8$rad/s.

The advantage of the time-scale or time-frequency analysis over classic frequency analysis is more useful in analyzing time-varying and nonlinear oscillations. In this example, we analyze a signal consisting of combination of constant harmonics with linear chirp as a time-varying frequency component. White noise is added to the signal with $SNR = 20$dB. The signal is given by Equation (5.10).

$$x(t) = 10\sin(0.4t^2) + 5\cos(2t) + 8\sin(t + \frac{pi}{7}) + D(t) \tag{5.10}$$

where $D(t)$ represents the white noise or the disturbance term. Figure 5.5 plots the signal in

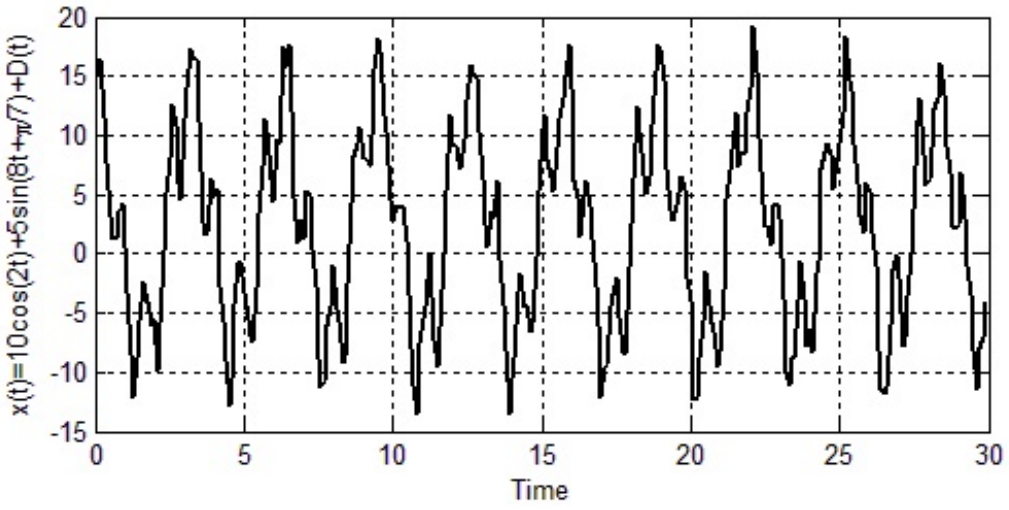

Figure 5.3: Sum of two harmonics with white noise. $\omega_1 = 2$rad/s, $\omega_2 = 8$rad/s, and the $SNR = 15$dB.

the time domain. Performing Fourier analysis to the signal does not reveal the instantaneous frequency change in the signal. Figure 5.6 shows the Fast Fourier Transform (FFT) and the Welch averaging of the frequency spectrum. While the FFT identifies the constant harmonics with peaks at $\omega = 1$rad/s and $\omega = 2$rad/s, there is no way to distinguish the instantaneous frequency change from the FFT. The Welch averaging does not identify even the constant harmonics because of the interference from the frequency-changing component.

Figure 5.7 shows the SOULTI wavelet transform of the signal. The transform distinctly traces the instantaneous frequency with respect to time, where the dashed lines represent ridgelines that trace this frequency along time. When examining the time varying component in Equation (5.10) we find that the instantaneous frequency is given by $\omega(t) = 0.8t$rad/s, which is the equation of the dashed line on the time-frequency wavelet mapping shown in Figure 5.7.b. The dashed curve in Figure 5.7.a is the inverse of the line $\omega = 0.8t$rad/s, namely $s(t) = 1/0.8t$s/rad, which conforms to the scale-frequency relation in Equation (3.5). Notice also, that the other two constant frequencies are identified along ridgelines of almost constant scales at s=0.5 and s=1 in Figure 5.7.a and along ridgelines of almost constant frequency at $\omega = 1$ and $\omega = 2$ in Figure 5.7.b. On Figure 5.7.a, the parabolic dashed line, which traces the instantaneous change of the chirp frequency, intersects the $s = 1$ and the $s = 0.5$ lines at times $t = 0.26$s and $t = 1.6$s respectively.

As a comparison between the SOULTI wavelet and other wavelets in resolving frequencies with respect to time, the same chirp signal is analyzed with four different wavelets, Morlet, complex Shannon, Mexican hat, and the frequency B-Spline. The four wavelets scalogram graphs are shown in Figure 5.8. Notice that the four are able to resolve the chirp into curves parabolic in shape with different ridge widths. However, the curves are not the reciprocal

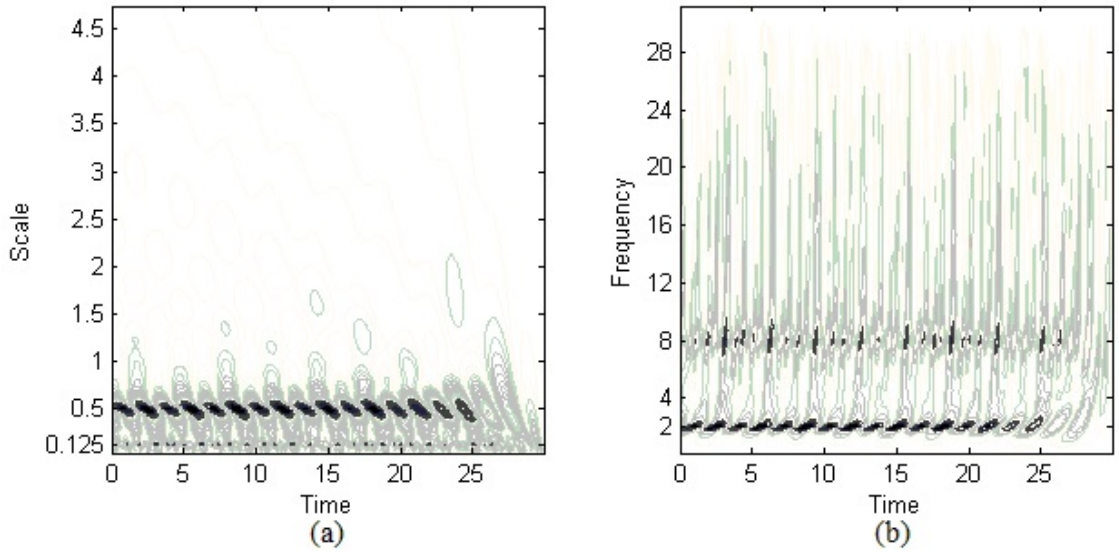

Figure 5.4: SOULTI wavelet transform for the two harmonics signal in Figure 5.3. (a) Time-scale contour mapping. (b) Time-frequency contour mapping.

of the instantaneous frequency. In addition, the constant scale ridges are not at scales that can be easily matched to frequencies.

The Mexican hat wavelet gives the best match to the parabolic curve, but when resolving the constant frequencies in the signal it shows large shifts. It is difficult to infer the accurate frequencies in the signal from these wavelets scalogram maps, though one can infer qualitative information about the shape of the instantaneous frequency change with respect to time. For each wavelet, the relation between the scale and the frequency along the ridgeline is different, but one can argue that it is the reciprocal of some function of the instantaneous frequency.

From the previous discussion, we conclude that it is difficult to construct a spectrogram for each scalogram shown in Figure 5.8. However, the SOULTI wavelet scalogram can be directly transformed into spectrogram by applying the scale-frequency change in Equation (3.5).

To evaluate the SOULTI wavelet spectrogram, we compare it to the Short Time Fourier Transform (STFT) spectrograms. Six spectrograms based on the STFT were computed for different window sizes (W) samples. To make the comparison compatible with the continuous wavelet transform, the window overlap is set as $(W-1)$ to perform window sweep over the time vector of the signal. Figure 5.9 plots the spectrograms with the three straight lines imposed on it that represent the instantaneous frequencies. Note that the narrow windows ($W64$) are better in resolving the linear chirp than in resolving the constant frequencies. While the wider windows ($W128$) are better in resolving the constant frequencies.

The wider the window, the less time resolution is obtained, the more end effect occurs, and the more time truncation from both sides of the signal is taken. For example, Figure 5.9.f

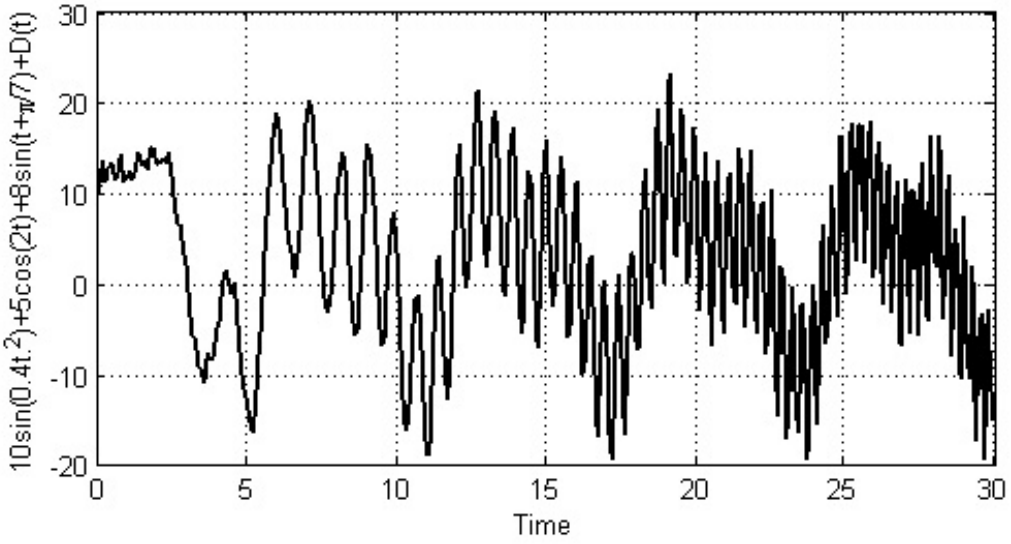

Figure 5.5: Two constant harmonics with a time varying frequency component signal.

only shows frequency information for the period $12.8 \leq t \leq 17.2$s of the signal. Frequency information for periods $0 \leq t < 12.8$s and $17.2 < t \leq 30$s is not available, while the SOULTI wavelet spectrogram provides information for the duration of the signal as shown on Figure 5.7.b. Moreover, the SOULTI spectrogram resolves both the linear chirp and the constant harmonics, and the direct link with the scalogram allows checking the results for small or close frequencies.

Edge effect mitigation

Edge effect in harmonic and wavelet analysis of finite duration signals is caused by many factors. First, the measured signals are finite in duration, and we do not have information about the signal after or before the times of recording. Second, many wavelets do not have compact support, rather they have effective window. Third, at the beginning of the signal, say ($t = 0$), the wavelet window has part of it outside the signal range, before $t = 0$, so the inner product is computed between the signal and part of the wavelet. Similarly, at the end of the signal, the wavelet effective window will move out of the signal range, and part of it will take part in the inner product with the signal. This partial inner product gives inaccurate results at both edges.

The SOULTI wavelet is a right sided wavelet or signal, i.e. the mother wavelet is zero for $t < 0$. Therefore, when performing the wavelet transform, the effective wavelet window starts sweeping the signal from the position where the window sets fully inside the range of the signal. However, at the end of the signal, the effective window moves out of the signal range, and the inner product is performed between the signal and part of the effective window.

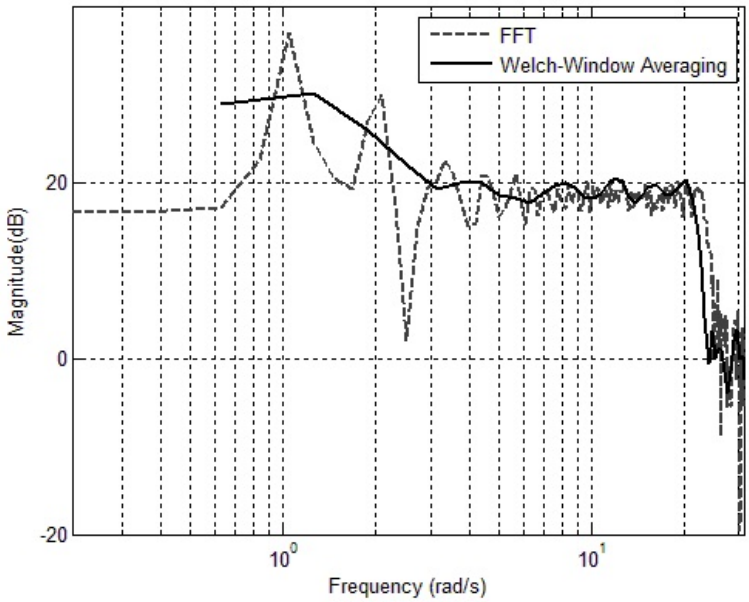

Figure 5.6: Frequency spectrum of the signal described by 5.10. (Dashed line) FFT. (Solid line) Welsh spectrum averaging

Therefore, though the SOULTI wavelet solves naturally the edge effect at the beginning, it does not solve the problem at the end, which makes the analysis at the end inaccurate and distorted.

As a solution for the end edge effect, we propose in this section performing a Reverse Wavelet Transform (RWT) analysis starting from the end of the signal. So the mother wavelet is reflected about $t = 0$, then it is shifted to the end of the signal, and the wavelet analysis is performed end-to-start. Then we reflect the results back with respect to time. The same result can be obtained by just reflecting the signal and perform the wavelet analysis as usual. Then, we reflect the results back.

Figure 5.10 shows the RWT of the signal in Figure 5.3, and 5.11 shows the RWT of the signal in Figure 5.5. Note that at the end of the signal, there are clear ridges in both the scalograms and the spectrograms, while the beginning shows distortions. This result gives an indication that the distortion of the ridges at the end of the signal is due to the edge effect.

Instead of producing two scalograms or spectrograms for each signal, the average of the Forward Wavelet Transform (FWT) and the RWT can be computed and mapped to give refined results at both ends of the signal. Figure 5.12 shows the average between the FWT and RWT. The edges are better resolved and the distortion at the edges almost disappeared. However, a slight reduction in the ridges amplitude is notices.

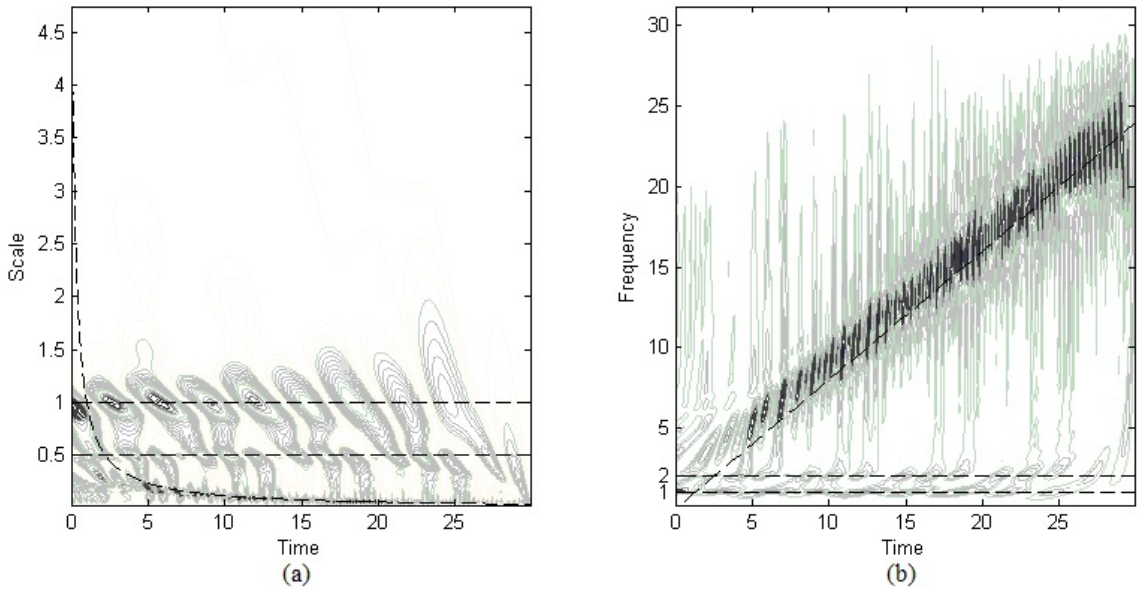

Figure 5.7: SOULTI wavelet transform for the chirp signal described by Equation (5.10) and shown in Figure 5.5. (a) Scalogram (Time-scale) contour mapping (b) Spectrogram (Time-frequency) contour mapping.

5.2.2 Laplace wavelet example

The LWT has attractive potential for applications in signal processing of vibratory systems and modal parameters identification. As shown in the previous section, the Laplace wavelet has better controlled frequency bandwidth, precisely centered and controlled filter over the desired frequencies, and good time-frequency resolution.

As a simple start for testing the capabilities of the LWT, we are processing chirps of different orders with some constant harmonics. Then, a simple example on mode separation of a three Degree-Of-Freedom (DOF) linear mass-spring system is presented.

The Laplace wavelet can be controlled precisely to detect frequency change over time and for any frequency range. In this example, we are processing a signal consisting of quadratic chirp mixed with noise and constant harmonics at 135Hz and 350Hz. The analyzed signal is given by

$$S(t) = \cos\left(\frac{200\pi}{3}t^3 + 200\pi t\right) + 2\sin(270\pi t) + \sin(700\pi t) + n(t) \tag{5.11}$$

where $n(t)$ is a white noise component. The Signal to Noise Ratio (SNR) of $S(t)$ is 15dB. Figure 5.13 shows the signal $S(t)$.

Processing the signal $S(t)$ using the LWT reveals the frequency content of the signal and distinctly traces the time-varying frequency. Figure 5.14 shows the time-scale (scalogram) and the time-frequency (spectrogram) of $S(t)$. The Spectrogram precisely shows the constant

harmonics at 2199.1rad/s = 350Hz and 848.23rad/s = 135Hz in addition to the quadratic chirp, which is traced along the parabola $a(t) = 200\pi t^2 + 200\pi$. The scalogram shows the reciprocal of the frequency and traces the quadratic term, which changes according to the curve $a(t) = \frac{1}{200\pi t^2 + 200\pi}$.

5.3 Analysis of a three degree-of-freedom mechanical system

This section introduces brief analysis of a 3DOF mechanical system consisting of 3 masses and 3 springs, and some friction, a schematic diagram is shown in Figure 5.15(a), while the actual testing bench is shown in Figure 5.15(b).

This example shows the capability of the Laplace wavelets in decoupling the modes of vibration. The analysis here can be considered as an introduction or a first step in system identification. The classical methods of system identification behave well with linear systems, see [58], however the LWT provides direct information and shortcuts some steps, so one can directly estimates the frequencies and the mode-shapes, and then the damping. Though, we are confident of this system linearity, this confidence is not usually available with other systems, so one of the advantages that can be attained by applying the LWT is confirming or negating the LTI behavior of systems through revealing the change of natural frequencies with respect to time. LTI systems have constant natural frequencies, while nonlinear systems and time-variant systems have time-variant oscillatory frequencies.

5.3.1 Experiment and measurement system description

An impulse test was done on the 3-mass test system shown in Figure 5.15(b). The test was performed on the system using a test hammer with a rubber head. The impulse was applied to mass M_3 as shown in Figure 5.15(a), then the acceleration of each mass was recorded at a sampling rate of 500Hz using NI-6321 data acquisition card from National Instruments with LabView-2015 software. The software ran on a laptop computer with 2.4GHz i7 dual-core processor and Windows-10 operating system. The acceleration was measured using single-axis PCB accelerometers of 10mv/g nominal sensitivity. The accelerometers were calibrated before testing and the accurate sensitivities were used in the data conversion.

The acceleration signal can be used after filtration and detrending in the analysis, but since the acceleration signal amplifies the high frequency modes and reduces the SNR of the low frequency modes, we will obtain the velocities and the displacements for the analysis as well. The velocities and the displacements are obtained by integrating the acceleration. Figure 5.16 shows the acceleration, velocity, and displacement of the three masses, M_1, M_2, and M_3. Figure 5.16 shows a constant bias in the acceleration measurement, which is

typical of accelerometers due to gravity and angular inclinations. Before the velocities and the displacements were obtained, the measured acceleration signals were detrended, and the trends were largely reduced. However, the remaining trending error accrues by integration, so the trending error propagation into the displacement is the largest, see Figure 5.16(c), (f), and (i).

5.3.2 Time-frequency analysis by the Laplace wavelets

The LWT, with $\zeta = 0.01$, was applied to the acceleration, velocity, and displacement of the three masses. Figure 5.17 shows the response spectrograms of the masses $M1$, M_2 and M_3.

By examining the LWT spectrograms of the acceleration in Figure 5.17, we only find two ridges extending at two constant frequencies, 11.6 Hz and 31 Hz. Each ridge is centered about a modal frequency, and we see that the ridge at $f = 31$ Hz is larger, which signifies that the dominant frequency in the acceleration signal for all three masses is the highest frequency. The wavelet transforms evaluated along these ridges are called Skeletons. By comparing the spectrograms of the acceleration with those of velocity, we notice a third ridge at a frequency of 1.6 Hz, which may appear on the acceleration spectrogram if the number of contour lines is increased. On the other hand, the spectrograms of the displacement of M_1 and M_3 show weak traces of the 31 Hz ridgeline and clear ridges of the two lowest frequencies.

These results coincide with the results obtained from the spectrum of the nine response signals shown in Figure 5.18. We can identify peaks at 1.6 Hz, 11.6 Hz and 31 Hz. However, the spectrum shows some peaks at 0.3 Hz, in Figures 5.18 (a), (d), (e), (g), (h) and (i). The best results can be obtained from the LWT spectrogram of the velocities. They give three distinct ridges as shown in Figure 5.17(b), (e), and (h).

The LWT gives similar and relatively better result than most harmonic wavelets. To validate the LWT results and compare its advantages with the other wavelets, the spectrograms using the analytic Morse [79] and the Morlet wavelets [94] in addition to the STFT spectrograms were computed for the response signals.

The continuous wavelet transform was computed in this example. The LWT was computed by discretizing the integration in Equation (4.4) as

$$\bar{f}_{L_\zeta}(n,m) = \left(\frac{m^{-p}}{1-\zeta^2}\right) \sum_{i=n}^{N} \overline{e^{\left(\frac{-\zeta}{\sqrt{1-\zeta^2}}+j\right)\left(\frac{i-n}{m}\right)\Delta t_i}} f(\Delta t_i)\Delta t_i \tag{5.12}$$

where n and m are the discrete time and frequency variables respectively, and Δt_i is the sampling time of the signal $f(t)$. To have an equivalent comparison, the Morlet wavelet transform is computed in a similar way using Equation (5.12). The Morlet wavelet used is defined by

$$\psi_m(t) = e^{\frac{-t^2}{2}} \cos(\omega t); \tag{5.13}$$

The Morse wavelet transform is computed using the package developed by [78], and the Morse wavelets family employed in the analysis has a symmetry parameter value $\gamma = 3$ and time-bandwidth product $\sqrt{\beta\gamma} = 60$. Figure 5.19 shows the Morse wavelet spectrograms of the acceleration, velocity, and displacement of the three masses. The results are similar to the LWT results, but the Morse wavelets ridges are wider, and the ridges of the displacement analysis are wider, shorter, and less visible than the LWT ridges.

The Morlet wavelet is one of the standard wavelets for time-frequency analysis. Figure 5.20 shows the Morlet wavelet spectrograms of the responses. The results are less crisp and do not resolve all the frequencies in the response, especially for the displacement response. Moreover, unexpected ridges at frequencies different from the modal frequency are clear and numerous, see Figure 5.20 (a), (g), and (h).

The last comparison is made with the STFT, which is the classic method for obtaining an evolutionary spectrum or spectrogram in vibration analysis. Figure 5.21 presents the STFT spectrograms of the response signals. The spectrograms are narrow and extend accurately along the modal frequencies in some spectrograms, but they only reveal the lowest modal frequency in the displacement signal. In addition, the acceleration spectrograms for the masses M_2 and M_3 do not show any ridge at the lowest modal frequency. Conversely, the acceleration spectrogram of mass M_1 shows four ridges, and we notice an unexpected ridge around $20Hz$, which is not a modal frequency of the system. The clearest results are those from the velocity; however, the STFT suffers from data cuts from start and end of signals equal to the analysis window length. The analysis window used in the STFT is 1 second of length, and notice a 1 second cut from both ends of the spectrograms time axis.

5.3.3 Modes decomposition

By using the FFT spectrum as a reference, we find that the ridges of the LWT spectrograms extend along the three modal frequencies. In the following analysis, we employ the velocity response of the three masses because its spectrograms offer clear distinct ridges at these modal frequencies. Since the system possesses only three major frequencies that are constant with respect to time, this gives strong indication that the system behaves linearly in the range of operation that has been tested. Therefore, the mode i of the response is given by

$$x_i(t) = \sum_{k=1}^{3} e^{\xi_k \omega_k t} \left(c_{ki_1} \cos(\omega_k t) + c_{ki_2} \sin(\omega_k t) \right) \tag{5.14}$$

From Table 4.1, the LWT of the response in Equation (5.14) is given by

$$\mathcal{W}_{L_\zeta}\{x_i(t)\} = \sum_{k=1}^{3} e^{-\xi_k \tau} \left(\frac{c_{ki_1} \left((\sigma_0 a + \xi_k a^2) \cos(\omega_k \tau) - a^2 \omega_k \sin(\omega_k \tau) \right)}{a^2 \omega_k^2 + (\sigma_0 + a\xi_k)^2} + \frac{c_{ki_2} \left(a^2 \omega_k \cos(\omega_k \tau) + (\sigma_0 a + \xi_k a^2) \sin(\omega_k \tau) \right)}{a^2 \omega_k^2 + (\sigma_0 + a\xi_k)^2} \right) \quad (5.15)$$

which shows that the LWT preserves the frequency and the exponential decay of the original signal. The result in Equation (5.15) is a complex valued function. With some algebraic manipulations, it can be shown that the norm of Equation (5.15), which is used to plot the spectrograms is given by

$$|\mathcal{W}_{L_\zeta}\{x_i(t)\}| = \sum_{k=1}^{3} e^{-\xi_k \omega_k \tau} \left(c_{ki_1} \sqrt{\frac{\frac{a^4\omega_k^2}{2} + \frac{h}{2} + \sqrt{\left(\frac{a^4\omega_k^2 - h}{2}\right)^2 + \left((aD + a^2\xi_k)a^2\omega\right)^2} \sin\left(2\omega_k\tau + \phi_k\right)}{\left(a^2(\omega_k^2 + \xi_k^2) + 2a\xi_k\right)^2 + 4\left(D + a\xi\right)^2}} + c_{ki_2} \sqrt{\frac{\frac{a^4\omega_k^2}{2} + \frac{h}{2} + \sqrt{\left(\frac{a^4\omega_k^2 - h}{2}\right)^2 + \left((ax + a^2\xi_k)a^2\omega_k\right)^2} \cos\left(2\omega_k\tau + \phi_k\right)}{\left(a^2(\omega_k^2 + \xi_k^2) + 2a\xi_k\right)^2 + 4\left(D + a\xi_k\right)^2}} \right) \quad (5.16)$$

where $h = ((aD + a^2\xi)^2 + a^2)$ and $D = \frac{\zeta}{\sqrt{1-\zeta^2}}$. The terms under the radical, in Equation (5.16), show that the norm adds a constant gain multiplied by an exponential term. Note that the sinusoidal terms' argument have $2\omega_k\tau$ and $\cos(2\omega_k\tau+\phi) = 2\cos^2(\omega_k\tau+\phi/2)-1$. Therefore, we would expect the transform to look as a decaying oscillations added to an exponentially decaying function.

Figure 5.22 shows skeletons at the spectrogram's ridges of the displacement, which are the skeletons along the ridges in Figure 5.17.c. Each skeleton line decays to zero, and each carries a different major frequency. The skeleton lines show offset from the zero axis because they represent the norm of the transform which is greater than or equal to zero, and this adds an offset to the results as shown by Equation (5.16). The skeletons represent the LWT at the scales corresponding to the central frequencies of the ridges. Notice that the first mode $f_1 = 1.6$ Hz is the most dominant mode in the displacement spectrograms. Figure 5.22(b) and (c) show that its effect propagates to the second and third modes.

Figures 5.23 to 5.25 show the skeletons at the modal ridges of the velocity spectrograms, $\dot{x_1}(t)$, $\dot{x_2}(t)$, and $\dot{x_3}$, and they compare among Laplace, Morlet, and the Morse wavelets in addition to the STFT. All the lines are normalized, so the maximum value of each is 1.

The LWT skeleton lines show the most uniform decay that closely looks like an exponential decay. This agrees with the results in Equations (5.15) and (5.16). The closest lines to

the LWT skeleton lines are the STFT lines. Each LWT skeleton line carries a single major frequency. The oscillation frequencies, carried by the LWT skeleton lines in Figure 5.23(a), (b), and (c) are 1.6 Hz, 11.6 Hz and 31 Hz respectively, which is predicted by Equation (5.15). This is not the case with the other wavelets and the STFT. The STFT skeleton is almost not oscillating and cut from both ends, so it does not reveal the behavior at the beginning and end of the signal. The Morse wavelet skeleton is not uniform and the least regular in shape. In addition, the oscillatory frequency of the Morlet wavelet is different from the peak frequency at which the Morlet wavelet attains its maximum in the frequency domain. The difference grows as the oscillatory frequency increase. In this example, the Morlet wavelet skeletons carry scaled frequencies by an approximate factor of 1/5. If the sinusoid in Equation (5.13) has a frequency of ω, then the Morlet wavelet filter is centered at frequency $\omega_{peak} \approx \omega/5$ in the frequency domain. Moreover, the decay shape significantly deviates from the exponential decay at many instances.

The previous analysis shows that the response signal of the LTI-MDOF system can be decomposed using the LWT into N components, where N is equal to the number of DOF. Moreover, each component carries the property of a single mode of the response modes.

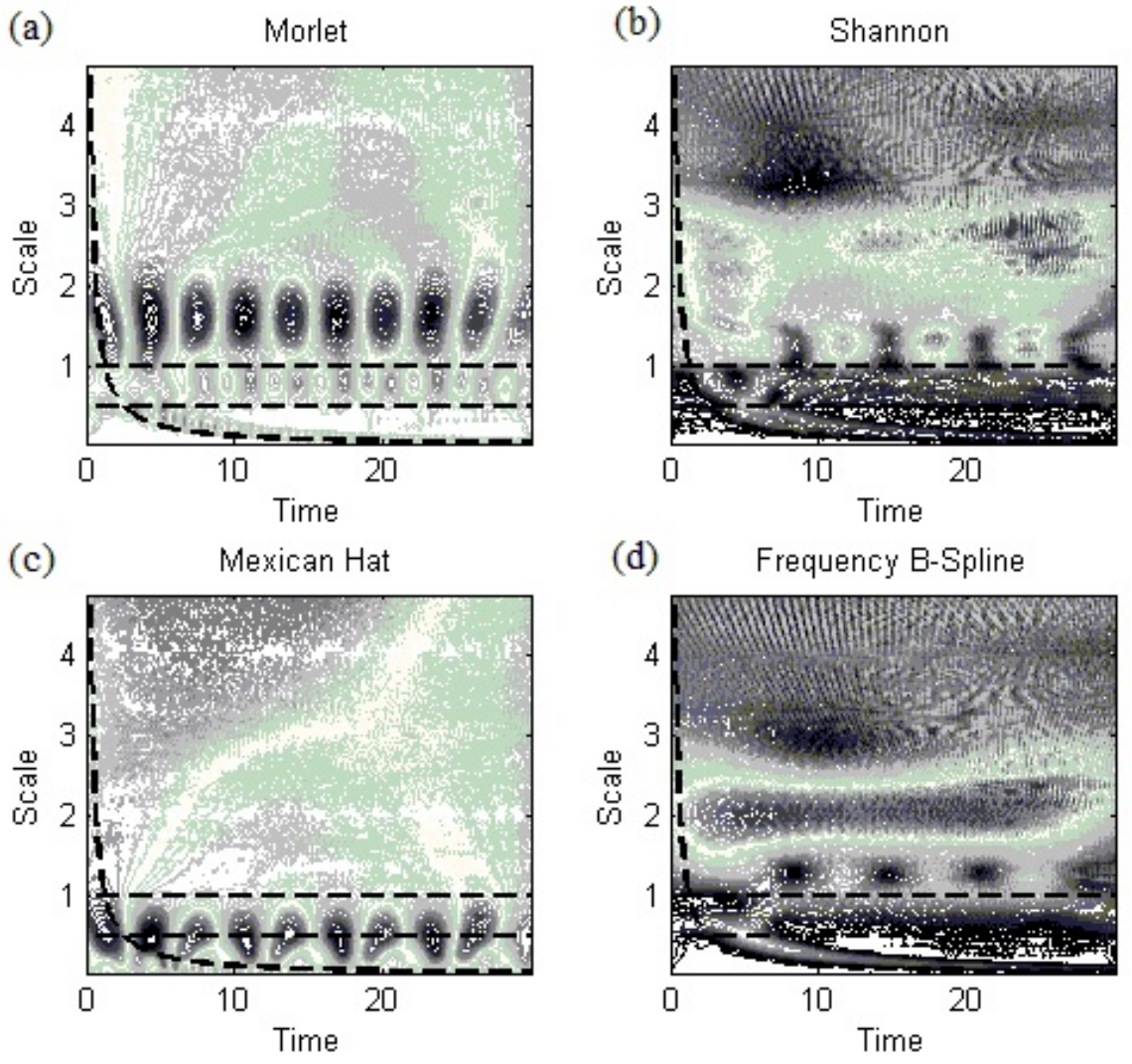

Figure 5.8: Scalograms of the signal described by Equation (5.10) using different wavelets. (a) by Morlet wavelet (b) by Complex Shannon wavelet ($f_b = 1$, $f_c = 1$) (c) by Mexican hat wavelet (d) by Frequency B-Spline wavelet (order=2, $f_b = 1$, $f_c = 1$). f_b: bandwidth frequency. f_c: wavelet center frequency

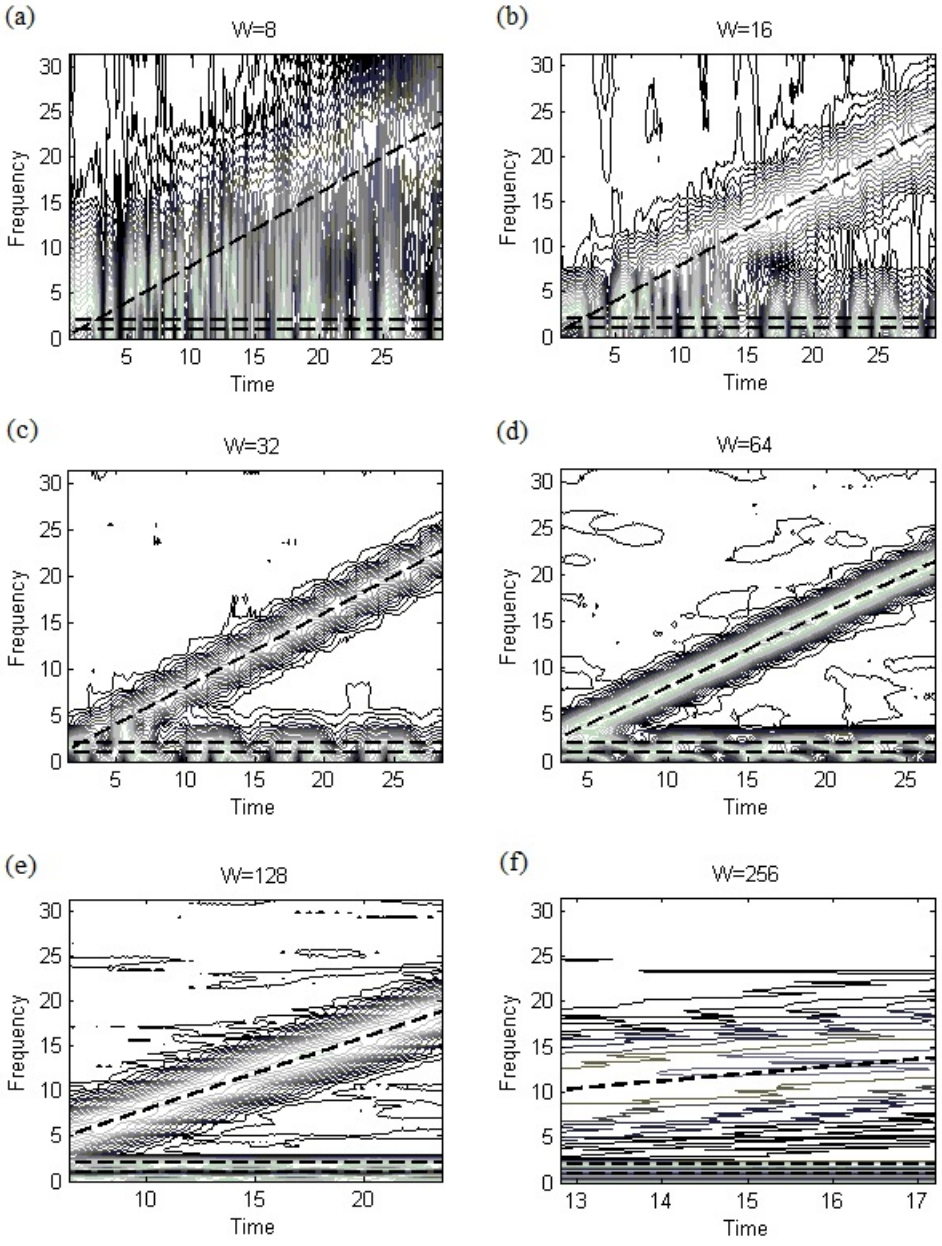

Figure 5.9: Spectrograms of the linear chirp signal in Equation (5.10) at different Window widths (samples). (a) $W = 8$ (b) $W = 16$ (c) $W = 32$ (d) $W = 64$ (e) $W = 128$ (f) $W = 256$.

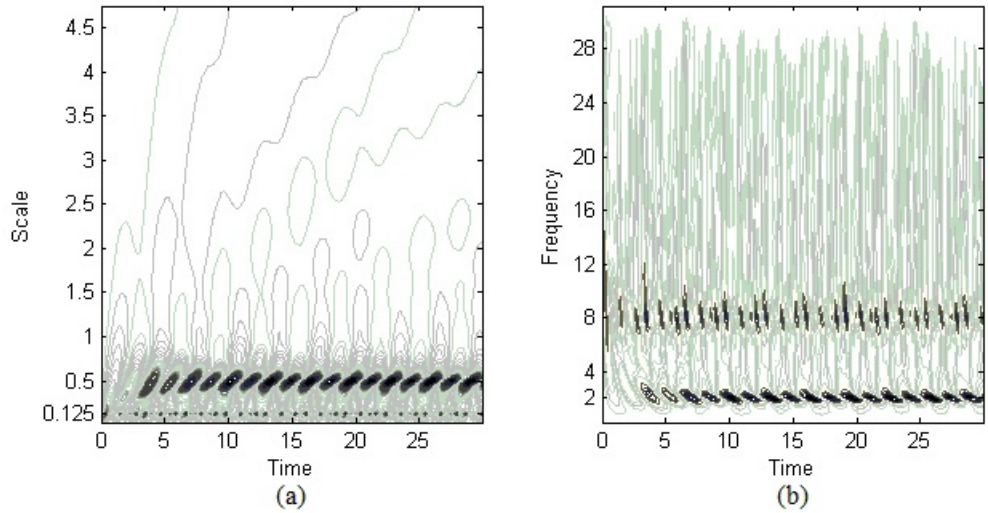

Figure 5.10: Reverse wavelet transform of the signal in Figure 5.3. (a)Scalogram, time-scale contour. (b) Spectrogram, time-frequency contour mapping.

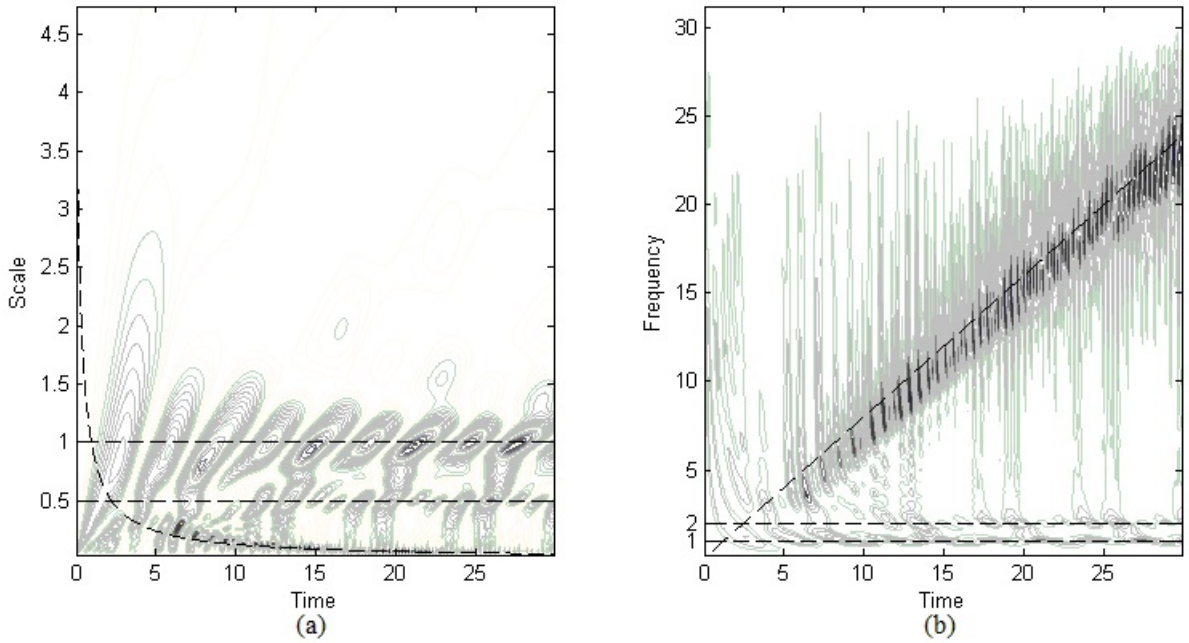

Figure 5.11: Reverse wavelet transform of the signal in Figure 5.5. (a) Scalogram, time-scale contour mapping. (b) Spectrogram, Time-frequency contour mapping.

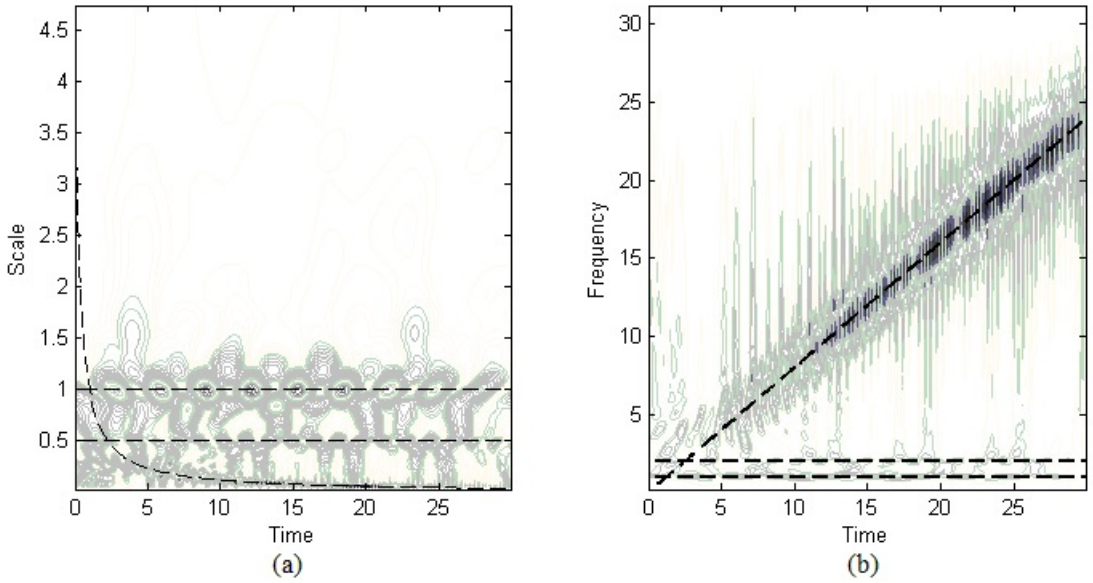

Figure 5.12: Average of FWT and RWT of the linear chirp in Figure 5.5. (a) Scalogram, time-scale contour mapping. (b) Spectrogram, time-frequency contour mapping.

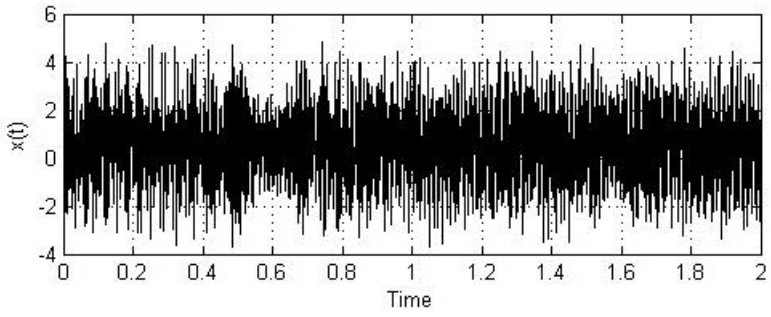

Figure 5.13: Quadratic chirp and two constant harmonics and white noise at SNR=15dB.

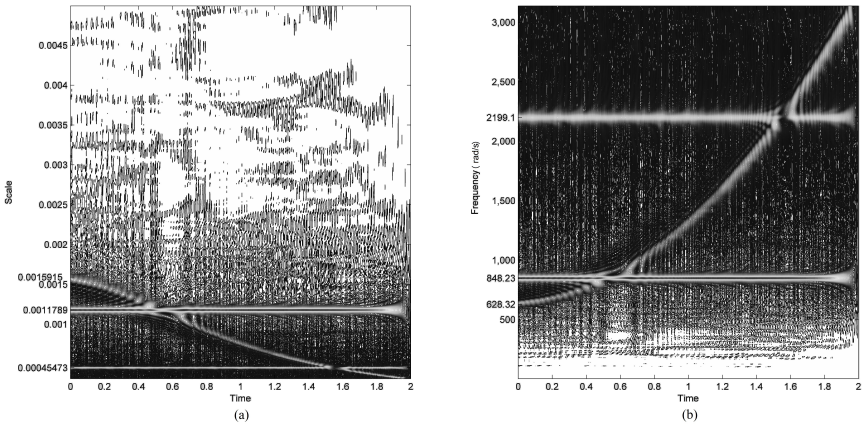

Figure 5.14: Laplace Wavelet Transform of $S(t)$ in Equation (5.11). (a) Time-scale contour (scalogram) (b) Time-frequency contour (spectrogram).

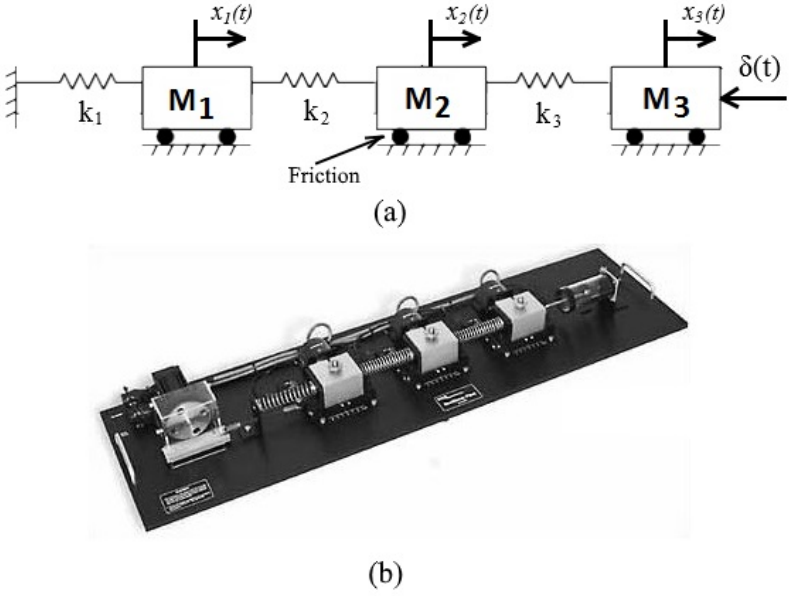

Figure 5.15: (a) schematic of 3 DOF Mass-spring system with friction (b) The testing bench used in experiments.

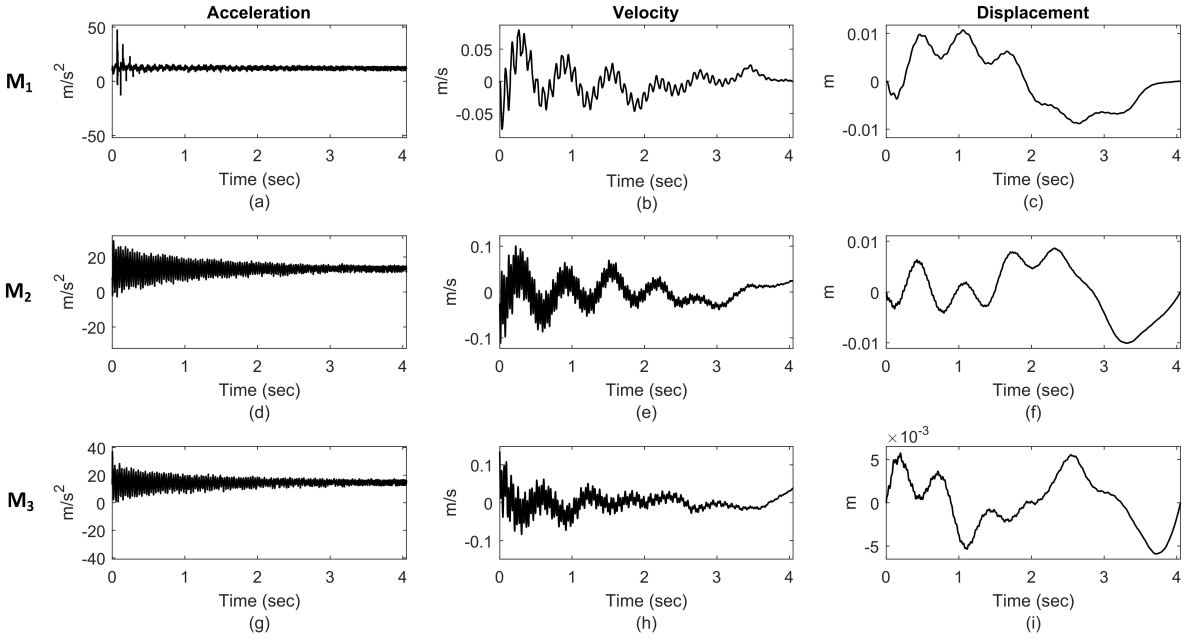

Figure 5.16: The response acceleration (left column), velocity (center column), and displacement (right column) for mass M_1 (top row), M_2 (middle row), and M_3 (bottom row).

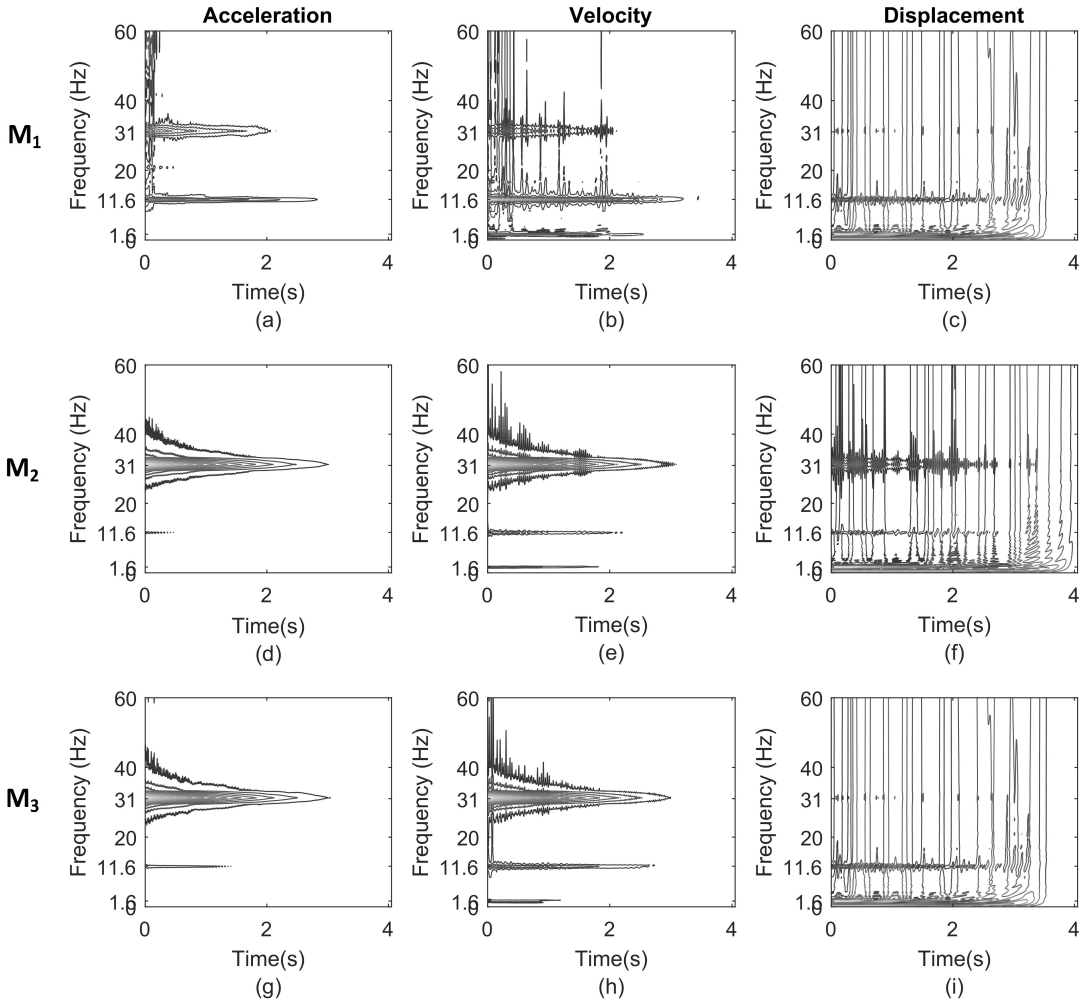

Figure 5.17: Spectrogram contour of the LWT, with $\zeta = 0.01$, of acceleration (left column), velocity (center column), and displacement (right column), and of M_1 (top row), M_2 (middle row), and M_3 (bottom row). The contour is plotted at 15 contour lines.

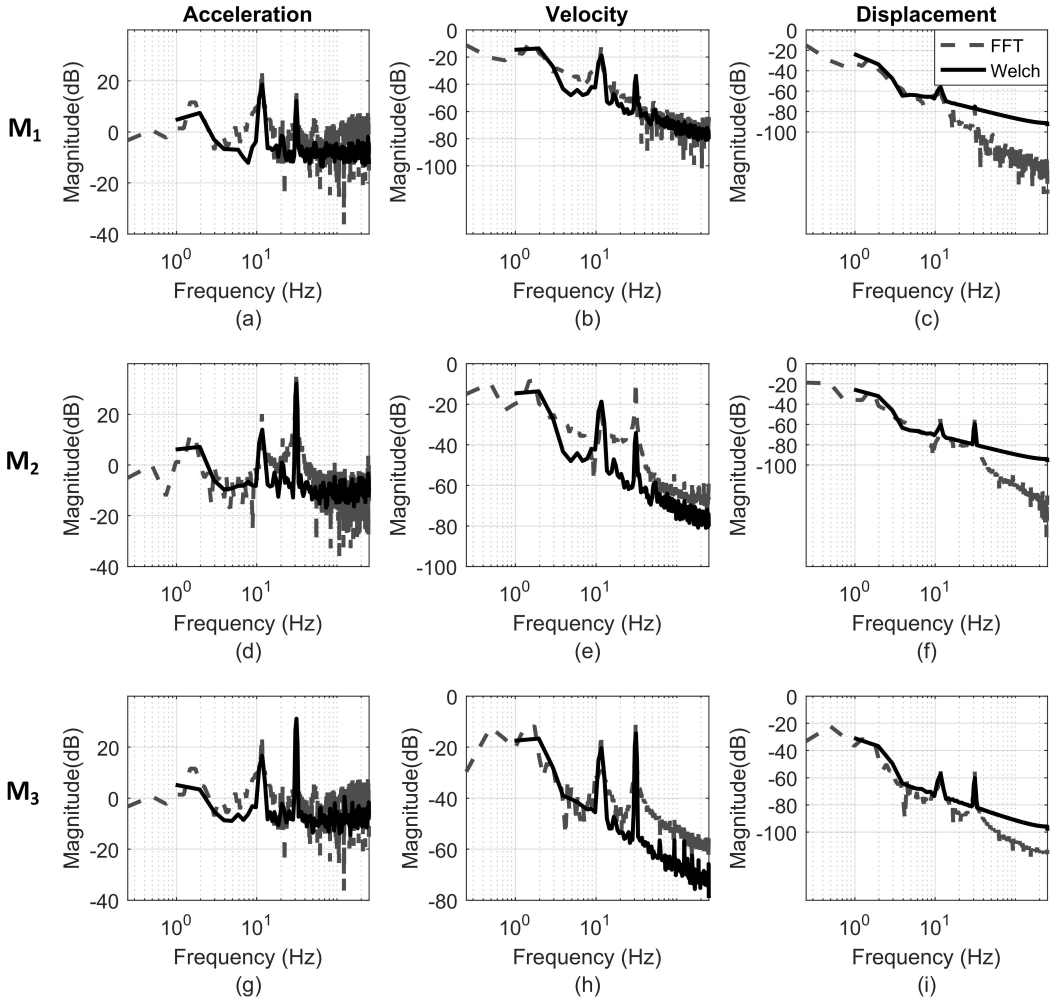

Figure 5.18: Spectrum on semi-log scale of the acceleration (left column), velocity (middle column), and displacement (right column) for M_1 (top row), M_2 (middle row), and M_3 (bottom row).

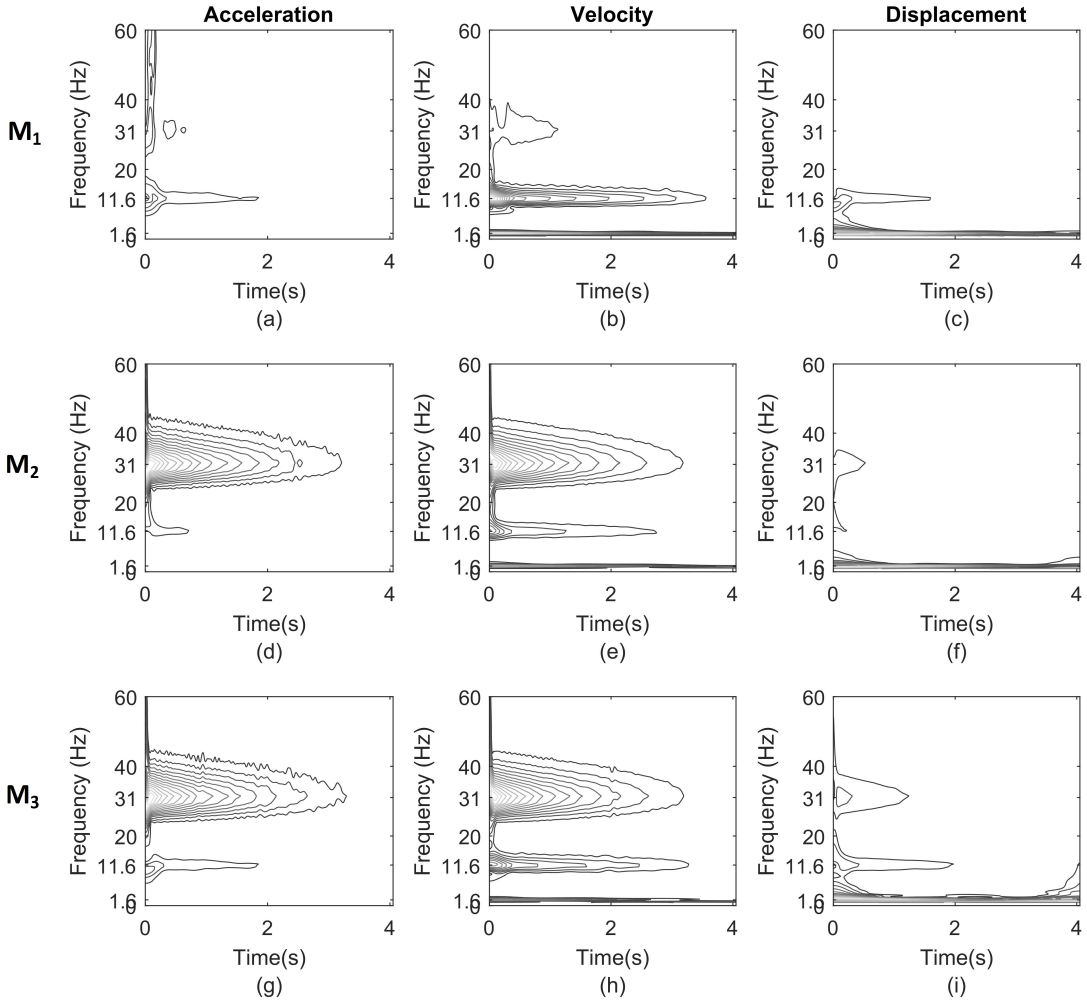

Figure 5.19: Spectrogram contour of the Morse wavelet transform of acceleration (left column), velocity (center column), and displacement (right column), for M_1 (top row), M_2 (middle row), and M_3 (bottom row). The contour is plotted with 15 contour lines.

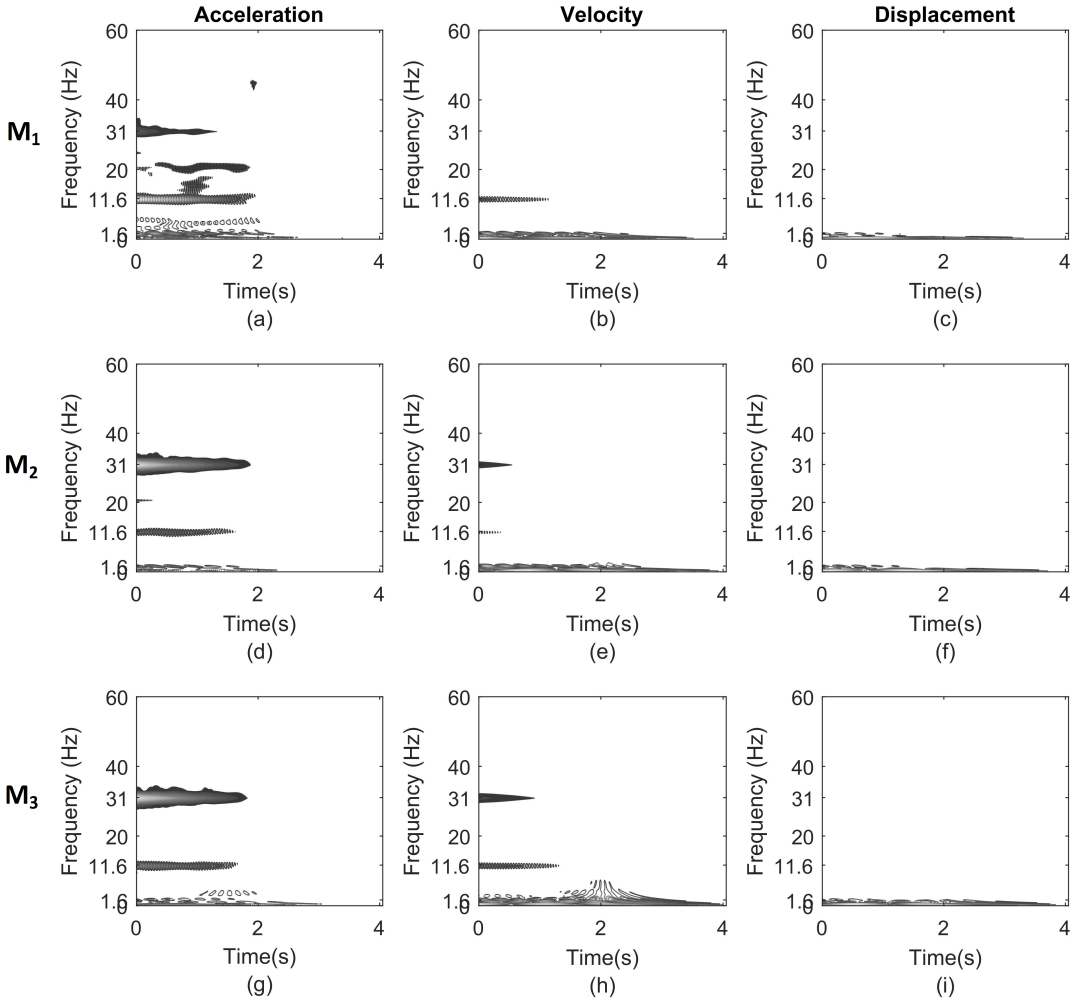

Figure 5.20: Spectrogram contour of the Morlet wavelet transform of acceleration (left column), velocity (center column), and displacement (right column), for M_1 (top row), M_2 (middle row), and M_3 (bottom row). The contour is plotted at 15 contour lines.

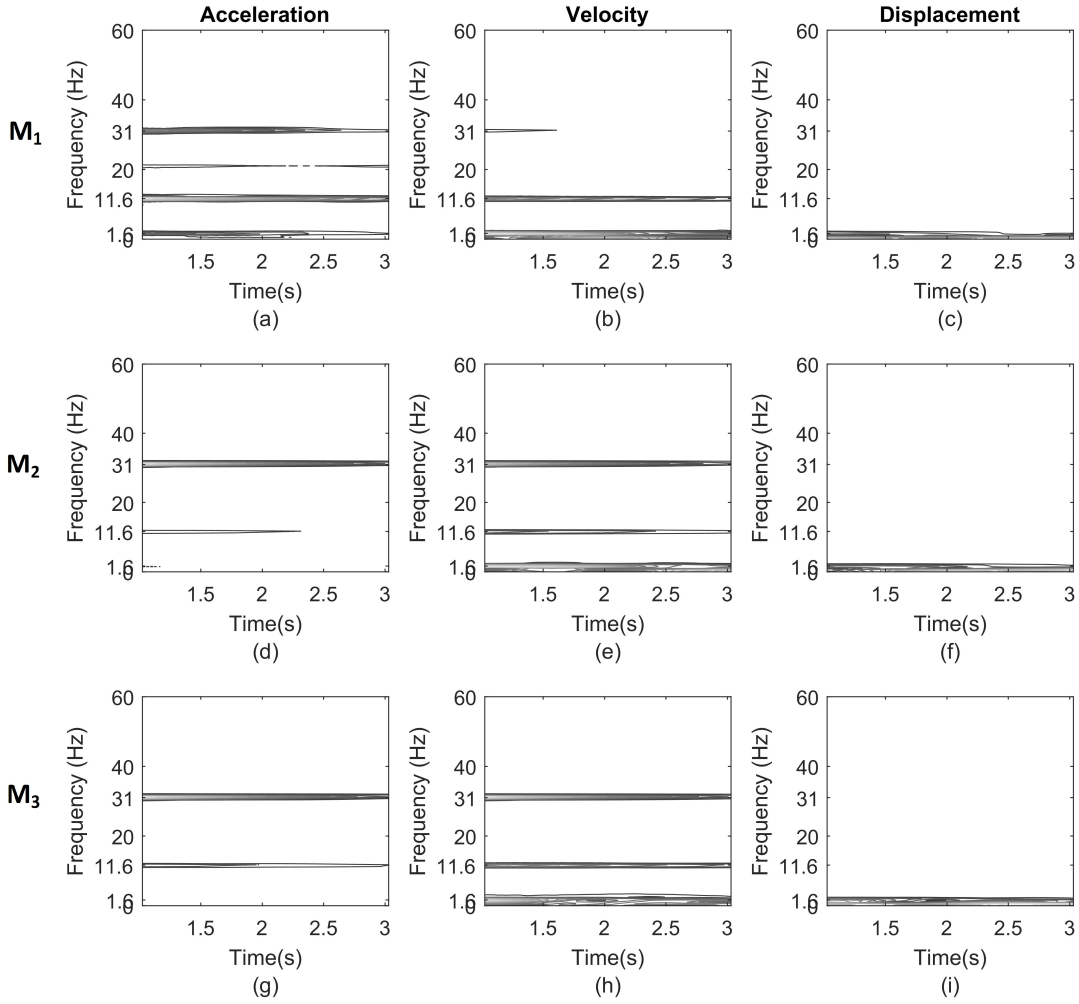

Figure 5.21: Spectrograms contours of the STFT of acceleration (left column), velocity (center column), and displacement (right column), for M_1 (top row), M_2 (middle row), and M_3 (bottom row). The contour is plotted at 15 contour lines.

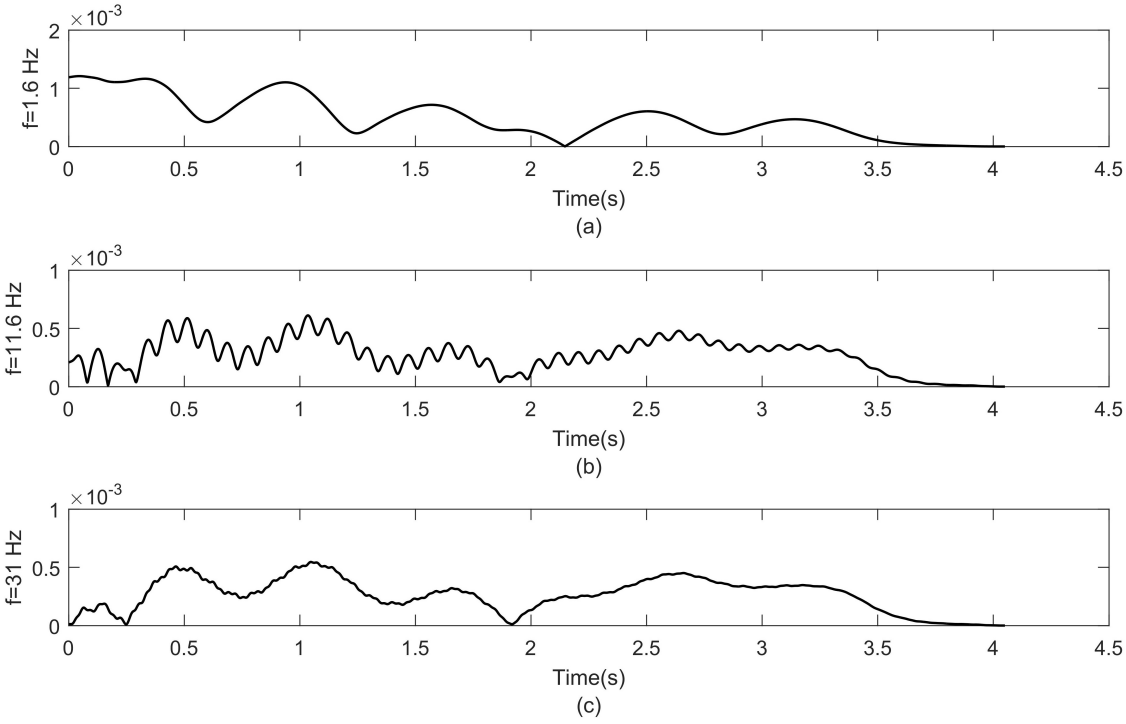

Figure 5.22: LWT Mode decomposition of $x_1(t)$. Skeleton lines at the modal ridges from mass M_1 displacement spectrograms shown in Figures 5.17 and 5.19 to 5.21.

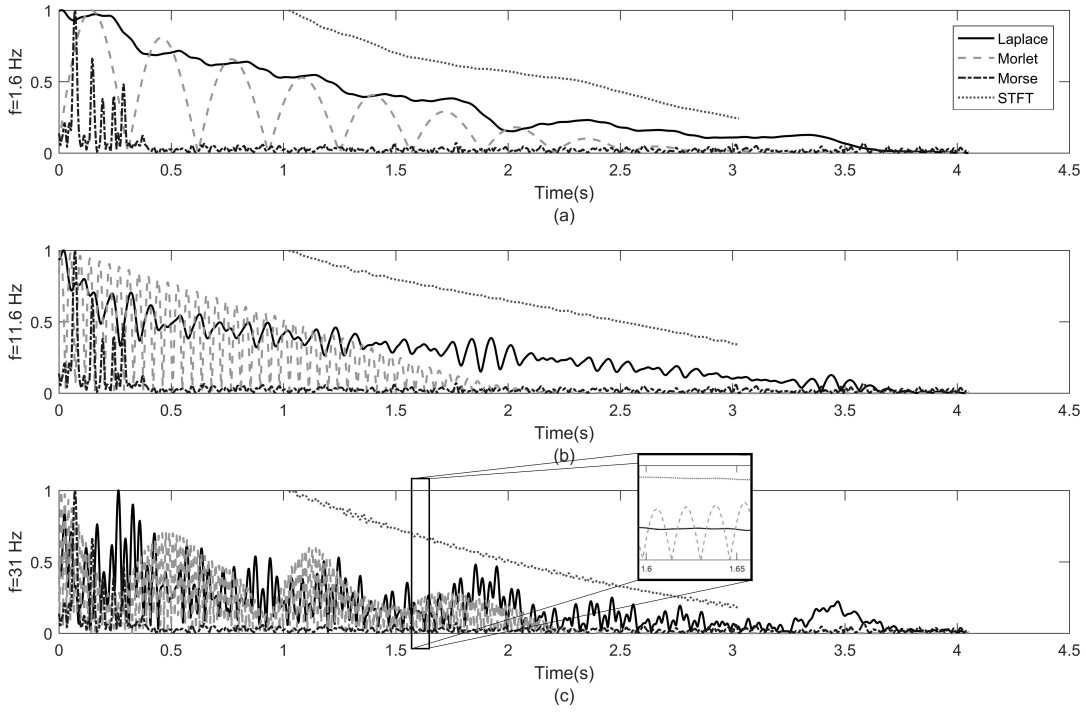

Figure 5.23: Skeleton lines at the modal ridges from the velocity spectrograms of mass M_1 shown in Figures 5.17 and 5.19 to 5.21. (a) 1.6 Hz skeleton; (b) 11.6 Hz skeleton; (c) 31 Hz skeleton.

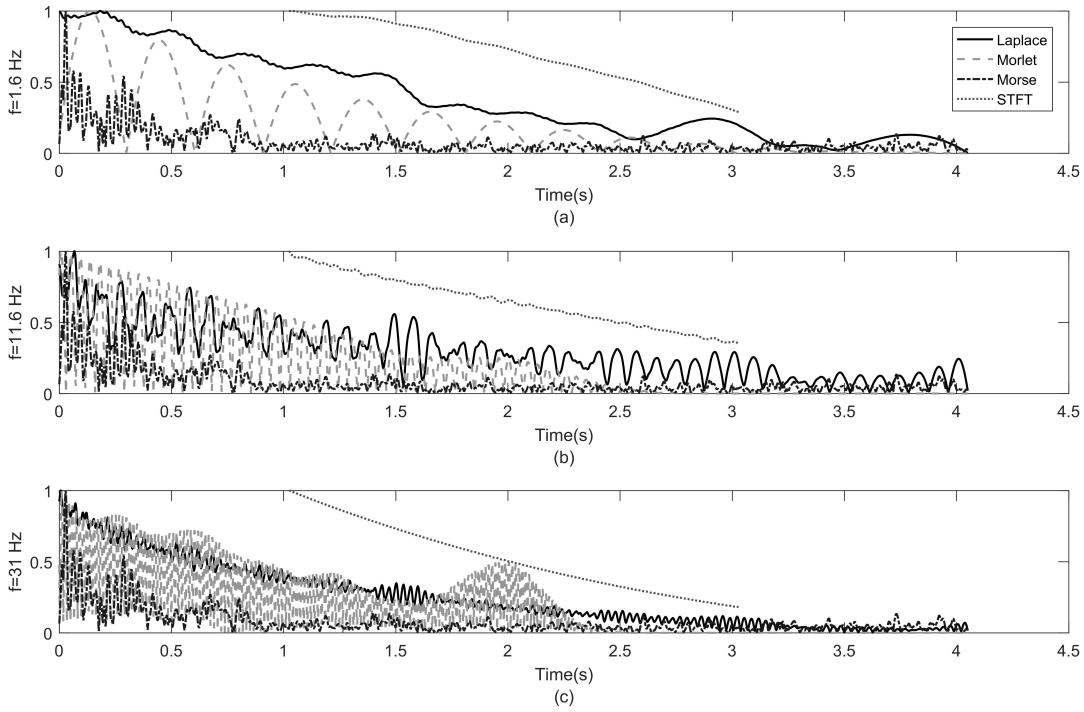

Figure 5.24: Skeleton lines at the modal ridges of mass M_2 velocity spectrograms shown in Figures 5.17 and 5.19 to 5.21. (a) 1.6 Hz skeleton; (b) 11.6 Hz skeleton; (c) 31 Hz skeleton, notice the enlarged section.

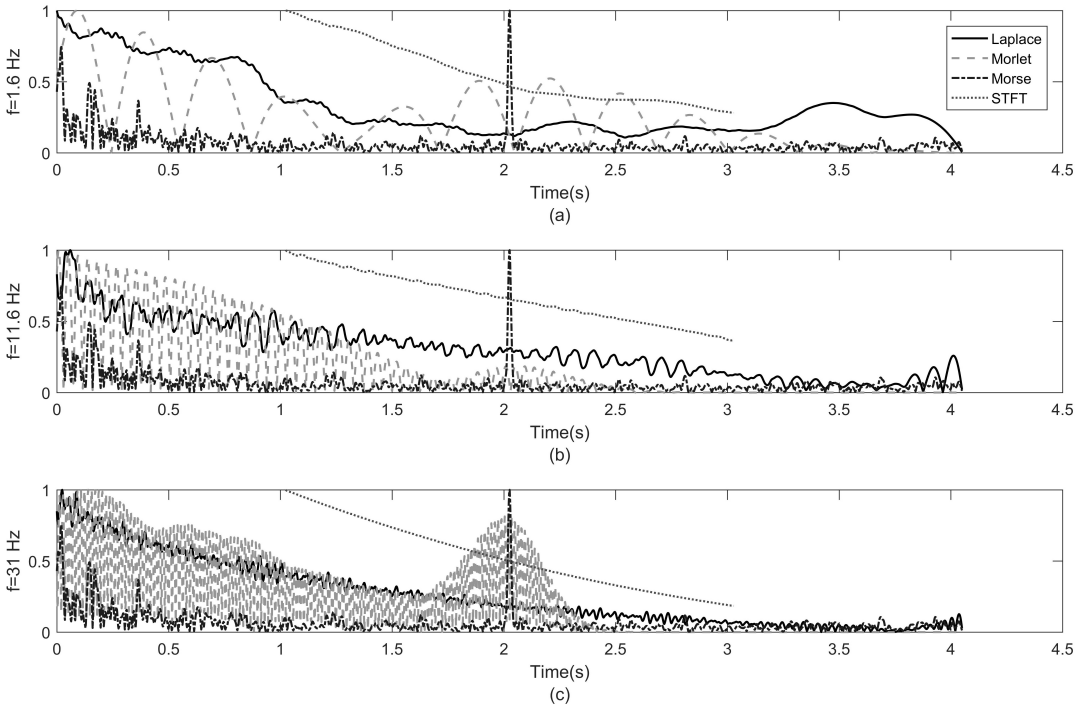

Figure 5.25: Skeleton lines at the modal ridges of mass M_3 velocity spectrograms shown in Figures 5.17 and 5.19 to 5.21. (a) 1.6 Hz skeleton; (b) 11.6 Hz skeleton; (c) 31 Hz skeleton.

Chapter 6

Modal Parameters Identification

Control of mechanical and civil structures requires accurate modeling. The more accurate the model, the easier the job of the control engineer will be. Furthermore, accurate modeling leads to better performance and control that is more reliable. In addition, accurate models simplify the needed control strategy, and this reduces the complexity and the cost of the control system. Therefore, system identification became an essential step in many practical control problems, and the field is expanding in theory, practice, and technology. One of the recent mathematical tools that showed potential for system identification is wavelets.

The major advantage of the Laplace wavelets over the Short Time Fourier Transform (STFT) is the analytically evaluated transform formulas of the LWT. Using the SOULTI or the Laplace wavelets enables accurate estimation of the peak frequency deviation from the input signal frequency. These wavelet transforms offer closed-form formulas for any cross section in the wavelet transform spectrogram, which enables linking the time-frequency transformation of the signal to the signal's features. Moreover, the accuracy and quality of the STFT depends on the width of the analysis window, which is fixed and chosen prior to the start of the analysis. Choosing the appropriate window width for the STFT requires many iterations, and sometimes the process is very difficult, especially for high rate signals. Because the STFT window is fixed in width, the time resolution is compromised at high frequency sections of the signal especially if the signal is of wide spectrum.

Moreover, the methodologies presented are more accurate than the Morlet-based and other wavelets-based methods because the LWT can be directly used in the analysis without approximations. Evaluating the ridges and skeletons in the time-frequency domain using the Morlet wavelet for the mode $x_k(t)$ is based on the approximation [66]

$$\tilde{x}_{k_{a,\tau}} \approx A(\tau)\ e^{-\xi\omega_n\tau} G^*(\pm aj\omega_n\sqrt{1-\xi^2}\tau). \tag{6.1}$$

where a is the time shift variable, τ the scale variable, ω_n the natural frequency, and ξ the damping ratio. A similar but an exact equation can be obtained for the wavelet transformation of mode $x_k(t)$ but using the Laplace or the SOULTI wavelet as will be shown in

the following analysis. This yields a more accurate result for modal parameters estimation. When approximation is used for some methods in the following analysis, we show that its accuracy and a way to measure the accuracy. On the other hand, some of the presented methods use exact relations without any approximation.

6.1 Modal Decomposition

Before describing the modal decomposition, it is relevant first to present a concise description of the modeling and the response of MDOF LTI systems.

The generic 2nd order differential equation of motion for a MDOF Linear Time-Invariant (LTI) vibratory system, with Degree of Freedom (DOF)=n, under impulse input is given by

$$\mathbf{M}\ddot{\mathbf{x}} + \mathbf{C}\dot{\mathbf{x}} + \mathbf{K}\mathbf{x} = \mathbf{G}\delta(t) \tag{6.2}$$

where $\mathbf{M}$ is the inertia matrix, $\mathbf{C}$ the damping matrix, $\mathbf{K}$ the stiffness matrix, $\mathbf{G}$ the input matrix, and $\mathbf{x}$ the displacement vector. The general solution of Equation (6.2) can be found by converting it to a system of first order differential equations. Equation (6.2) can be rewritten as

$$\dot{\mathbf{X}} = \mathbf{A}\mathbf{X} + \mathbf{B}\delta(t) \tag{6.3}$$

where $\mathbf{A}$ and $\mathbf{B}$ are given by

$$\mathbf{A} = \begin{pmatrix} \mathbf{0} & \mathbf{I} \\ -\mathbf{M}^{-1}\mathbf{K} & -\mathbf{M}^{-1}\mathbf{C} \end{pmatrix}, \ \mathbf{B} = \begin{pmatrix} \mathbf{0} \\ \mathbf{G} \end{pmatrix} \tag{6.4}$$

and the state vector, $\mathbf{X}$, is given by

$$\mathbf{X}(t) = \begin{pmatrix} \mathbf{x}(t) \\ \dot{\mathbf{x}}(t) \end{pmatrix} = \begin{pmatrix} x_1(t) \\ \vdots \\ x_n(t) \\ \dot{x_1}(t) \\ \vdots \\ \dot{x_n}(t) \end{pmatrix} \tag{6.5}$$

An output equation can be added to model the measurement of the system states as

$$\mathbf{Y}(t) = \mathbf{C}\mathbf{X}(t) \tag{6.6}$$

The solution of equation 6.3 is given by

$$\mathbf{X}(t) = \sum_{k=1}^{n} 2c_k e^{\xi_k \omega_k t} \left(Re(\mathbf{q}^{(k)}) \sin\left(\omega_k \sqrt{1-\xi_k^2}t\right) + Im(\mathbf{q}^{(k)}) \cos\left(\omega_k \sqrt{1-\xi_k^2}t\right)\right) \tag{6.7}$$

where $\mathbf{q}^{(k)} = (q_{k1}\ q_{k2}\ \dots\ q_{kn})^T$ is kth eigenvector of $\mathbf{A}$, ω_k the modal frequency of the kth mode, and ξ_k the modal damping of the kth mode. If the LWT is applied to the measured output $y_i(t) = x_i(t)$, the transformed signal, $\tilde{y}_{iL\zeta}(\tau, a)$, in the time-scale domain reads

$$\tilde{y}_{iL\zeta}(\tau, a) = \sum_{k=1}^{n} R_{ik}(a, \zeta, \omega_k, \xi_k) e^{\xi_k \omega_k \tau} \sin(\omega_k \sqrt{1-\xi_k^2}\tau + \theta_k) \tag{6.8}$$

From Tables 3.1 and 4.1, the phase angle θ is given by

$$\theta = \tan^{-1}\left(\frac{\sigma_0 + (\xi_k - \omega_k)a}{\sigma_0 + (\xi_k + \omega_k)a}\right) \tag{6.9}$$

and $R_{ik}(a, \zeta, \omega_k, \xi_k)$ is given by

$$R_{ik}(a, \zeta, \omega_k, \xi_k) = \frac{\sqrt{\left(Re(q_{ki})\left(\sigma_0 + (\xi_k + \omega_k)a\right)\right)^2 + \left(Im(q_{ki})\left(\sigma_0 + (\xi_k - \omega_k)a\right)\right)^2}}{a^2\omega_k^2 + (\sigma_0 + a\xi_k)^2} \tag{6.10}$$

In modal decomposition, the interest is to separate the each modal frequency from the system's output. Therefore, we have to insure that the wavelet transform acts as a filter that separates the frequencies of interest. The question becomes, at what input frequency ω the amplitude of the Wavelet transform attains its peak. This will be shown for the Laplace wavelets. However, the same procedure can be followed for the SOULTI wavelets. Note that the SOULTI and Laplace wavelets are not symmetric, so the wavelet transform in this case is not equivalent to the convolution integral. The amplitude $R_{ik}(a, \zeta, \omega_k, \xi_k)$ is complex. Finding its magnitude, then differentiating it with respect to ω produces high order polynomial whose roots are very difficult to find analytically. Therefore, the answer is sought through analysis in the frequency domain.

The following analysis relies on the result of Theorems 3.3 and 4.2, which show that the Laplace and the SOULTI wavelet transforms resemble the particular solution or the particular response of LTI systems.

The relationship between the SOULTI and Laplace wavelets and the Equations (3.18) and (4.20) respectively is established in the frequency domain. The frequency response function (FRF) of the system described by equation 3.18 is the complex conjugate of the Laplace wavelet in the frequency domain as shown in Theorem 4.1. Therefore, if the FRF of Equation (4.2) is $\Phi_{L\zeta}(\omega)$ then it is related to the Fourier transform of the Laplace wavelet $\Psi_{L\zeta}(\omega)$ by

$$\Phi_{L\zeta}(\omega) = \overline{\Psi_{L\zeta}(\omega)} = \frac{a^{1-p}}{1-\zeta^2} \frac{1}{-j\omega + \left(\frac{\zeta}{\sqrt{1-\zeta^2}} + j\right)} \tag{6.11}$$

A similar relation applies to the SOULTI wavelets. We conclude from Theorems 3.3 and 4.2 that the wavelet transform with respect to the Laplace and SOULTI wavelets can be

represented as the output of a linear system or linear IIF filter, where the filters are described by Equations (3.18) and (4.20), see the block diagram in Figure 6.1. However, the wavelet transform only produces part of the general system response, namely the particular response. This property is useful in modal signal decomposition, since the response due to the filter natural characteristics is not desired and considered noise.

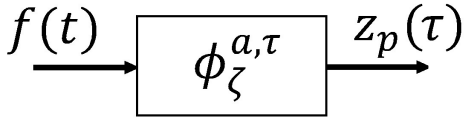

Figure 6.1: Block diagram representing the Laplace and SOULTI wavelets transform as the output of linear time-invariant system.

From the theory of linear dynamic systems, we find that if the impulse response of a system is given by

$$h(t) = c_1 e^{\sigma t} \tag{6.12}$$

then the response to generic initial conditions, $y(0) = y_0$, and forcing input, $f(t)$ is given by

$$\begin{aligned} z(t) &= \underbrace{e^{\sigma t} z_0}_{} + \underbrace{\int_0^t e^{\sigma(t-\tau)} f(\tau) d\tau}_{} \\ &= z_i \quad + \quad \overbrace{z_{nat} + z_p}^{} \end{aligned} \tag{6.13}$$

where z_i is the response due to initial conditions, z_{nat} the natural response due to input, and z_p the particular response of the input. In the following analysis, we will use the LWT, but the same can be applied using the SOULTI wavelet.

Let $\phi_{L\zeta}(t)$ be defined by

$$\phi_{L\zeta}(t) = \mathcal{F}^{-1}\{\Phi_{L\zeta}(\omega)\} \tag{6.14}$$

then the scaled and shifted version of $\phi_{L\zeta}(t)$ is denoted by $\phi_{L\zeta}^{\tau,a}(t)$. If the wavelet transform is applied to the measured output $y_i(t) = x_i(t)$ of the system in Equation (6.3), then this is equivalent to feeding $y_i(t)$ through the LTI filter $\phi_{L\zeta}^{a,\tau}$ and obtaining the particular solution. The general form of the response of an LTI system to some input is given in the Laplace domain by

$$Z(s) = H(s)F(s) \tag{6.15}$$

where $H(s)$ is the system's transfer function, and $F(s)$ is the input function in the frequency domain. Let us consider the interaction between the filter $\Phi_{L\zeta}(as)$ and the kth mode of the MDOF system described by Equation (6.3), so in Equation (6.15), make $H(s) = \Phi_{L\zeta}(as)$ and $F(s) = \mathcal{L}\{x_{ki}(t)\} = X_{ki}(s)$, $k, i = 1, 2, \ldots, n$. $x_{ki}(t)$ represents the kth mode response of the ith degree of freedom. In general, $X_{ki}(s)$ can be expanded in partial fraction as

$$X_{ki}(s) = \frac{c_1 s + c_2 \xi_k \omega_k}{s^2 + \xi_k \omega_k s + \omega_k^2} = \frac{c_1 s + c_2 \xi_k \omega_k}{(s - s_1)(s - s_2)} \tag{6.16}$$

where $c_1 = 2Im\,(q_{ki})$ and $c_2 = 2Re\,(q_{ki})$, and the roots s_1 and s_2 are given by

$$\begin{aligned} s_1 &= \left(\frac{-\xi_k}{\sqrt{1-\xi_k^2}} - j \right) \omega_{dk} \\ s_2 &= \left(\frac{-\xi_k}{\sqrt{1-\xi_k^2}} + j \right) \omega_{dk} \end{aligned} \tag{6.17}$$

where ω_{dk} is the damped oscillating frequency defined as $\omega_{dk} = \omega_k \sqrt{1-\xi_k^2}$. Now, the output $Z_{ki}(s)$ in Equation (6.15) can be expressed as

$$Z_{ki}(s) = \frac{K_1}{s-s_1} + \frac{K_2}{s-s_2} + [partial \;\; fraction\,(\Phi_{L\zeta}(a\,s))] \tag{6.18}$$

where the particular solution part of $Z_{ki}(s)$ is

$$Z_{ki_p}(s) = \frac{K_1}{s-s_1} + \frac{K_2}{s-s_2} \tag{6.19}$$

K_1 and K_2 are given by

$$\begin{aligned} K_1 &= w_{1_{ki}} \Phi_{L\zeta}(as_1) \\ K_2 &= w_{2_{ki}} \Phi_{L\zeta}(as_2) \end{aligned} \tag{6.20}$$

where $w_{1_{ki}} = \overline{w_{2_{ki}}}$, and both are given by

$$\begin{aligned} w_{1_{ki}} &= \frac{c_1 s_1 + c_2 \xi_k \omega_k}{s_1 - s_2} = \frac{c_1\sqrt{1-\xi_k^2} + j(-c_1+c_2)\xi_k}{2\sqrt{1-\xi_k^2}} \\ w_{2_{ki}} &= \frac{c_1 s_2 + c_2 \xi_k \omega_k}{s_2 - s_1} = \frac{c_1\sqrt{1-\xi_k^2} - j(-c_1+c_2)\xi_k}{2\sqrt{1-\xi_k^2}} \end{aligned} \tag{6.21}$$

and by substituting s_1 and s_2 from Equation (6.17) into Equation (6.11) gives $\Phi_{L\zeta}(as_1)$ and $\Phi_{L\zeta}(as_2)$ as

$$\begin{aligned} \Phi_{L\zeta}(as_1) &= \frac{a^{1-p}}{1-\zeta^2} \frac{1}{j(1+a\omega_{dk}) + \left(\frac{\zeta}{\sqrt{1-\zeta^2}} - \frac{a\xi_k\omega_{dk}}{\sqrt{1-\xi_k^2}} \right)} \\ \Phi_{L\zeta}(as_2) &= \frac{a^{1-p}}{1-\zeta^2} \frac{1}{j(1-a\omega_{dk}) + \left(\frac{\zeta}{\sqrt{1-\zeta^2}} - \frac{a\xi_k\omega_{dk}}{\sqrt{1-\xi_k^2}} \right)} \end{aligned} \tag{6.22}$$

Since $w_{1_{ki}}$ and $w_{2_{ki}}$ are only functions of ξ_k and q_{ki}, then the only part in Equation (6.20) that depends on a and ω_{dk} is $\Phi_{L\zeta}(as_i)$, $i = 1, 2$. Therefore, to find the scale that maximizes the amplitude of the Laplace wavelet filter, differentiate the norms of $\Phi_{L\zeta}(as_1)$ and $\Phi_{L\zeta}(as_2)$

with respect to a and set the derivatives to zero. To simplify the analysis, we use $p = 1$ and differentiate $|\Phi_{L\zeta}(as_i)|^2$, $i = 1, 2$, so the derivatives read

$$\begin{aligned}
&\frac{d|\Phi_{L\zeta}(as_1)|^2}{da} = \\
&-\frac{1}{1-\zeta^2}\frac{2(1+a\omega_{dk})\omega_{dk} - 2\left(\frac{\zeta}{\sqrt{1-\zeta^2}} - \frac{a\xi_k\omega_{dk}}{\sqrt{1-\xi_k^2}}\right)\frac{\omega_{dk}\xi_k}{\sqrt{1-\xi_k^2}}}{\left((1+a\omega_{dk})^2 + \left(\frac{\zeta}{\sqrt{1-\zeta^2}} - \frac{a\xi_k\omega_{dk}}{\sqrt{1-\xi_k^2}}\right)^2\right)^2} \\
&\frac{d|\Phi_{L\zeta}(as_2)|^2}{da} = \\
&-\frac{1}{1-\zeta^2}\frac{2(1-a\omega_{dk})\omega_{dk} - 2\left(\frac{\zeta}{\sqrt{1-\zeta^2}} - \frac{a\xi_k\omega_{dk}}{\sqrt{1-\xi_k^2}}\right)\frac{\omega_{dk}\xi_k}{\sqrt{1-\xi_k^2}}}{\left((1-a\omega_{dk})^2 + \left(\frac{\zeta}{\sqrt{1-\zeta^2}} - \frac{a\xi_k\omega_{dk}}{\sqrt{1-\xi_k^2}}\right)^2\right)^2}
\end{aligned} \tag{6.23}$$

setting the derivatives in Equation (6.23) to zero and solving for a yields the maximizing scale values as

$$\begin{aligned}
a_{k1} &= \frac{-1}{\omega_{dk}}\frac{1 - \frac{\zeta\xi_k}{\sqrt{1-\zeta^2}\sqrt{1-\xi_k^2}}}{1 + \frac{\xi_k^2}{1-\xi_k^2}} \\
a_{k2} &= \frac{1}{\omega_{dk}}\frac{1 + \frac{\zeta\xi_k}{\sqrt{1-\zeta^2}\sqrt{1-\xi_k^2}}}{1 + \frac{\xi_k^2}{1-\xi_k^2}}
\end{aligned} \tag{6.24}$$

Notice that $a_{k_1} < 0$ for

$$\xi_k < \sqrt{1-\zeta^2}$$

In addition, when $\xi_k = 0$ Equation (6.24) shows that

$$\begin{aligned}
a_{k1} &= \frac{-1}{\omega_{dk}} \\
a_{k2} &= \frac{1}{\omega_{dk}}
\end{aligned} \tag{6.25}$$

regardless of the value of ζ. Moreover, if $\xi_k = \zeta$ then $a_{k2} = 1/\omega_{dk}$, but the magnitude of $\Phi_{L\zeta}(as_2)$ becomes infinite which means that the wavelet filter experiences a resonance. However, for a single harmonic we may either assume that the input frequency is positive or negative but not both. Without loss of generality, assume that $\omega_{dk} > 0$, then $\Phi_{L\zeta}(as_2)$ is the function that has a peak at $a = 1/\omega_{dk}$, while the magnitude of $\Phi_{L\zeta}(as_1)$ is smaller, see Figure 6.2. Consequently, the focus is given to a_{k2} and $\Phi_{L\zeta}(as_2)$.

Return to Equation (6.19) and evaluate the particular solution in the time domain. Substituting $w_{1_{ki}}$ and $w_{2_{ki}}$ from Equation (6.21) in Equation (6.20), substituting the result back into Equation (6.19) and taking the Laplace inverse transform yields

$$\begin{aligned} z_{ki_p}(t) = &|w_{1_{ki}}| e^{-\frac{\xi_k \omega_{dk}}{\sqrt{1-\xi_k^2}} t} \\ &[|\Phi_{L\zeta}(as_1)| \cos(\omega_{kd} t + \theta_1) + |\Phi_{L\zeta}(as_2)| \cos(\omega_{kd} t + \theta_2) + \\ &j(|\Phi_{L\zeta}(as_1)| \sin(\omega_{kd} t + \theta_1) + |\Phi_{L\zeta}(as_2)| \sin(\omega_{kd} t + \theta_2))] \end{aligned} \tag{6.26}$$

If $\Phi_{L\zeta}(as_2) \gg \Phi_{L\zeta}(as_1)$ then one can approximate with high accuracy the maximum value of $z_{k_{ip}}(t)$ to occur at a scale $a = a_{k2}$ given by Equation (6.25). Since the function $\Phi_{L\zeta}(as_2)$ is bell-shaped, then by pushing a_{k1} in the negative range, the magnitude of $\Phi_{L\zeta}(as_1)$ at positive values of ω especially at a_{k2} becomes smaller and dominated by $\Phi_{L\zeta}(as_2)$. Figure 6.2 shows $\Phi_{L\zeta}(as_1)$ and $\Phi_{L\zeta}(as_2)$ for positive input frequency ω_{dk}. The figure shows that the farther $\Phi_{L\zeta}(as_1)$ to the left the smaller is its effect on the magnitude at the peak scale a_{k2}. Moreover, Figure 6.2 shows that $\Phi_{L\zeta}(as_2) > \Phi_{L\zeta}(as_1)$ and this is always the case for positive input frequencies as confirmed by Equation (6.22).

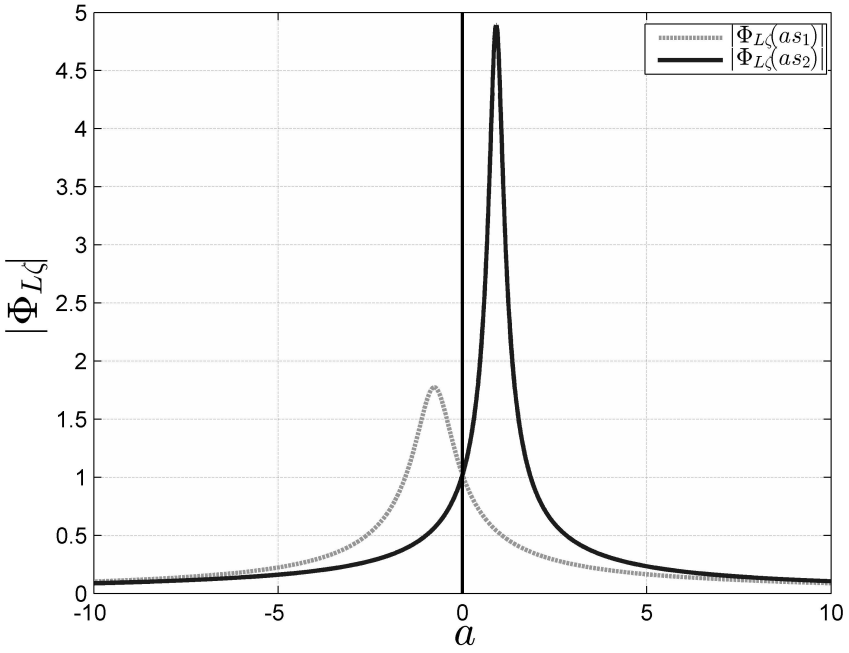

Figure 6.2: $|\Phi_{L\zeta}(as_1)|$ and $|\Phi_{L\zeta}(as_2)|$ versus scale for $\omega_{dk} = 1$, $\zeta = 0.2$, and $\xi = 0.4$.

Making ζ small guarantees that the peak of $\Phi_{L\zeta}(as_1)$ is in the negative range of frequencies for almost all the possible values of the input damping ξ_k. For example, if $\zeta = 0.2$, then $0 < \xi_k < 0.979$ makes $a_{k1} < 0$. Note that if $\omega_{dk} > 0$, then $a_{k2} > 0$ for all $0 < \xi_k < 1$. In these ranges, we have $|\Phi_{L\zeta}(as_2)| \gg |\Phi_{L\zeta}(as_1)|$, which means that $\Phi_{L\zeta}(as_2)$ is dominant.

Therefore, equation 6.26 can be approximated as

$$z_{ki_p}(t) \simeq |w_{1_{ki}}| e^{-\frac{\xi_k \omega_{dk}}{\sqrt{1-\xi_k^2}} t} \left[|\Phi_{L\zeta}(as_2)| \cos(\omega_{kd} t + \theta_2) + j \left(|\Phi_{L\zeta}(as_2)| \sin(\omega_{kd} t + \theta_2) \right) \right] \tag{6.27}$$

Then, the magnitude of $z_{ki_p}(t)$ can be approximated as

$$|z_{ki_p}(t)| \simeq |w_{1_{ki}}| e^{-\frac{\xi_k \omega_{dk}}{\sqrt{1-\xi_k^2}} t} |\Phi_{L\zeta}(as_2)| \tag{6.28}$$

If ω_{dk} is a modal frequency of the signal, then it is approximated with high accuracy by the scale a_k at which $z_{ki_p}(t)$ attains its maximum magnitude. This can be expressed as

$$\omega_{dk} \approx \frac{1}{a_{k2}} \approx \frac{1}{a_k} \tag{6.29}$$

6.2 Modal Parameters Identification

The previous section lays the foundation for different procedures to identify the damping and the frequency of a MDOF LTI system. In this section, we describe some techniques that can effectively be used to estimate the natural frequency and the damping ratio accurately.

6.2.1 Frequency estimation

The simplest and quickest method to estimate the oscillating frequency using the LWT relies on the LWT time-frequency separation of vibrations. From the LWT as shown in Table 4.1 and Equation (6.8), we find that the signal frequency is preserved through the transform and that the straight ridges are dominated by a single frequency.

Lightly damped systems

The first method is well suited for lightly damped systems, where $\xi_k \leq 0.3$. From the previous section we find that when the damping is light we can choose ζ to be small, $\zeta \leq 0.2$, then $\omega_{dk} \simeq 1/a$. Therefore, in a scalogram, the horizontal ridge-lines marked by the peak scales give direct estimate to the oscillating frequencies of the response through the relation

$$\omega_{dk} \simeq \frac{1}{a_k} \tag{6.30}$$

If the spectrogram is constructed using Equation (4.45), then the estimate of the oscillating frequencies is given by

$$\omega_{dk} \simeq \omega_k \tag{6.31}$$

Large or unknown damping range

If the damping is suspected to be in the mid to large range, $\xi_k > 0.3$, then a more accurate estimation than the estimation in section 6.2.1 is required.

When the damping is large, the peak scales or frequencies of the LWT are more skewed from the accurate estimation given by Equations (6.30) and (6.31). However, by examining the LWT of the response $y_i(t)$ shown in Equation (6.8), we find that the time evolving part of the LWT preserves the frequency content of the signal. In other words, the LWT cross sections around the peak scales carry a major single frequency, while the other modes' frequencies are attenuated. To retrieve that frequency, a simple FFT can be applied to the cross-section.

6.2.2 Damping ratio estimation

The estimation of the damping ratio in the following procedures follows the estimation of the oscillating frequencies from Section 6.2.1. In theory, the damping ratio can be estimated using Equation (6.24) at two different frequencies. First, pick any $0 < \zeta < 1$, which will be ζ_1 and perform the LWT with respect to $\psi_{L\zeta_1}$, then we choose a different wavelet family, $\psi_{L\zeta_2}$, where $\zeta_2 \neq \zeta_1$ and perform the LWT. For each modal frequency, obtain a ridge whose maximum is centered at a certain scale. Let the center scale obtained using ζ_1 and ζ_2 be $a_{k\zeta_1}$ and $a_{k\zeta_2}$ respectively. Now, take the ratio between $a_{k\zeta_1}$ and $a_{k\zeta_2}$ from Equation (6.24) and solve for ξ_k to get

$$\xi_k = \frac{|a_{k\zeta_1} - a_{k\zeta_2}|(1-\zeta_1^2)}{\sqrt{\left(a_{k\zeta_2}\zeta_1 - \frac{a_{k\zeta_1}\zeta_2\sqrt{1-\zeta_1^2}}{\sqrt{1-\zeta_2^2}}\right)^2 + \left((a_{k\zeta_1} - a_{k\zeta_2})(1-\zeta_1^2)\right)^2}} \tag{6.32}$$

However, finding the damping ratio using Equation (6.32) is unreliable against noise, and the method is very sensitive to inaccuracies in the frequency estimation. Notice also that a small difference between $a_{k\zeta_1}$ and $a_{k\zeta_2}$ increases the sensitivity to noise. From Equation (6.24), it can be shown that the difference $|a_{k\zeta_1} - a_{k\zeta_2}|$ is found to be bounded by the inequality

$$|a_{k\zeta_1} - a_{k\zeta_2}| \leq \left| \frac{\zeta_1}{\sqrt{1-\zeta_1^2}} - \frac{\zeta_2}{\sqrt{1-\zeta_2^2}} \right| \tag{6.33}$$

if an accurate priory estimation of the ω_{dk} using the methods in 6.2.1 is performed, the damping ratio value can be tuned to reach better estimation. This notion relies on the fact that when $\zeta = \xi_k$, the peak scale exactly satisfies $a_{k2} = 1/\omega_{dk}$ as can be inferred from

equation 6.24. In summary, equation 6.24 shows that

$$\begin{aligned} \zeta < \xi_k \quad &\rightarrow \quad a_k < \frac{1}{\omega_{dk}} \\ \zeta = \xi_k \quad &\rightarrow \quad a_k = \frac{1}{\omega_{dk}} \\ \zeta > \xi_k \quad &\rightarrow \quad a_k > \frac{1}{\omega_{dk}} \end{aligned} \tag{6.34}$$

which eases the task of tuning ξ_k. The procedure of finding the damping ratio within error ϵ using the tuning method can be summarized by the following steps:

1. Find ω_{dk} using a suitable method from Section 6.2.1.
2. Choose a family of Laplace wavelets by picking a ζ and perform the LWT.
3. Find a_k from the LWT scalogram or spectrogram and compare it to ω_{dk} by computing the error
$$E_\zeta = a_k - \frac{1}{\omega_{dk}} \tag{6.35}$$
4. If $E_\zeta > \epsilon$, decrease ζ, and if $E_\zeta < -\epsilon$, increase ζ, then move back to step 2. continue until $|E_\zeta| < \epsilon$.

Hilbert transform method

With the presence of noise, absence of accurate information about the natural frequencies, and small unmodeled nonlinearities, the Hilbert Transform (HT) offers a more robust mean against noise for estimating the damping ration. The HT extracts the modulating envelop of a harmonic signal [60], hence the decaying envelop can be extracted from an oscillatory signal. For a signal $f(t)$, the HT is defined by

$$\mathcal{H}\{f(t)\} = \frac{1}{\pi} \int_{-\infty}^{\infty} \frac{f(t)}{t-\tau} dt \tag{6.36}$$

$\mathcal{H}\{f(t)\}$ is the imaginary part of the analytic signal of $f(t)$. The analytic signal of $f(t)$ is defined by

$$\mathrm{F}(t) = f_R(t) + j f_I(t) \tag{6.37}$$

where $f_R(t) = f(t)$ and $f_I(t) = \mathcal{H}\{f(t)\}$. $f_I(t)$ is shifted from $f_R(t)$ by phase shift equal to $\frac{\pi}{2}$. If $f(t) = \sin(t)$ then $f_I(t) = \cos(t)$. Therefore, the magnitude of $\mathrm{F}(t)$ represents the enveloping function of oscillatory signals.

After separating the modes using the LWT, apply the HT to the LWT. This, in turn, removes the sinusoidal oscillations from the LWT and leaves smooth exponentially decaying ridges in the scalogram or the spectrogram. From Equation (6.8), we find that if the ridge is centered at scale a_k, then the HT of that ridge leaves a ridge decaying with exponential rate equal to $\frac{-\omega_{dk}\xi_k}{\sqrt{1-\xi_k^2}}$. Consequently, to estimate the damping ratio, the oscillating frequency has to be estimated first by one of the methods in Section 6.2.1.

The method is summarized by following steps:

1. Evaluate the LWT of the signal.
2. Find the frequency ω_{dk}.
3. Take the horizontal cross section of the LWT at a_k.
4. Apply the Hilbert transform to the LWT.
5. Take the logarithm of the Hilbert transform to convert the exponential curve to straight line.
6. The slope of the line is given by

$$\nu = \frac{-\omega_{dk}\xi_k}{\sqrt{1-\xi_k^2}} \tag{6.38}$$

from which the damping ration is given by

$$\xi_k = \frac{1}{\sqrt{1+\left(\frac{\omega_{dk}}{\nu}\right)^2}} \tag{6.39}$$

6.3 Application Example

To apply and validate the methods described in the previous sections, an example for MDOF systems is tested. The example is a simulated LTI 3-DOF system, the parameter of which are exactly known. This example is presented for validity and comparison purposes.

6.3.1 Simulated LTI 3-DOF system

The parameters of the simulated system are given in Tables 6.1 and 6.2. After obtaining the response, white noise is added to it at a 20 dB SNR. From the analysis in Chapter 5, it is found that the velocity signal amplifies the high frequency components, so their weight

Table 6.1: Physical parameters for 3-DOF Linear mass-spring-damper system

Mass (kg)	Stiffness (N/m)	Damping (N.s/m)
1.5	350	8
1	2500	12
1	5000	1.5

Table 6.2: Dynamic parameters for the 3-DOF Linear mass-spring-damper system

Mode	Natural Frequency (ω_{nk}(Hz))	Oscillating frequency (ω_{dk}(Hz))	Damping Ratio ξ_k
1st	1.55	1.473	0.315
2nd	8.17	8.16	0.044
3rd	17.18	17.163	0.038

is larger in harmonic analysis. Therefore, the velocities are analyzed in the forthcoming analysis.

Applying the LWT with $\zeta = 0.001$ to the velocity response of the system generates three ridges as shown by Figure 6.3. The ridges extend along the frequencies of 1.66 Hz, 8.11 Hz, and 17.65 Hz. These are the oscillating frequencies, which are related to the natural frequencies by $\omega_{dk} = \omega_{nk}\sqrt{1-\zeta_k^2}$. Table 6.3 lists the peak frequencies obtained from the LWT spectrogram and from the classical FFT. The FFT spectrum is shown in Figure 6.4.

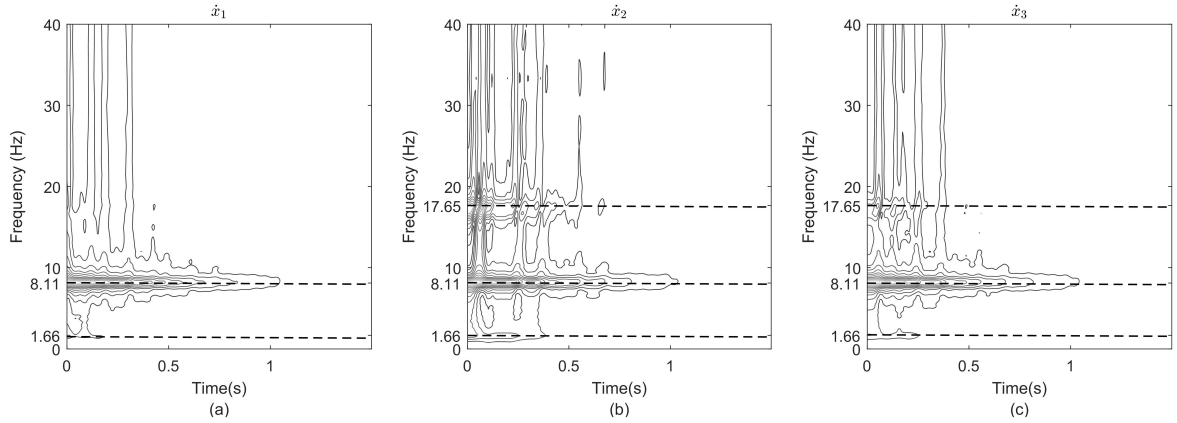

Figure 6.3: Laplace Wavelet Spectrogram for the response of the simulated 3 DOF system. (a) $\dot{x}_1(t)$ spectrogram. (b) $\dot{x}_2(t)$ spectrogram. (c) $\dot{x}_3(t)$ spectrogram.

The next step in the analysis is finding the LWT at peak frequencies. This resembles extracting the cross-sections of the LWT spectrogram at the peak frequencies, and gives modes separation. Figures 6.5 to 6.7 show the cross-sections for the responses of the three degrees of freedom. Applying the FFT for each cross-section reveals to us how the LWT separates the modes. Figures 6.8 to 6.10 show the FFT of each cross-section for $x_1(t)$, $x_2(t)$, and $x_3(t)$

Table 6.3: Estimated frequencies by LWT and FFT.

Mode	LWT	FFT
1st	1.66	1.6
2nd	8.11	8.2
3rd	17.65	17.4

Table 6.4: Estimated slopes of the envelopes natural logarithm and estimated damping ratios from the velocity response.

	Estimated Slope (ν)							
Mode	$\dot{x}_1(t)$	$\dot{x}_2(t)$	$\dot{x}_3(t)$	Average	Actual	% Slope Err.	ξ (Est.)	$\%\xi_k$ Err.
1st	-2.5427	-2.5377	-2.4634	-2.5146	-3.08	18.36%	0.2411	23%
2nd	-2.2766	-2.1673	-2.2767	-2.2402	-2.27	1.31%	0.044	0%
3rd	-2.8680	-4.4805	-3.1679	-3.5055	-4.07	13.87%	0.032	15.8%

respectively.

To estimate the damping ratio associated with each mode, apply the HT to the cross-sections. Then find the magnitude of the analytic signals of $x_1(t)$, $x_2(t)$ and $x_3(t)$ to obtain the envelop of each cross-section. Figure 6.11 shows the envelops for the three output velocities at the three modal cross-sections.

To find the damping ratios, apply the natural logarithm to each envelop, then find the slope of the line that minimizes the root mean square error. Figure 6.12 shows the natural logarithm for each envelop in Figure 6.11. The slope of the line, $\nu = -\xi_k\omega_k$, is given in Equation (6.38), from which the modal damping ratio ξ_k can be found using Equation (6.39). Table 6.4 lists the slopes and the estimations . From the estimated frequencies in Table 6.3, the damping ratio can be found by dividing the values in Equation (6.39) by the natural frequencies. 6.5 lists the estimated damping ratios, with the corresponding errors, based on the average values in Equation (6.39).

The error in estimating the 1st mode's damping ratio is relatively large. To reduce the error, consider analyzing the displacement. The same procedure is repeated with the displacement response. 6.13 shows the HT envelops of the displacement spectrograms cross-sections, while 6.14 shows the natural logarithm of the envelops.Table 6.5 lists the estimated envelop slopes based on the analysis of the displacement response of the system. In general, the results showed significant improvements in the estimation of the 1st and 3rd mode damping ratio, while the 2nd mode damping ration has small error that does not exceed 2%.

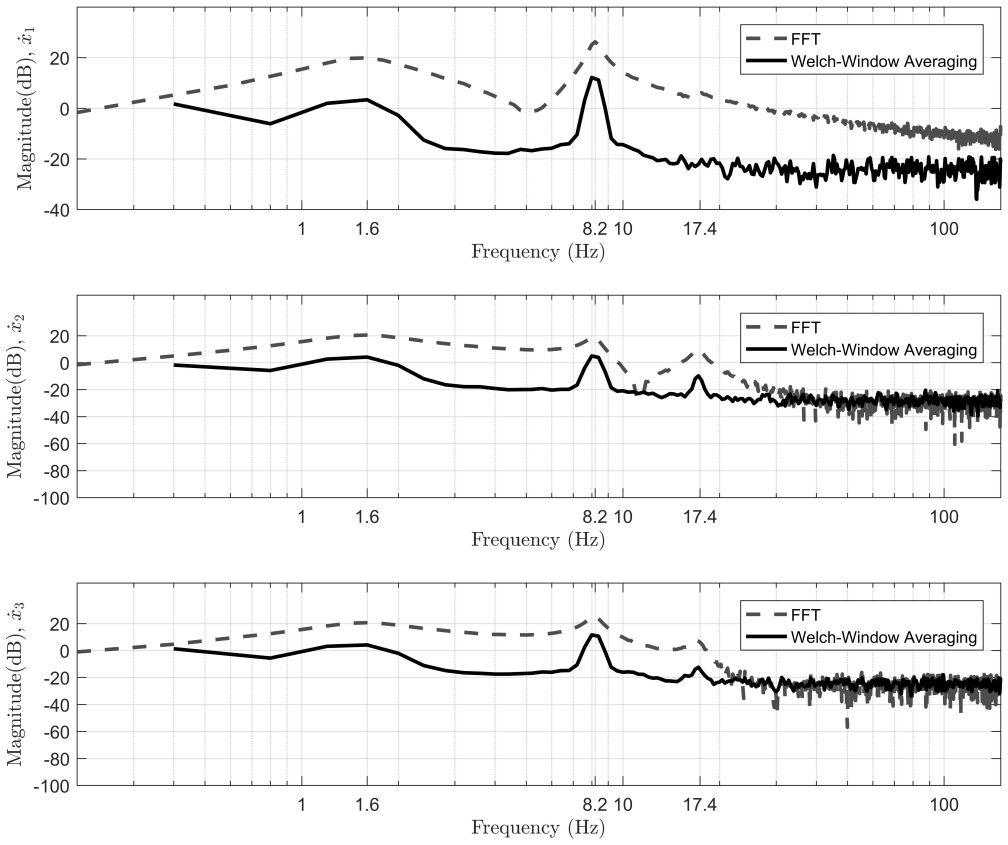

Figure 6.4: Spectrums of the simulated example response. Top $\dot{x}_1(t)$, Center $\dot{x}_2(t)$, and Bottom $\dot{x}_3(t)$.

Table 6.5: Estimated slopes of envelopes exponentials and estimated damping ratios from the displacement response.

	Estimated Slope (ν)							
Mode	$\dot{x}_1(t)$	$\dot{x}_2(t)$	$\dot{x}_3(t)$	Average	Actual	% Slope Err.	ξ_k (Est.)	% ξ_k Err.
1st	-3.0587	-3.4570	-3.3893	-3.3016	-3.08	6.71%	0.3165	−0.4919%
2nd	-2.1579	-2.1404	-2.3006	-2.1997	-2.27	3.20%	0.0432	1.89%
3rd	-3.9223	-4.1812	-3.8655	-3.9897	-4.07	2.01%	0.0361	5.06%

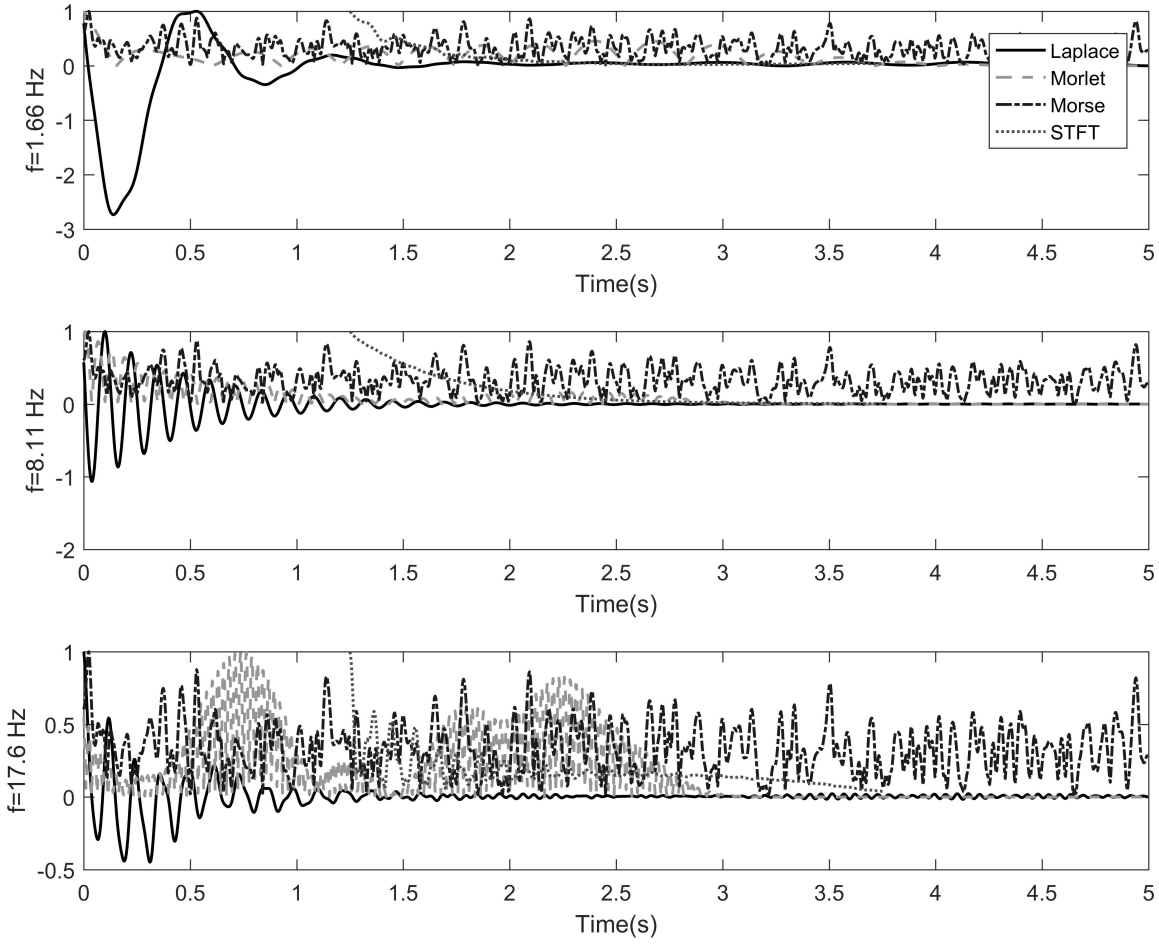

Figure 6.5: LWT of $\dot{x}_1(t)$ at the modal frequencies. Top, first mode; center, second mode; bottom, third mode.

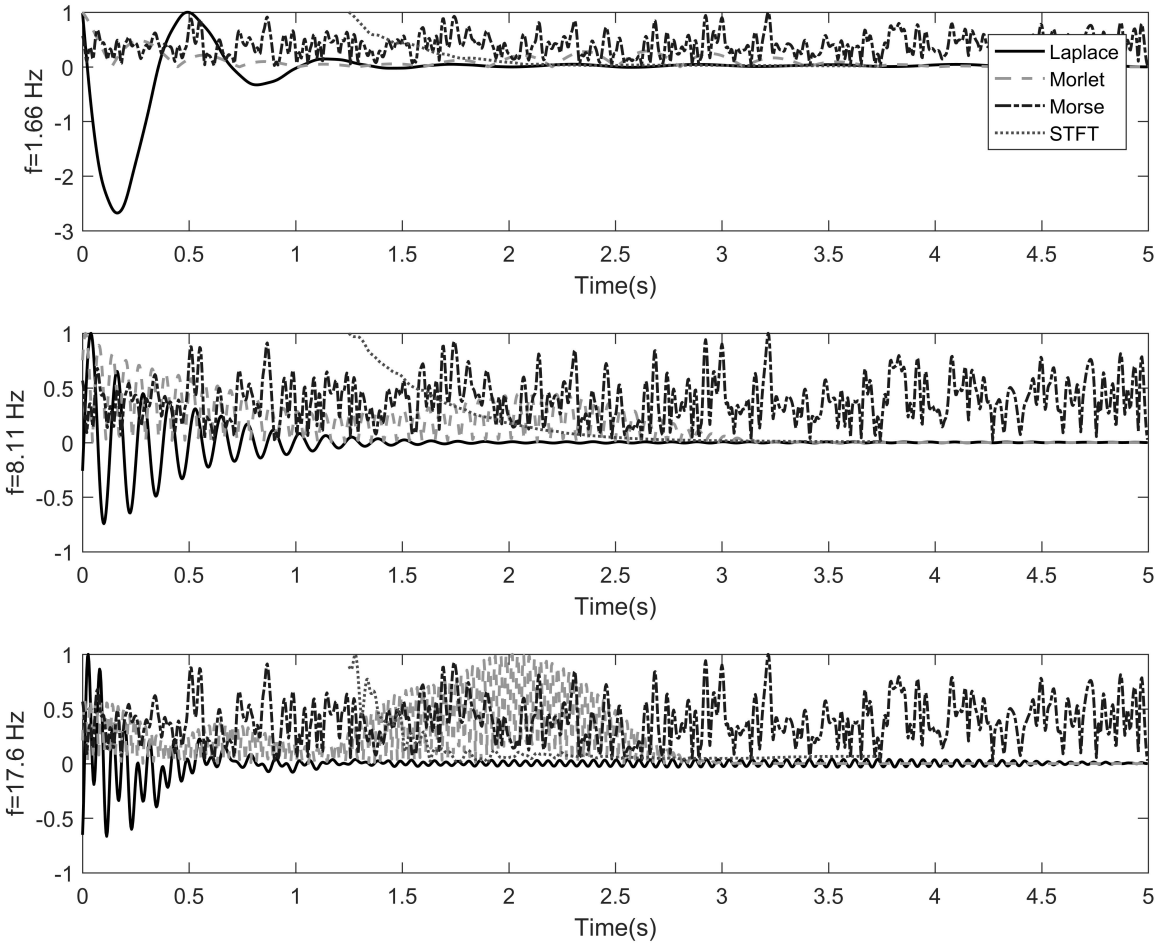

Figure 6.6: LWT of $\dot{x}_2(t)$ at the modal frequencies. Top, first mode; center, second mode; bottom, third mode.

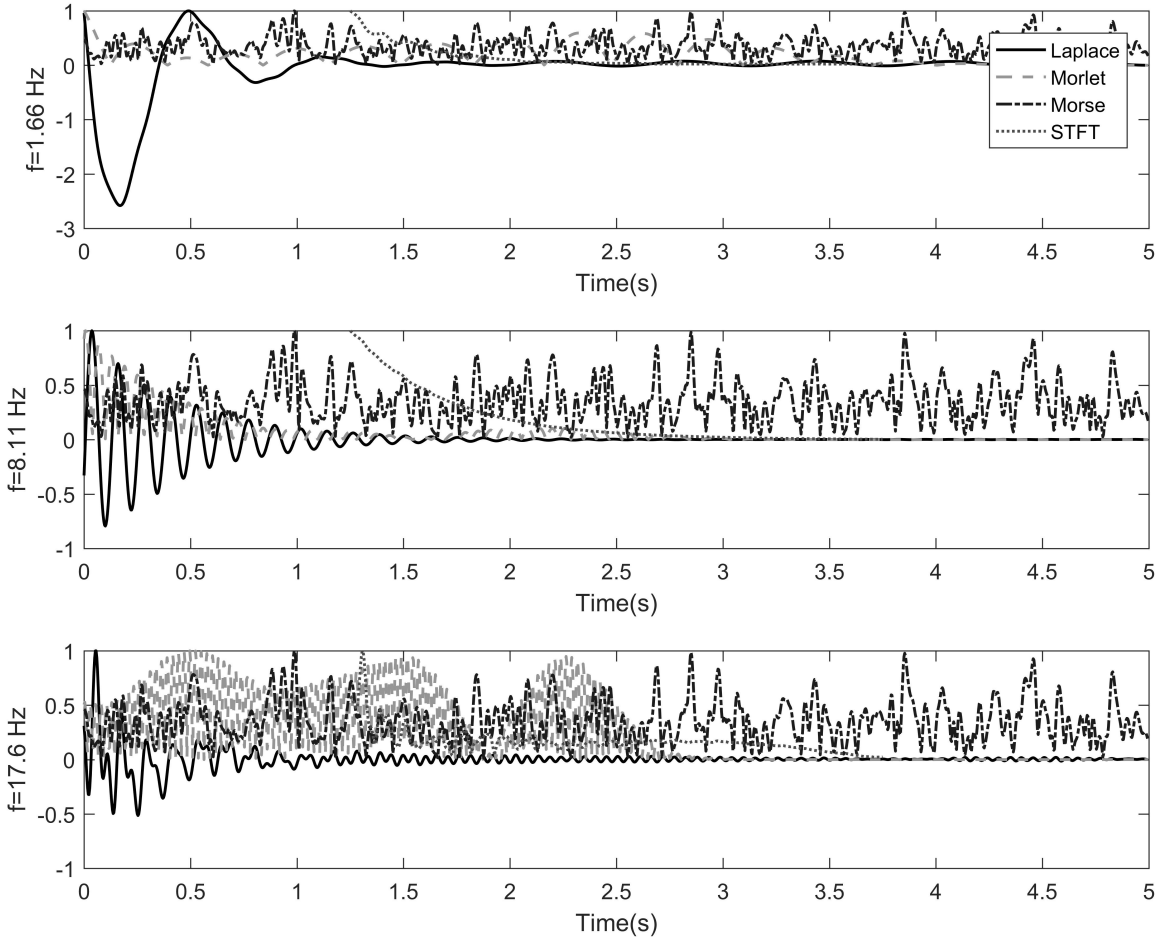

Figure 6.7: LWT of $\dot{x}_3(t)$ at the modal frequencies. Top, first mode; center, second mode; bottom, third mode.

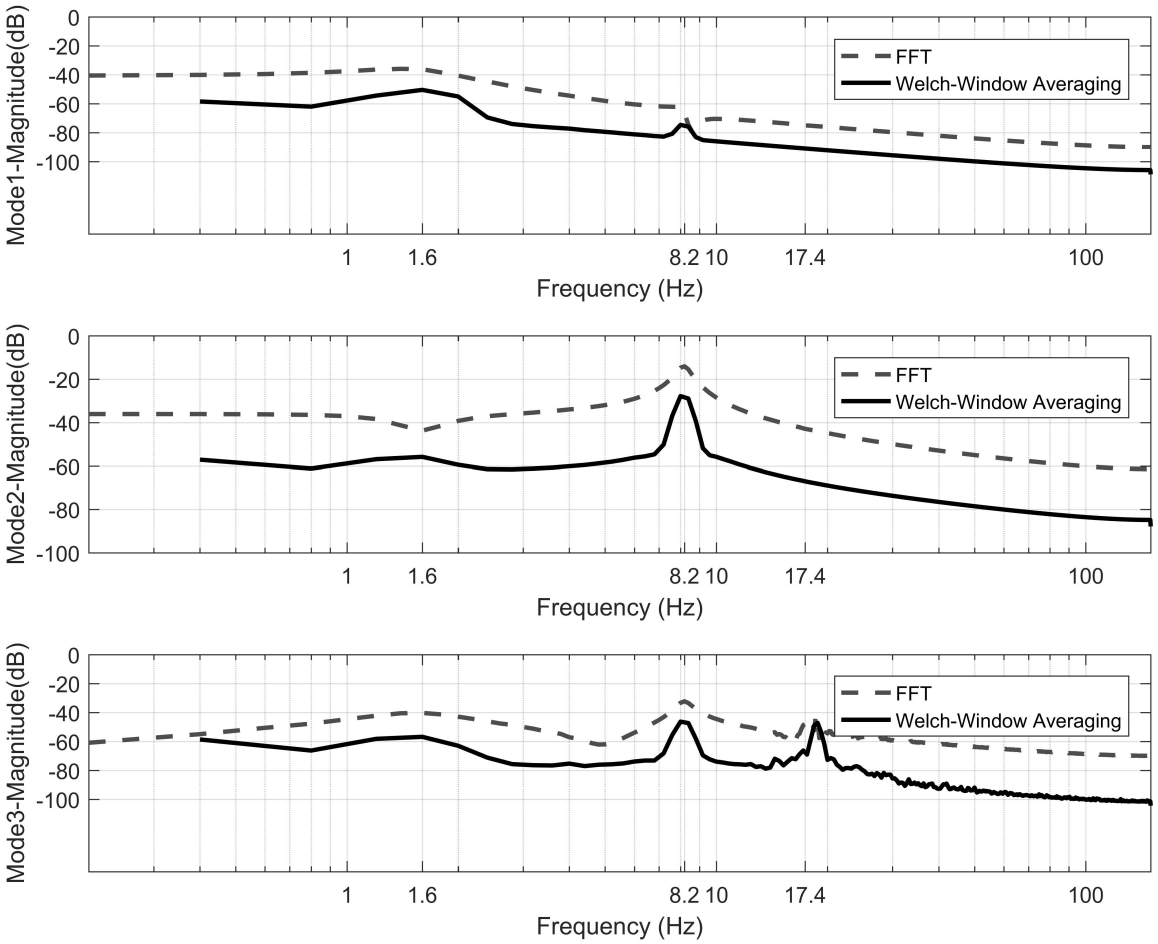

Figure 6.8: Spectrums of the LWT of $\dot{x}_1(t)$ at the modal frequencies. Top, first mode; center, second mode; bottom, third mode.

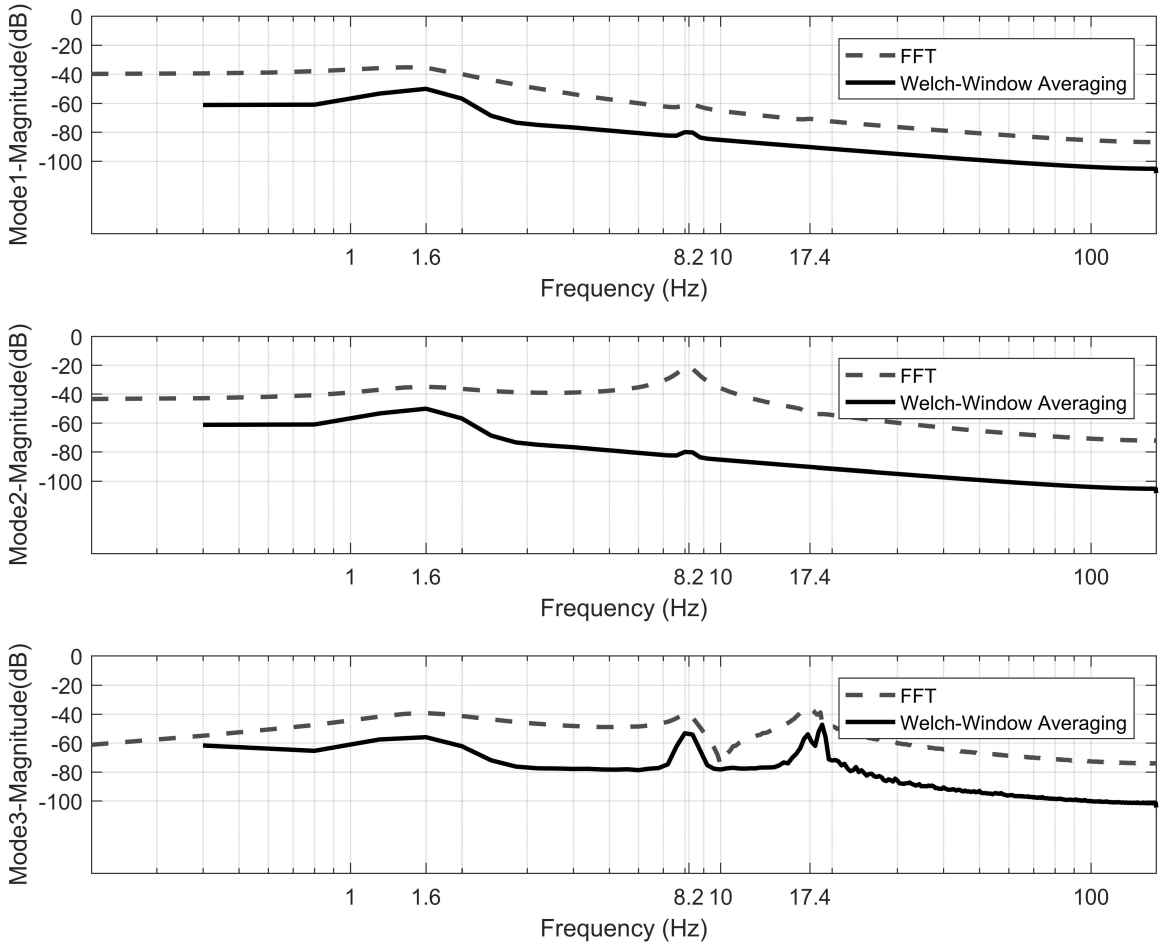

Figure 6.9: Spectrums of the LWT of $\dot{x}_2(t)$ at the modal frequencies. Top, first mode; center, second mode; bottom, third mode.

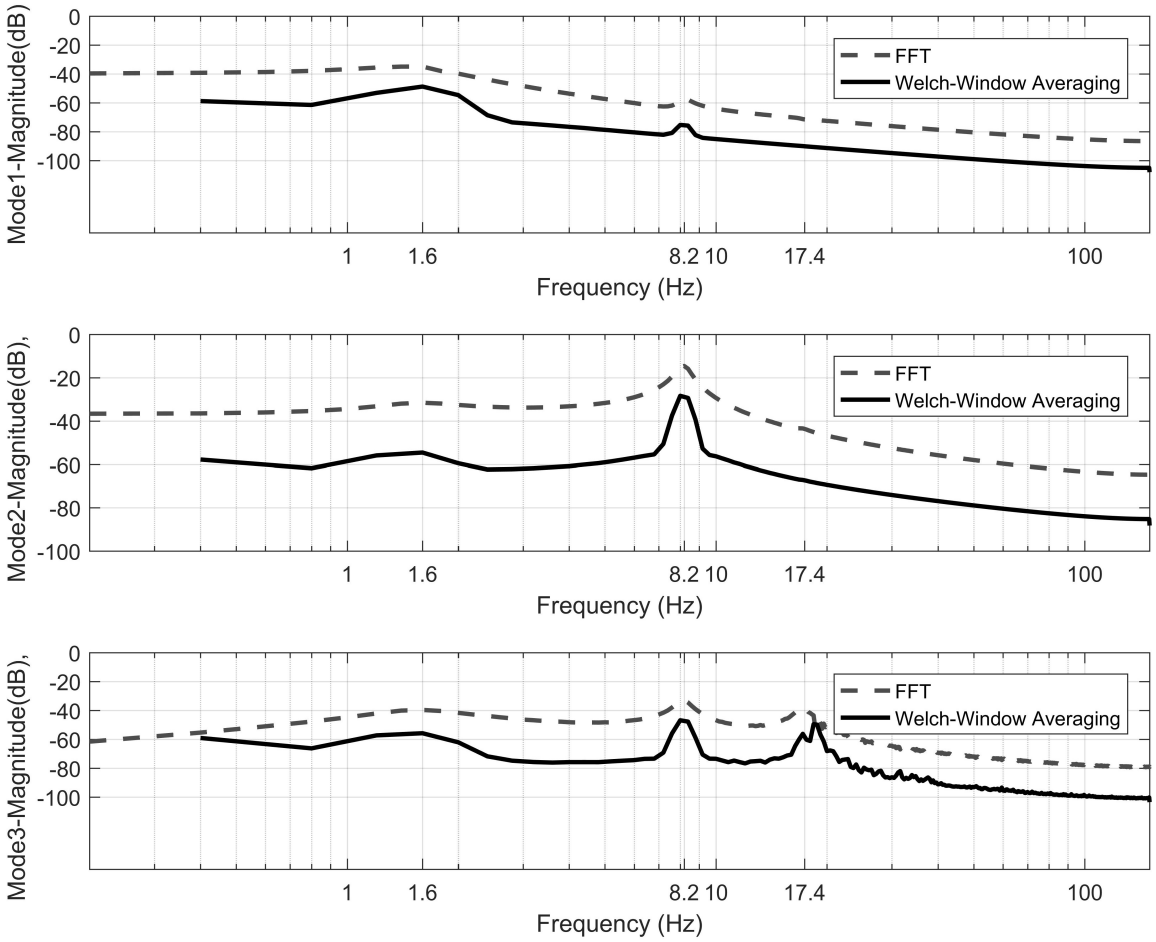

Figure 6.10: Spectrums of the LWT of $\dot{x}_3(t)$ at the modal frequencies. Top, first mode; center, second mode; bottom, third mode.

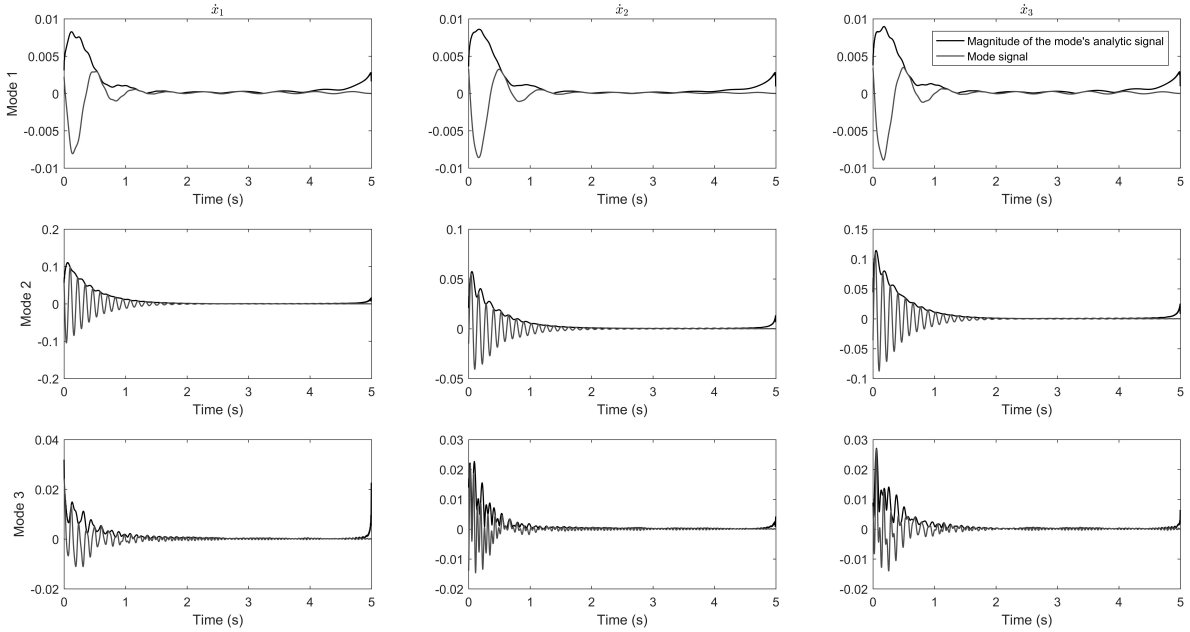

Figure 6.11: Hilbert envelops of the modes. Top row, first mode; center row, second mode; bottom row, third mode. Left column, $\dot{x}_1(t)$, center column, $\dot{x}_2(t)$, right column $\dot{x}_3(t)$

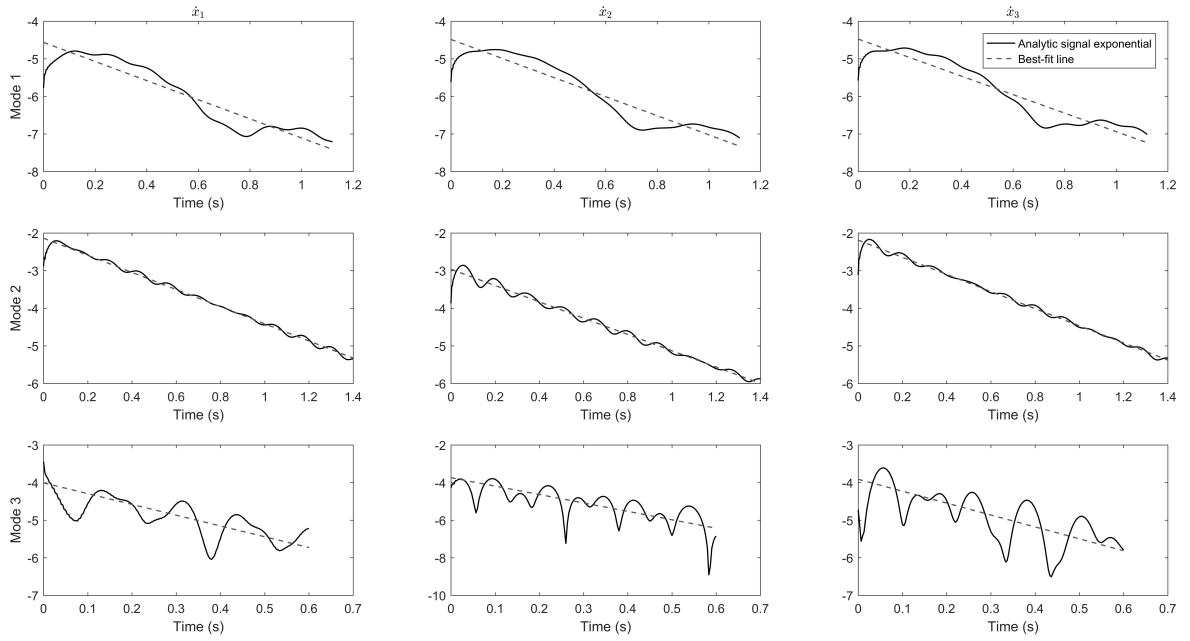

Figure 6.12: Natural logarithm of the decaying envelops in Figure 6.11. Top row, first mode; center row, second mode; bottom row, third mode. Left column, $\dot{x}_1(t)$, center column, $\dot{x}_2(t)$, right column $\dot{x}_3(t)$

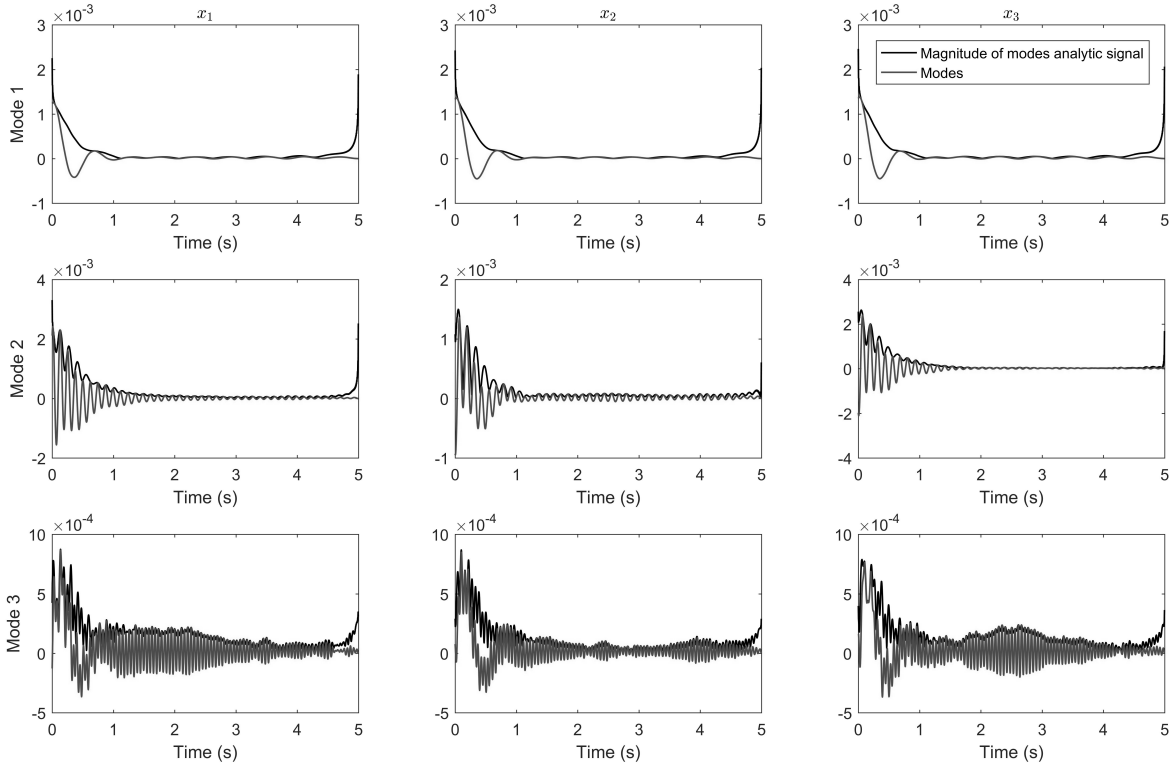

Figure 6.13: Hilbert envelops of the modes. Top row, first mode; center row, second mode; bottom row, third mode. Left column, $x_1(t)$, center column, $x_2(t)$, right column $x_3(t)$

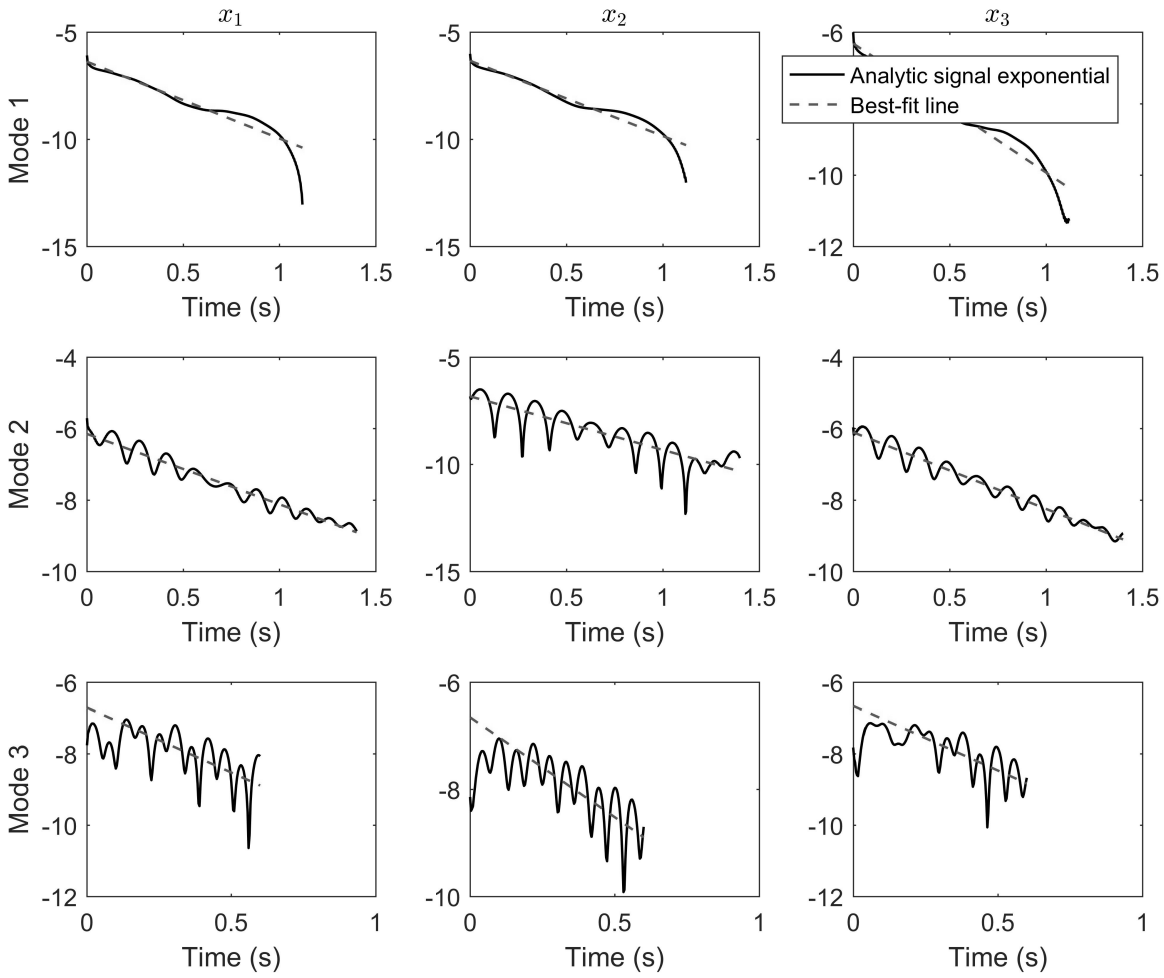

Figure 6.14: Natural logarithm of the decaying envelops in Figure 6.11. Top row, first mode; center row, second mode; bottom row, third mode. Left column, $x_1(t)$, center column, $x_2(t)$, right column $x_3(t)$

Chapter 7

Concluding Remarks

It was shown that the impulse response of the Second Order Underdamped LTI systems can be used as a wavelet to obtain time-scale and time-frequency analysis directly. Also, it was proved that once the wavelet transform is performed, the transform can be reversed to obtain the original signal, hence an inverse wavelet transform for the SOULTI wavelet exists. A region of convergence can be defined for the transform on the scale domain. This region defines for which range of scales the SOULTI wavelet transform converges.

Then, the wavelet was generalized to the complex domain and become the Laplace wavelet. The properties of the new generalization inherits many properties from the Laplace transform. It also introduces phase of transform. Moreover, the original signal can be retrieved back by substituting the transform into the reconstruction differential equation. The SOULTI and the Laplace wavelet can be evaluated for most elementary functions and basic signals. In addition, there is a direct relation between the SOULTI and the Laplace wavelet transform of a signal and the transform of its derivative or integral. For a wavelet scaling power $p = 1$, we found that the time-frequency resolution is preserved constant using the three definitions of time-frequency resolution.

The RWT can reveal whether the distortion at the end of the time range on scalograms and spectrograms is due to edge effect or not. Moreover, taking the average between the FWT and RWT is a practical and simple method to eliminate the edge effect on both edges.

The most important property of the SOULTI and Laplace wavelets is the particular solution property. The property shows that the wavelet transform gives the particular solution of the reconstruction differential equations. This property proved to be useful in application such as the modal parameters identification.

The Laplace and SOULTI wavelets can separate the modes of vibrations clearly and reduce the noise in the signal. Each mode carries a main frequency that represent the frequency of the LWT cross-section along a peak frequency.

The Laplace and SOULTI transforms can be applied to the mathematical model of linear systems, and to the response of nonlinear systems. The presented results can be extended to define a Laplace wavelet-based or SOULT wavelet-based time-frequency wavelet response function. The SOULTI and the Laplace wavelet transform formula provides an analytical tool for time-frequency or time-scale representation of basic signals. It also preserves all the important characteristics and parameters that exist in the time domain to the time-scale or time-frequency domain.

Bibliography

[1] Tariq Abuhamdia and Saied Taheri. Wavelets as a tool for systems analysis and control. *Journal of Vibration and Control*, pages 1077546315620923 Copyright © 2015 SAGE Publications. Reprinted by permission of SAGE Publications, http://journals.sagepub.com/doi/abs/10.1177/1077546315620923, 2015. URL `http://journals.sagepub.com/doi/abs/10.1177/1077546315620923`.

[2] Tariq Abuhamdia, Saied Taheri, and John Burns. A new wavelet family based on second-order lti-systems. *Journal of Vibration and Control*, pages 1177/1077546316674089 Copyright © 2016 SAGE Publications. Reprinted by permission of SAGE Publications, http://journals.sagepub.com/doi/full/10.1177/1077546316674089, 2016. URL `http://journals.sagepub.com/doi/full/10.1177/1077546316674089`.

[3] Jonathan M Aitken and Tim Clarke. Observer/Kalman filter identification with wavelets. *Signal Processing, IEEE Transactions on*, 60(7):3476–3485, 2012.

[4] Pierre Argoul. Linear dynamical identification: An integral transform seen as a complex wavelet transform. *Meccanica*, 32(3):215 – 222, 1997. ISSN 00256455. URL `http://dx.doi.org/10.1023/A:1004274709070`.

[5] Pierre Argoul and Silvano Erlicher. On the use of continuous wavelet analysis for modal identification. *Lecture Notes in Applied and Computational Mechanics*, 23:359 – 368, 2005. ISSN 16137736.

[6] Pierre Argoul and Thien-Phu Le. Instantaneous indicators of structural behaviour based on the continuous Cauchy wavelet analysis. *Mechanical Systems and Signal Processing*, 17(1):243 – 250, 2003. ISSN 08883270. URL `http://dx.doi.org/10.1006/mssp.2002.1557`.

[7] Sami Barmada, Antonino Musolino, and Marco Raugi. Analysis of integrated circuit system s by an innovative wavelet-based scattering matrix approach. *Advanced Packaging, IEEE Transactions on*, 30(1):86–96, 2007.

[8] B Basu and VK Gupta. On wavelet-analyzed seismic response of SDOF systems. In *Symposium on Time–Frequency and Wavelet Analysis, ASME 16th Biennial Conference on Mechanical Vibration and Noise, Sacramento, USA*, 1997.

[9] Biswajit Basu and Vinay K. Gupta. Non-stationary seismic response of MDOF systems by wavelet transform. *Earthquake Engineering and Structural Dynamics*, 26(12):1243–1258, 1997. ISSN 1096-9845. doi: 10.1002/(SICI)1096-9845(199712)26:12⟨1243::AID-EQE708⟩3.0.CO;2-P. URL http://dx.doi.org/10.1002/(SICI)1096-9845(199712)26:12<1243::AID-EQE708>3.0.CO;2-P.

[10] Biswajit Basu and Vinay K. Gupta. Seismic response of sdof systems by wavelet modeling of nonstationary processes. *Journal of Engineering Mechanics*, 124(10):1142, 1998. ISSN 07339399. URL http://ezproxy.lib.vt.edu:8080/login?url=http://search.ebscohost.com/login.aspx?direct=true&db=a9h&AN=1116875&scope=site.

[11] Biswajit Basu and VK Gupta. Wavelet-based analysis of the non-stationary response of a slipping foundation. *Journal of Sound and Vibration*, 222(4):547–563, 1999.

[12] Biswajit Basu, Satish Nagarajaiah, and Arunasis Chakraborty. Online identification of linear time-varying stiffness of structural systems by wavelet analysis. *Structural Health Monitoring*, 7(1):21–36, 2008.

[13] Saroj Biswas, Qing Dong, and Li Bai. Computation of optimal control of linear systems using Haar wavelets. *International Journal of Innovative Computing Iinformation and Control*, 8(5 B):3819–3831, 2012.

[14] Arunasis Chakraborty, Biswajit Basu, and Mira Mitra. Identification of modal parameters of a mdof system by modified L–P wavelet packets. *Journal of sound and vibration*, 295(3):827–837, 2006.

[15] Avijit Chakraborty and David Okaya. Frequency-time decomposition of seismic data using wavelet-based methods. *Geophysics*, 60(6):1906–1916, 1995.

[16] Chih-Chen Chang and Yuanfeng Shi. Identification of time-varying hysteretic structures using wavelet multiresolution analysis. *International Journal of Non-Linear Mechanics*, 45(1):21–34, 2010.

[17] Bor-Sen Chen and Yu-Min Cheng. Adaptive wavelet network control design for nonlinear systems. In *Decision and Control, 1996., Proceedings of the 35th IEEE Conference on*, volume 3, pages 3224–3229. IEEE, 1996.

[18] C.F. Chen and C.-H. Hsiao. Wavelet approach to optimising dynamic systems. *Control Theory and Applications, IEE Proceedings* -, 146(2):213–219, Mar 1999. ISSN 1350-2379. doi: 10.1049/ip-cta:19990516.

[19] CF Chen and CH Hsiao. Haar wavelet method for solving lumped and distributed-parameter systems. In *Control Theory and Applications, IEE Proceedings-*, pages 87–94. IET, 1997.

[20] Chun-Sheng Chen and Wei-Song Lin. Adaptive wavelet sliding mode control of uncertain multivariable nonlinear systems. In *American Control Conference, 2003. Proceedings of the 2003*, volume 1, pages 180–185. IEEE, 2003.

[21] Jie Chen, Changpeng Pan, and Wenjin Gu. A nonlinear control algorithm based on adaptive wavelet net for STT anti-ship missile. In *Computational Engineering in Systems Applications, IMACS Multiconference on*, volume 1, pages 607–612, Oct 2006. doi: 10.1109/CESA.2006.4281725.

[22] Kenneth C Chou. The use of wavelets for efficient, active control of distributed parameter systems. In *Signals, Systems and Computers, 1995. 1995 Conference Record of the Twenty-Ninth Asilomar Conference on*, volume 2, pages 1260–1264. IEEE, 1995.

[23] TACM Claasen and WFG Mecklenbrauker. The wigner distribution - a tool for time-frequency signal analysis, part I: Continuous time signal. *Philips Journal for Research*, 1980.

[24] D Coca and SA Billings. Continuous-time system identification for linear and nonlinear systems using wavelet decompositions. *International Journal of Bifurcation and Chaos*, 7(01):87–96, 1997.

[25] R.R. Coifman and M.V. Wickerhauser. Entropy-based algorithms for best basis selection. *Information Theory, IEEE Transactions on*, 38(2):713–718, March 1992. ISSN 0018-9448. doi: 10.1109/18.119732.

[26] MOT Cole, PS Keogh, CR Burrows, and MN Sahinakaya. Adaptive control of rotor vibration using compact wavelet. *Journal of Vibration and Acoustics*, 128(5):653–665, October 2006.

[27] I. Daubechies. Orthonormal bases of wavelets with finite support connection with discrete filters. In Jean-Michel Combes, Alexander Grossmann, and Philippe Tchamitchian, editors, *Wavelets*, Inverse Problems and Theoretical Imaging, pages 38–66. Springer Berlin Heidelberg, 1989. ISBN 978-3-642-97179-2. doi: 10.1007/978-3-642-97177-8_3. URL `http://dx.doi.org/10.1007/978-3-642-97177-8_3`.

[28] I. Daubechies. *Ten Lectures on Wavelets*. Society for Industrial and Applied Mathematics (SIAM), 1992. doi: 10.1137/1.9781611970104. URL `http://epubs.siam.org/doi/abs/10.1137/1.9781611970104`.

[29] N. Delprat, B. Escudie, P. Guillemain, R. Kronland-Martinet, P. Tchamitchian, and B. Torresani. Asymptotic wavelet and gabor analysis: extraction of instantaneous

frequencies. *Information Theory, IEEE Transactions on*, 38(2):644–664, March 1992. ISSN 0018-9448. doi: 10.1109/18.119728.

[30] Alejandro R Díaz. A wavelet–Galerkin scheme for analysis of large-scale problems on simple domains. *International journal for numerical methods in engineering*, 44(11): 1599–1616, 1999.

[31] Dou-Zhang Ding and Xing-Sheng Gu. Boundary predictive control of first-order linear modulus-varying distributed parameter systems based on wavelets transformation. In *Wavelet Analysis and Pattern Recognition, 2007. ICWAPR'07. International Conference on*, volume 4, pages 1550–1555. IEEE, 2007.

[32] Huang Dishan. A wavelet-based algorithm for the Hilbert transform. *Mechanical Systems and Signal Processing*, 10(2):125–134, 1996.

[33] K Dziedziech, WJ Staszewski, and T Uhl. Input-output time-frequency analysis of time-variant systems. In *International conference on Uncertainty in Structural Dynamics, Leuven*, pages 2765–2774, 2012.

[34] R Ebrahimi, MA Vali, M Samavat, and AA Gharavisi. A computational method for solving optimal control of singular systems using the Legendre wavelets. *ICGST-ACSE Journal*, 9(2):1–6, 2009.

[35] Silvano Erlicher and Pierre Argoul. Modal identification of linear non-proportionally damped systems by wavelet transform. *Mechanical Systems and signal processing*, 21 (3):1386–1421, 2006.

[36] Lawrence C Freudinger, Rick Lind, and Martin J Brenner. Correlation filtering of modal dynamics using the laplace wavelet. In *International Modal Analysis Conference*, pages 868–877, Santa Barbara, CA, Febraury 1998.

[37] A Gandelli and S Leva. Direct Haar-space control for dc motors. In *Circuits and Systems, 2001. MWSCAS 2001. Proceedings of the 44th IEEE 2001 Midwest Symposium on*, volume 2, pages 984–988. IEEE, 2001.

[38] A Gandelli and Sonia Leva. Haar state equations for power electronics system modeling. In *Circuits and Systems, 2001. ISCAS 2001. The 2001 IEEE International Symposium on*, volume 3, pages 525–528. IEEE, 2001.

[39] A. Gandelli, A. Monti, and F. Ponci. State equations in the Haar domain. In *Circuits and Systems, 1999. 42nd Midwest Symposium on*, volume 2, pages 596–599 vol. 2, 1999. doi: 10.1109/MWSCAS.1999.867709.

[40] Roger Ghanem and Francesco Romeo. A wavelet-based approach for the identification of linear time-varying dynamical systems. *Journal of Sound and Vibration*, 234(4): 555–576, 2000.

[41] Roger Ghanem and Francesco Romeo. A wavelet-based approach for model and parameter identification of non-linear systems. *International Journal of Non-Linear Mechanics*, 36(5):835–859, 2001.

[42] J. C. Goswami and A. K. Chan. *Fundamentals of Wavelets: Theory, Algorithms, and Applications*. Wiley Series in Microwave and Optical Engineering. John Wiley and Sons, Inc., New York, NY, 1999.

[43] Xinyi Gu, Gengyin Li, Ming Zhou, and K.L. Lo. Wavelet transform based approach to harmonic analysis. In *Electrical Power Quality and Utilisation (EPQU), 2011 11th International Conference on*, pages 1–6, Oct 2011. doi: 10.1109/EPQU.2011.6128954.

[44] Alfred Haar. Zur theorie der orthogonalen funktionensysteme. *Mathematische Annalen*, 69(3):331–371, 1910.

[45] Stéphane Hans, E Ibraim, Stéphane Pernot, Claude Boutin, and C-H Lamarque. Damping identification in multi-degree-of-freedom system via a wavelet-logarithmic decrement-part 2: Study of a civil engineering building. *Journal of Sound and Vibration*, 235(3):375–403, 2000.

[46] F.J. Harris. On the use of windows for harmonic analysis with the discrete Fourier transform. *Proceedings of the IEEE*, 66(1):51–83, Jan 1978. ISSN 0018-9219. doi: 10.1109/PROC.1978.10837.

[47] Daniel WC Ho, Ping-Au Zhang, and Jinhua Xu. Fuzzy wavelet networks for function learning. *Fuzzy Systems, IEEE Transactions on*, 9(1):200–211, 2001.

[48] Zhikun Hou and Adriana Hera. A system identification technique using pseudo-wavelets. *Journal of Intelligent Material Systems and Structures*, 12(10):681–687, 2001. doi: 10.1177/104538901320560328. URL `http://jim.sagepub.com/content/12/10/681.abstract`.

[49] Zhikun Hou and Adriana Hera. System identification technique using truncated pseudo-wavelet transform. In *SPIE's 8th Annual International Symposium on Smart Structures and Materials*, pages 198–207. International Society for Optics and Photonics, 2001.

[50] Chun-Hui Hsiao and Wen-June Wang. State analysis and optimal control of linear time-varying systems via Haar wavelets. *Optimal Control Applications and Methods*, 19(6):423–433, 1998.

[51] CS Huang and WC Su. Identification of modal parameters of a time invariant linear system by continuous wavelet transformation. *Mechanical Systems and Signal Processing*, 21(4):1642–1664, 2007.

[52] CS Huang, SL Hung, CI Lin, and WC Su. A wavelet-based approach to identifying structural modal parameters from seismic response and free vibration data. *Computer-Aided Civil and Infrastructure Engineering*, 20(6):408–423, 2005. ISSN 1467-8667. doi: 10.1111/j.1467-8667.2005.00406.x. URL `http://dx.doi.org/10.1111/j.1467-8667.2005.00406.x`.

[53] CS Huang, SL Hung, WC Su, and CL Wu. Identification of time-variant modal parameters using time-varying autoregressive with exogenous input and low-order polynomial function. *Computer-Aided Civil and Infrastructure Engineering*, 24(7): 470–491, 2009. ISSN 1467-8667. doi: 10.1111/j.1467-8667.2009.00605.x. URL `http://dx.doi.org/10.1111/j.1467-8667.2009.00605.x`.

[54] Norden E Huang, Zheng Shen, Steven R Long, Manli C Wu, Hsing H Shih, Quanan Zheng, Nai-Chyuan Yen, Chi Chao Tung, and Henry H Liu. The empirical mode decomposition and the Hilbert spectrum for nonlinear and non-stationary time series analysis. *Proceedings of the Royal Society of London. Series A: Mathematical, Physical and Engineering Sciences*, 454(1971):903–995, 1998.

[55] O Islas-Gomez, LE Ramos-Velasco, J Garcia-Lamont, JCR Fernandez, and MAE Rivera. Implementation of different wavelets in an auto-tuning wavenet pid controller and its application to a dc motor. In *Electronics, Robotics and Automotive Mechanics Conference (CERMA), 2011 IEEE*, pages 301–306, Nov 2011. doi: 10.1109/CERMA.2011.55.

[56] L. Jezequel and P. Argoul. New integral transform for linear systems identification. *Journal of Sound and Vibration*, 111(2):261 – 278, 1986. ISSN 0022460X.

[57] Xiaomo Jiang and Sankaran Mahadevan. Wavelet spectrum analysis approach to model validation of dynamic systems. *Mechanical Systems and Signal Processing*, 25(2):575–590, 2011.

[58] Jer-Nan Juang. *Applied system identification*. Prentice Hall, 1994.

[59] Gerald Kaiser. *A friendly guide to wavelets*. Springer, 2010.

[60] S. C. Kak. Fourier, laplace and hilbert transforms. *Electronics Letters*, 4(19):396–397, September 1968. ISSN 0013-5194. doi: 10.1049/el:19680314.

[61] Hamid Reza Karimi, Boris Lohmann, B Moshiri, and P Jabehdar Maralani. Wavelet-based identification and control design for a class of nonlinear systems. *International Journal of Wavelets, Multiresolution and Information Processing*, 4(01):213–226, 2006.

[62] T Kijewski and A Kareem. Wavelet transforms for system identification in civil engineering. *Computer-Aided Civil & Infrastructure Engineering*, 18(5):339 – 355, 2003. ISSN 10939687. URL `http://ezproxy.lib.vt.edu:8080/login?url=http:`

//search.ebscohost.com/login.aspx?direct=true&db=iih&AN=10130645&scope=site.

[63] Yoshihiro Kitada. Identification of nonlinear structural dynamic systems using wavelets. *Journal of Engineering Mechanics*, 124(10):1059–1066, 1998.

[64] Andrzej Klepka and Tadeusz Uhl. Identification of modal parameters of non-stationary systems with the use of wavelet based adaptive filtering. *Mechanical Systems and Signal Processing*, 47(12):21 – 34, 2014. ISSN 0888-3270. doi: http://dx.doi.org/10.1016/j.ymssp.2013.09.001. URL http://www.sciencedirect.com/science/article/pii/S0888327013004457. {MSSP} Special Issue on the Identification of Time Varying Structures and Systems.

[65] Ioannis A Kougioumtzoglou and Pol D Spanos. An identification approach for linear and nonlinear time-variant structural systems via harmonic wavelets. *Mechanical Systems and Signal Processing*, 37(12):338 – 352, 2013. ISSN 0888-3270. doi: http://dx.doi.org/10.1016/j.ymssp.2013.01.011. URL http://www.sciencedirect.com/science/article/pii/S0888327013000319.

[66] R. Kronland-Martinet, J. Morlet, and A. Grossman. Analysis of sound patterns through wavelet transform. *International Journal of Pattern Recognition and Artificial Intelligence*, 1(2):273–302, January 1987.

[67] A Kyprianou and WJ Staszewski. On the cross-wavelet analysis of duffing oscillator. *Journal of Sound and Vibration*, 228(1):199 – 210, 1999. ISSN 0022-460X. doi: http://dx.doi.org/10.1006/jsvi.1999.2420. URL http://www.sciencedirect.com/science/article/pii/S0022460X99924203.

[68] C-H Lamarque and J-M Malasoma. Analysis of nonlinear oscillations by wavelet transform: Lyapunov exponents. *Nonlinear Dynamics*, 9(4):333–347, 1996.

[69] C-H Lamarque, Stéphane Pernot, and A Cuer. Damping identification in multi-degree-of-freedom systems via a wavelet-logarithmic decrement part 1: theory. *Journal of Sound and Vibration*, 235(3):361–374, 2000.

[70] Joseph Lardies. Identification of a dynamical model for an acoustic enclosure using the wavelet transform. *Applied Acoustics*, 68(4):473–490, 2006.

[71] Joseph Lardies and Stephane Gouttebroze. Identification of modal parameters using the wavelet transform. *International Journal of Mechanical Sciences*, 44(11):2263–2283, 2002.

[72] Joseph Lardies and Minh-Nghi Ta. A wavelet-based approach for the identification of damping in non-linear oscillators. *International Journal of Mechanical Sciences*, 47(8):1262–1281, 2005.

[73] Thien-Phu Le and Pierre Argoul. Continuous wavelet transform for modal identification using free decay response. *Journal of Sound and Vibration*, 277(1-2):73 – 100, 2004. ISSN 0022460X. URL `http://dx.doi.org/10.1016/j.jsv.2003.08.049`.

[74] Thien-Phu Le and Pierre Argoul. Distinction between harmonic and structural components in ambient excitation tests using the time-frequency domain decomposition technique. *Mechanical Systems and Signal Processing*, 2014. ISSN 08883270. URL `http://dx.doi.org/10.1016/j.ymssp.2014.07.008`.

[75] Thien-Phu Le and Patrick Paultre. Modal identification based on the time–frequency domain decomposition of unknown-input dynamic tests. *International Journal of Mechanical Sciences*, 71:41–50, 2013.

[76] Changjiu Li, Lijun Zhao, Yingfeng Chen, and Jiefan Cui. Parameters identification of direct thrust control system using wavelet transform. In *Intelligent Control and Automation, 2008. WCICA 2008. 7th World Congress on*, pages 8842–8846. IEEE, 2008.

[77] Mu Li and Yigang He. Analog wavelet transform using multiple-loop feedback switched-current filters and simulated annealing algorithms. *AEU-International Journal of Electronics and Communications*, 68(5):388–394, 2014.

[78] Jonathan M Lilly. A data analysis package for matlab, version 1.6.2. `http://www.jmlilly.net/jmlsoft.html`, 2016.

[79] Jonathan M Lilly and Sofia C Olhede. Generalized morse wavelets as a superfamily of analytic wavelets. *IEEE Transactions on Signal Processing*, 60(11):6036–6041, 2012.

[80] Faa-Jeng Lin, Rong-Jong Wai, and Mu-Ping Chen. Wavelet neural network control for linear ultrasonic motor drive via adaptive sliding-mode technique. *Ultrasonics, Ferroelectrics, and Frequency Control, IEEE Transactions on*, 50(6):686–698, 2003.

[81] Jing Lin and Liangsheng Qu. Feature extraction based on morlet wavelet and its application for mechanical fault diagnosis. *Journal of sound and vibration*, 234(1): 135–148, 2000.

[82] Xiangqian Liu and Lin Zhang. Analysis of linear time-varying systems via Haar wavelet. *Tsinghua Science and Technology*, 4(1):1311–1313, 1999.

[83] Xiangqian Liu and Lin Zhang. Haar wavelet and its application in optimal control of linear time-invariant systems. *Tsinghua Science and Technology*, 4(1):1307–1310, March 1999.

[84] H Loussifi, K Nouri, and R Dhaouadi. Modal parameters identification of elastic drive systems using the wavelet transform. In *Power Electronics, Machines and Drives (PEMD 2010), 5th IET International Conference on*, pages 1–6, April 2010. doi: 10.1049/cp.2010.0157.

[85] RW-P Luk and Robert I Damper. Non-parametric linear time-invariant system identification by discrete wavelet transforms. *Digital Signal Processing*, 16(3):303–319, 2006.

[86] Nagabhushan Mahadevan and KA Hoo. Wavelet-based model reduction of distributed parameter systems. *Chemical Engineering Science*, 55(19):4271–4290, 2000.

[87] Stephane G Mallat. A theory for multiresolution signal decomposition: the wavelet representation. *Pattern Analysis and Machine Intelligence, IEEE Transactions on*, 11 (7):674–693, 1989.

[88] Stéphane G Mallat and Zhifeng Zhang. Matching pursuits with time-frequency dictionaries. *Signal Processing, IEEE Transactions on*, 41(12):3397–3415, 1993.

[89] Hong Mei, Om P Agrawal, and Shantaram S Pai. Wavelet-based model for stochastic analysis of beam structures. *AIAA journal*, 36(3):465–470, 1998.

[90] Leonard Meirovitch. *Principles and techniques of vibrations*, volume 1. Prentice Hall New Jersey, 1997.

[91] A P S Meliopoulos and Chien-Hsing Lee. An alternative method for transient analysis via wavelets. *Power Delivery, IEEE Transactions on*, 15(1):114–121, Jan 2000. ISSN 0885-8977. doi: 10.1109/61.847238.

[92] David Mendlovic, Zeev Zalevsky, David Mas, Javier Garc'ia, and Carlos Ferreira. Fractional wavelet transform. *Applied optics*, 36(20):4801–4806, 1997.

[93] Henrique Mohallem Paiva and Roberto Kawakami Harrop Galvão. Wavelet-packet identification of dynamic systems in frequency subbands. *Signal processing*, 86(8): 2001–2008, 2006.

[94] J Morlet, G Arens, E Fourgeau, and D Giard. Wave propagation and sampling theory-part II: Sampling theory and complex waves. *Journal of Geophysics*, 47(2):222–236, February 1982.

[95] Arch W Naylor and George R Sell. *Linear operator theory in engineering and science*. Springer Science & Business Media, New York, 2000.

[96] SA Neild, PD McFadden, and MS Williams. A review of time-frequency methods for structural vibration analysis. *Engineering Structures*, 25(6):713 – 728, 2003. ISSN 0141-0296. doi: http://dx.doi.org/10.1016/S0141-0296(02)00194-3. URL `http://www.sciencedirect.com/science/article/pii/S0141029602001943`.

[97] D E Newland. Wavelet analysis of vibration, part I: Theory. *Journal of Vibration and Acoustics*, 1994.

[98] D E Newland. Wavelet analysis of vibration, part II: Wavelet maps. *Journal of Vibration and Acoustics*, 1994.

[99] D E Newland. Ridge and phase identification in the frequency analysis of transient signals by harmonic wavelets. *Journal of Vibration and Acoustics*, 121(2):149–155, April 1999. ISSN 0739-3717. doi: 10.1115/1.2893957. URL `http://dx.doi.org/10.1115/1.2893957`.

[100] David E Newland. Harmonic wavelet analysis. *Proceedings of the Royal Society of London. Series A: Mathematical and Physical Sciences*, 443(1917):203–225, 1993. doi: 10.1098/rspa.1993.0140. URL `http://rspa.royalsocietypublishing.org/content/443/1917/203.abstract`.

[101] Ricardo P Pacheco and Valder Steffen Jr. On the identification of non-linear mechanical systems using orthogonal functions. *International Journal of Non-Linear Mechanics*, 39(7):1147–1159, 2004.

[102] S Parvez and Zhiqiang Gao. A wavelet-based multiresolution PID controller. *Industry Applications, IEEE Transactions on*, 41(2):537–543, March 2005. ISSN 0093-9994. doi: 10.1109/TIA.2005.844378.

[103] Shahid Parvez and Zhiqiang Gao. A novel controller based on multi-resolution decomposition using wavelet transforms. *TECHNICAL PAPERS-ISA*, 422:407–416, 2002.

[104] AE Pearson and FC Lee. On the identification of polynomial input-output differential systems. *Automatic Control, IEEE Transactions on*, 30(8):778–782, 1985.

[105] VL Pham and KP Wong. Wavelet-transform-based algorithm for harmonic analysis of power system waveforms. *Generation, Transmission and Distribution, IEE Proceedings-*, 146(3):249–254, May 1999. ISSN 1350-2360. doi: 10.1049/ip-gtd:19990316.

[106] VF Poterasu. Wavelets transform for nonlinear control of multibody systems. *Journal of the Franklin Institute*, 338(2):321–334, 2001.

[107] Akhilesh Prasad and Ashutosh Mahato. The fractional wavelet transform on spaces of type s. *Integral Transforms and Special Functions*, 23(4):237–249, 2012.

[108] S Qian and Dapang Chen. Joint time-frequency analysis. *Signal Processing Magazine, IEEE*, 16(2):52–67, Mar 1999. ISSN 1053-5888. doi: 10.1109/79.752051.

[109] A N Robertson, KC Park, and K F Alvin. Extraction of impluse response data via wavelet transform for structural system identification. *Journal of Vibration and Acoustics*, 1998.

[110] Enders A Robinson. *Random wavelets and cybernetic systems*, volume 9. Hafner Publishing Company, 1962.

[111] C Rouby, D Remond, and P Argoul. Orthogonal polynomials or wavelet analysis for mechanical system direct identification. *Annals of Solid and Structural Mechanics*, 1(1):41 – 58, 2010. ISSN 18676936. URL http://dx.doi.org/10.1007/s12356-009-0005-1.

[112] M Ruzzene, A Fasana, L Garibaldi, and B Piombo. Natural frequencies and dampings identification using wavelet transform: Application to real data. *Mechanical Systems and Signal Processing*, 11(2):207 – 218, 1997. ISSN 0888-3270. doi: http://dx.doi.org/10.1006/mssp.1996.0078. URL http://www.sciencedirect.com/science/article/pii/S0888327096900783.

[113] DA Schoenwald. System identification using a wavelet-based approach. In *Decision and Control, 1993., Proceedings of the 32nd IEEE Conference on*, pages 3064–3065 vol.4, Dec 1993. doi: 10.1109/CDC.1993.325767.

[114] Ervin Sejdić, Igor Djurović, and LJubiša Stanković. Fractional fourier transform as a signal processing tool: An overview of recent developments. *Signal Processing*, 91(6): 1351–1369, 2011.

[115] Yuh-Tay Sheen and Chun-Kai Hung. Constructing a wavelet-based envelope function for vibration signal analysis. *Mechanical Systems and Signal Processing*, 18(1):119 – 126, 2004. ISSN 0888-3270. doi: http://dx.doi.org/10.1016/S0888-3270(03)00046-3. URL http://www.sciencedirect.com/science/article/pii/S0888327003000463.

[116] Jun Shi, NaiTong Zhang, and XiaoPing Liu. A novel fractional wavelet transform and its applications. *Science China Information Sciences*, 55(6):1270–1279, 2012.

[117] T Shojaeizadeh and E Babolian. A computational method for solving optimal control problem of time-varying singular systems using the Haar wavelets. *International Journal of Industrial Mathematics*, 4(1):1–9, 2012.

[118] J Slavic, I Simonovski, and M Boltezar. Damping identication using a continuous wavelet transform: application to real data. *Journal of Sound and Vibration*, 2003.

[119] Akira Sone, Hiroaki Hata, and Arata Masuda. Identification of structural parameters using the wavelet transform of acceleration measurements. *Journal of pressure vessel technology*, 126(1):128–133, 2004.

[120] Wieslaw J Staszewski and D Mark Wallace. Wavelet-based frequency response function for time-variant systems an exploratory study. *Mechanical Systems and Signal Processing*, 47(1):35–49, 2013.

[121] WJ Staszewski. Identification of damping in MDOF systems using time-scale decomposition. *Journal of Sound and Vibration*, 203(2):283 – 305, 1997. ISSN 0022-460X. doi: http://dx.doi.org/10.1006/jsvi.1996.0864. URL http://www.sciencedirect.com/science/article/pii/S0022460X96908640.

[122] WJ Staszewski. Identification of non-linear systems using multi-scale ridges and skeletons of the wavelet transform. *Journal of Sound and Vibration*, 214(4):639 – 658, 1998. ISSN 0022-460X. doi: http://dx.doi.org/10.1006/jsvi.1998.1616. URL http://www.sciencedirect.com/science/article/pii/S0022460X98916169.

[123] WJ Staszewski and JE Cooper. Flutter data analysis using the wavelet transform. In *New Advances in Modal Synthesis of Large Structures: Non-linear Damped and Non-deterministic Cases: Proceedings of the international conference MV2, Lyon, France, 5-6 October 1995*, page 203. CRC Press, 1997.

[124] W.J. Staszewski and J. Giacomin. Application of the wavelet based frfs to the analysis of nonstationary vehicle data. In *Proceedings of 15th International Modal Analysis Conference*, volume 1(4), pages 425–431, 1997.

[125] WJ Staszewski and GR Tomlinson. Application of the wavelet transform to fault detection in a spur gear. *Mechanical Systems and Signal Processing*, 8(3):289 – 307, 1994. ISSN 0888-3270. doi: http://dx.doi.org/10.1006/mssp.1994.1022. URL http://www.sciencedirect.com/science/article/pii/S0888327084710223.

[126] WC Su, CY Liu, and CS Huang. Identification of instantaneous modal parameter of time-varying systems via a wavelet-based approach and its application. *Computer-Aided Civil and Infrastructure Engineering*, 29(4):279–298, 2014.

[127] Arun K Tangirala, Siddhartha Mukhopadhyay, and Akhilanand P Tiwari. Wavelets applications in modeling and control. *Control and Optimisation of Process Systems*, 43:107, 2013.

[128] Ph Tchamitchan and B Torresani. *Wavelets and Their Applications*, chapter Ridge and Skeleton Extraction from The Wavelet Transform, pages 123–153. Jones and Bartlett Publishers, 1992.

[129] Jale Tezcan. *Non-Linear System Response to Non-Stationary Input Processes Using Harmonic Wavelets*. PhD thesis, Rice University, Houston, Texas, 2005.

[130] P Tratskas and PD Spanos. Linear multi-degree-of-freedom system stochastic response by using the harmonic wavelet transform. *Journal of applied mechanics*, 70(5):724–731, 2003.

[131] MK Tsatsanis and GB Giannakis. Time-varying system identification using wavelets. In *Signals, Systems and Computers, 1992. 1992 Conference Record of The Twenty-Sixth Asilomar Conference on*, pages 125–129 vol.1, Oct 1992. doi: 10.1109/ACSSC.1992.269245.

[132] Zdeněk Váňa and Heinz A Preisig. System identification in frequency domain using wavelets: Conceptual remarks. *Systems & Control Letters*, 61(10):1041–1051, 2012.

[133] M. Vetterli and C. Herley. Wavelets and filter banks: theory and design. *Signal Processing, IEEE Transactions on*, 40(9):2207–2232, Sep 1992. ISSN 1053-587X. doi: 10.1109/78.157221.

[134] M. Vetterli and J. Kovacevic. *Wavelets and Subband Codding*. Prentice Hall Signal Processing series. Prentice Hall PTR, Englewood Cliffs, New Jersey, 1995.

[135] Stacy S Wilson. Using a pseudo-random binary sequence as a mother wavelet in the wavelet-correlation system identification method. In *SoutheastCon, 2002. Proceedings IEEE*, pages 58–61. IEEE, 2002.

[136] Stacy S Wilson. Optimizing the performance of the wavelet-correlation system identification method. In *SoutheastCon, 2012 Proceedings of IEEE*, pages 1–5. IEEE, 2012.

[137] Xiru Wu, Yaonan Wang, and Xuanju Dang. Robust adaptive sliding-mode control of condenser-cleaning mobile manipulator using fuzzy wavelet neural network. *Fuzzy Sets and Systems*, 235:62–82, 2014.

[138] Jin-Chao Xu and Wei-Chang Shann. Galerkin-wavelet methods for two-point boundary value problems. *Numerische Mathematik*, 63(1):123–144, 1992.

[139] X Xu, ZY Shi, and SL Long. Time-varying systems identification using continuous wavelet analysis of free decay response signals. *Journal of Vibroengineering*, 14(1):225 – 235, 2012. ISSN 13928716. URL `http://ezproxy.lib.vt.edu:8080/login?url=http://search.ebscohost.com/login.aspx?direct=true&db=iih&AN=74028552&scope=site`.

[140] X Xu, ZY Shi, and Q You. Identification of linear time-varying systems using a wavelet-based state-space method. *Mechanical Systems and Signal Processing*, 26(0): 91 – 103, 2012. ISSN 0888-3270. doi: http://dx.doi.org/10.1016/j.ymssp.2011.07.005. URL `http://www.sciencedirect.com/science/article/pii/S0888327011002937`.

[141] Banfu Yan and Ayaho Miyamoto. A comparative study of modal parameter identification based on wavelet and Hilbert-Huang transforms. *Computer-Aided Civil and Infrastructure Engineering*, 21(1):9 – 23, 2006. ISSN 10939687. URL `http://dx.doi.org/10.1111/j.1467-8667.2005.00413.x`.

[142] BF Yan, Ayaho Miyamoto, and Eugen Brühwiler. Wavelet transform-based modal parameter identification considering uncertainty. *Journal of Sound and Vibration*, 291 (1):285–301, 2006.

[143] HP Yin, D Duhamel, and P Argoul. Natural frequencies and damping estimation using wavelet transform of a frequency response function. *Journal of Sound and Vibration*, 271(3-5):999 – 1014, 2004. ISSN 0022460X. URL `http://dx.doi.org/10.1016/j.jsv.2003.03.002`.

[144] Ksaku Yoshida. *Functional Analysis*, volume 123. Springer-Verlag, Berlin Heidelberg, Germany, 1st edition, 1965. doi: 10.1007/978-3-662-25762-3.

[145] Zhou Youhe, Wang Jizeng, and Zheng Xiaojing. Applications of wavelet Galerkin FEM to bending of beam and plate structures. *Applied Mathematics and Mechanics*, 19(8): 745–755, 1998. ISSN 0253-4827. doi: 10.1007/BF02457749. URL `http://dx.doi.org/10.1007/BF02457749`.

[146] Maryam Zekri, Saeed Sadri, and Farid Sheikholeslam. Adaptive fuzzy wavelet network control design for nonlinear systems. *Fuzzy Sets and Systems*, 159(20):2668–2695, 2008.

[147] Qinghua Zhang and Albert Benveniste. Wavelet networks. *Neural Networks, IEEE Transactions on*, 3(6):889–898, 1992.

[148] Yanyang Zi, Xue Feng Chen, Zheng Jia He, and Peng Chen. Vibration based modal parameters identification and wear fault diagnosis using Laplace wavelet. *Key Engineering Materials*, 293:183–192, 2005.